# REGIONAL MAPPING OF CROPS UNDER AGRICULTURAL NETS USING SENTINEL-2

By Rozanne Mouton

*Thesis presented in partial fulfilment of the requirements for the degree of Master of Science in the Faculty of Science at Stellenbosch University.*




Supervisor: Prof. A van Niekerk

September 2022

# DECLARATION

By submitting this report electronically, I declare that the entirety of the work contained therein is my own, original work, that I am the sole author thereof (save to the extent explicitly otherwise stated), that reproduction and publication thereof by Stellenbosch University will not infringe any third party rights and that I have not previously in its entirety or in part submitted it for obtaining any qualification.

Date: December 2022

# SUMMARY

The use of agricultural nets is rapidly expanding worldwide as farmers are forced to adapt to the adverse effects of climate change on crops. These nets have diverse spectral properties due to their differing colours, thicknesses, porosities and the large variety of plastic compounds used to make the nets. As such, nets are difficult to map using existing remote sensing techniques. To address this problem, this study aimed to fill several research gaps pertaining to mapping agricultural nets, with a specific focus on the use of Sentinel-2 imagery. Sentinel-2 imagery is freely available and has a short (5-day) revisit time, making it a viable data source for monitoring large areas. However, there are limited research findings about whether Sentinel-2 imagery has the necessary spatial and spectral resolutions to effectively capture nets. This question was addressed through two experiments conducted in the Western Cape, South Africa.

The first experiment aimed to record and interpret the spectral signatures of the most common types of nets used in the Western Cape and to investigate how these signatures are affected by the seasonal changes of their underlying crops. Spectral signatures of nets covering vineyards, citrus, and berry crops were collected for an entire growing season. The Jeffries-Matusita distance was used to quantify the spectral separability among the net classes and their surrounding land cover and how the signatures changed over time. The results showed that the spectral resolution of the Sentinel-2 imagery was adequate to identify distinguishable net signatures. Furthermore, it was found that the signatures of the underlying crops could also be identified. The net types were most separable during the summer months.

The second experiment aimed to investigate whether Sentinel-2 imagery has the necessary spatial and spectral resolutions required to map nets. The experiment also tested different machine learning classifiers and classification features to determine which method and features were best suited for mapping nets. The classifications achieved high accuracies which were comparable to the accuracies achieved by studies that used very-high-resolution imagery (like WorldView-3 and QuickBird) for mapping agricultural nets. The accuracies achieved in the second experiment were higher than those found in studies using lower resolution Landsat imagery. The results showed that the unaltered Sentinel-2 bands contained the most important features for classification and that both the random forest and the neural network algorithms achieved high accuracies for mapping nets.

Both experiments confirmed that Sentinel-2 imagery has the necessary spatial and spectral resolutions to effectively capture and map nets. This insight makes Sentinel-2 a practical and viable option for mapping strategies in agriculture. Furthermore, this study provided valuable information

about the spectral characteristics of agricultural nets, and effective techniques for mapping the distribution of agricultural nets.

**KEY WORDS**

agricultural nets, Jeffries-Matusita, machine learning, neural network, plasticulture, random forest, Sentinel-2, supervised classification, support vector machine

# OPSOMMING

Die gebruik van nette vir landbou neem wêreldwyd toe, hoofsaaklik omdat hierdie nette die oeste teen die negatiewe gevolge van klimaatsverandering beskerm. Landbounette word van verskillende tipes plastiek gemaak en kan in vele kleure en digthede voorkom. Daarom het hierdie nette uiteenlopende spektrale eienskappe en word nette moeilik met die gebruik van satellietbeelde gekarteer. Om hierdie probleem op te los, ondersoek hierdie studie die gebruik van Sentinel-2 satellietbeelde om landbounette te klassifiseer. Sentinel-2 satellietbeelde is vrylik beskikbaar en word elke vyf dae herhaal. Hierdie twee eienskappe maak Sentinel-2 beelde geskik om groot landbougebiede met landbounette te karteer, maar ongelukkig was daar nog geen navorsing gedoen om Sentinel-2 beelde hiervoor te toets nie. Hierdie studie is gevolglik gerig om dié navorsingsvraag te beantwoord. Om te bepaal of Sentinel-2 beelde vir die klassifikasie van landbounette gebruik kan word, het die huidige studie twee eksperimente uitgevoer.

Die eerste eksperiment het die spektrale eienskappe van die landbounette ondersoek om te bepaal hoe hierdie nette in die Sentinel-2 beelde vertoon en om vas te stel of die spektrale eienskappe as gevolg van die plante onder die net oor tyd verander. ‘n Spektrale grafiek is vir drie tipes nette geskep, naamlik vir  nette wat oor druiwe, sitrus en bessie gewasse gespan was. Die Jeffries-Matusita metode is gebruik om te bepaal of die unieke spektrale eienskappe van landbounette akkuraat genoeg in Sentinel-2 beelde uitgebeeld kan word sodat uitgekenning uitgevoer kan word. Daarna was die grafieke gebruik om vas te stel hoe die spektrale eienskappe van die landbounette verander soos wat die gewasse onder die nette gedurend die groeiseisoen verander. Die resultate toon dat die resolusie van die Sentinel-2 beelde goed genoeg is om die unieke spektrale eienskappe van die landbounette en die gewasse onder die nette vas te stel. Die resultate toon ook dat die landbounette die maklikste tydens somer geklassifiseer kan word.

Die doel van die tweede eksperiment was om te sien of Sentinel-2 beelde vir die kartering van landbounette geskik is. Die eksperiment het ook ondersoek ingestel oor watter masjienleer metodes en veranderlikes die beste vir klassifikasie werk. Die neurale netwerk en ewekansige woud metodes het die beste resultate gelewer. Die akkuraatheid van dié klassifikasies was hoër as kaarte wat deur ander navorsers met Landsat beelde gemaak is en net so hoog soos kaarte wat met baie hoë resolusie beelde (soos Wordview-3 en QuickBird) gemaak is.

Die studie het bewys dat Sentinel-2 satellietbeelde gebruik kan word om landbounette te klassifiseer en om akkurate landboukaarte te maak. Verder voorsien die resultate unieke insig oor die spektrale eienskappe van landbounette, en watter masjienleer metodes en veranderlikes nuttig is om landbounette te klassifiseer.

**TREFWOORDE**

Beeldklassifikasie, landbounette, masjienleer, Sentinel-2

# ACKNOWLEDGEMENTS

I sincerely thank:

- My supervisor, Professor Adriaan Van Niekerk, for his patience and guidance throughout my research.
- My family and friends for their support and belief in my abilities.
- The Water Research Commission for funding this study, which formed part of a larger project titled *WATER FOOTPRINT AS A SUSTAINABILITY INDICATOR FOR TABLE AND WINE GRAPE PRODUCTION*. More information about this project is available in the WRC Report No. 2710/1/20 (ISBN 978-0-6392-0151-1) available at www.wrc.org.za.

# CONTENTS

# TABLES

# FIGURES

# APPENDICES

# ACRONYMS AND ABBREVIATIONS

| | |
|---|---|
| ABA | Average balanced accuracy |
| AKS | Average kappa statistic |
| AOA | Average overall accuracy |
| ARVI | Atmospheric resistant vegetation index |
| ASM | Angular second moment |
| BA | Balanced accuracy |
| BioPar | Biophysical Parameter Service |
| BOA | Bottom of atmosphere |
| DT | Decision tree |
| ED2 | Euclidean distance 2 |
| EMR | Electromagnetic radiation |
| EMS | Electromagnetic spectrum |
| ESA | European Space Agency |
| ESP | Estimation of scale parameter |
| EUROLAND | European Land Monitoring Service |
| EVI | Enhanced vegetation index |
| FSO | Feature space optimization |
| GCP | Ground control point |
| GDP | Gross domestic product |
| GEE | Google Earth Engine |
| GLCM | Grey-level co-occurrence matrix |
| GLDV | Grey-level difference vector |
| IFOV | Instantaneous field of view |
| JM | Jeffries-Matusita |
| KNN | K-nearest neighbour |
| KS | Kappa statistic |
| ML | Machine learning |
| MRS | Multiresolution segmentation |
| MSI | Multispectral instrument |
| NDSI | Normalized difference sandy index |
| NDVI | Normalized difference vegetation index |
| NIR | Near-infrared |
| NN | Neural networks |
| OA | Overall accuracy |

| | |
|---|---|
| OBIA | Object-based image analysis |
| OSAVI | Optimized soil-adjusted vegetation index |
| PBIA | Per-pixel image analysis |
| PE | Polyethene |
| PGI | Plastic greenhouse index |
| PML | Plastic-mulched land cover |
| PMLI | Plastic-mulched land cover index |
| PP | Polypropylene |
| PSI | Plastic surface index |
| RBF | Radial basis function |
| RBT | Rescaled brightness temperature |
| RE | Red edge |
| RF | Random forest |
| RF-RFE | Random forest recursive feature elimination |
| RGB | Red, green and blue |
| ROI | Regions of interest |
| SAR | Synthetic aperture radar |
| SATChMo | Seasonal and Annual Change Monitoring Service |
| SAVI | Soil-adjusted vegetation index |
| SVM | Support vector machines |
| SWIR | Short-wave infrared |
| TD | Transformed divergence |
| TOA | Top of atmosphere |
| VARI | Visible atmospherically resistant index |

# CHAPTER 1: INTRODUCTION

Climate is the primary constituent influencing agricultural productivity (Adams et al. 1998). Given the crucial role that agriculture plays in food security, there are growing concerns about the effects of climate change on crop production (Matsei 2016). Climate change is primarily characterised by increased weather variability, which includes unreliable rainfall, increased temperatures and the increased frequency of extreme weather conditions (Jones, Singels & Ruane 2015). Farmers have had to adapt to these changes to maintain yields (Bryan et al. 2009). A variety of adaptation methods are employed by farmers, including the use of agricultural nets (Howden et al. 2007). These nets are used to protect crops from sunburn, wind, intense rainfall, hail and pests, which all contribute to losses in crop yield and quality (Briassoulis, Mistriotis & Eleftherakis 2007).

Remote sensing can provide timely and accurate images of large areas, thus making it an indispensable tool for mapping, monitoring and managing agricultural activities (Atzberger 2013). Some of the applications of remote sensing in agriculture are the estimation of water stress in plants, the assessment of plant health and the determination of crop yield which all provide essential information to maintain a successful agricultural sector (Mulla 2013). However, the introduction of agricultural nets has limited the capabilities of remote sensing in the agricultural sector. For instance, Van Niekerk et al. (2018) used remote sensing to quantify water use of irrigated crops, but they had to exclude crops grown under agricultural nets due to the nets' effect on spectral reflection and the uncertainties they cause in estimating evapotranspiration.

Agricultural nets are made from plastic thread woven or knitted to form a regular porous geometric structure which allows the free movement of fluids (Castellano et al. 2008). Given this broad definition, the diverse nature of agricultural practices and the variety of applications that agricultural nets are used for, the physical properties of these nets vary greatly (Briassoulis, Mistriotis & Eleftherakis 2007). Consequently, agricultural nets are difficult to identify, classify and map using remote sensing, and no robust methodology for mapping agricultural nets exists as yet. Accurate maps of agricultural areas, crops and activities, including the use of agricultural nets, will aid the effective management of natural and agricultural resources, ultimately contributing to food security and economic growth.

## 1.1 AGRICULTURAL NETS

Protected agriculture involves the modification of the natural environment to optimize conditions for plant growth. These modifications have undergone a rapid spatial expansion in recent years to cover more than 500 000 hectares worldwide (Agüera, Aguilar & Aguilar 2008). The modifications can be divided into three main categories, namely greenhouses, plastic tunnels and

agricultural nets (Jensen & Malter 1995). Traditionally, glass-covered greenhouses were the most popular modification used in agriculture. However, the advancement of plastic technologies has led to the rapid adoption of plasticulture, a term used to describe the practice of plastic-covered agriculture (Levin et al. 2010).

Agricultural nets constitute a large part of plasticulture and they have gained popularity as a less expensive alternative to greenhouses and tunnels, covering some 61 800 hectares of crops in Europe (Scarascia-Mugnozzo, Sica & Russo 2011). These nets have a variety of uses and are therefore characterised by various threading patterns, plastic materials, weights, colours, shading factors, durabilities, porosities, air permeabilities and breaking strengths (Castellano, Candura & Scarascia Mugnozza 2008). Consequently, the nets interact with electromagnetic radiation (EMR) in slightly differing ways that have implications for the development and mapping of crops (Levin et al. 2010). Previous research has mainly investigated the reflective and transmissive properties of nets as these are most relevant for agricultural and remote sensing applications. Agricultural nets interact with both diffuse and direct radiation (Al-Helal & Abdel-Ghany 2011). Diffuse radiation is electromagnetic energy that has been scattered by the atmosphere and therefore results from the atmosphere's inherent illumination, whereas direct radiation is electromagnetic energy that is directly produced by an active sensor or the sun (Liu & Jordan 1960).

Scarascia-Mugnozzo, Sica & Russo (2011) investigated the different types of plastic material that are used to make agricultural nets in Europe and they found that polyethene (PE) and polypropylene (PP) were the most popular groups of material used. They determined that the unique properties of each plastic group significantly affected the transmissive and reflective properties of the agricultural nets, resulting in distinct spectral responses in different regions of the electromagnetic spectrum. They also noted that newer technologies were applying the unique properties of certain plastic materials to create nets with specific photoselective and photoluminescent properties. Hemming et al. (2008) found that the spectral characteristics of agricultural nets were significantly affected by the porosity of the nets and the angle of incident radiation. They observed that the spectral responses of agricultural nets change depending on the season and time of day, as well as the shape and thickness of the netted structure.

Al-Helal & Abdel-Ghany (2011) examined the effect of incidence angle and time of day on the spectral characteristics of agricultural nets. They concluded that the colour of the nets and the angle of illumination affected the transmission and reflection of the radiation more than the porosity, with brighter colours and a higher incident angle producing higher reflectance. Shahak et al. (2004) studied the effect of net colour on the transmissive and reflective properties of the nets. The coloured (red, blue or yellow) nets showed varied responses in the visible portion of the spectrum,

while the spectral responses of neutral-coloured (black, white or grey) nets were more homogenous. However, both the coloured and neutral nets showed similar reflective responses in the near-infrared (NIR) portion of the electromagnetic spectrum. The transmittance of all the nets were wavelength-dependent and increased as the wavelength increased. Similar findings were reported by Castellano, Russo & Mugnozza (2006) and Espí et al. (2006). A limitation of these studies was that wavelengths beyond 850 nm (NIR) were not considered. Sica & Picuno (2008) extended the range to 2500 nm and found an additional absorption feature around 1800 nm which could be utilized by remote sensors to identify agricultural nets. Understanding the spectral properties of plastic-covered agriculture, allow these properties to be exploited to map plasticulture using remote sensing. The following section gives a brief introduction to optical remote sensing and examines how optical sensors have been used to map plasticulture.

## 1.2 OPTICAL REMOTE SENSING FOR MAPPING PLASTICULTURE

Remote sensing applications use different types of sensors, of which optical and synthetic aperture radar (SAR) sensors are common. The optical type include air- or space-borne sensors that rely on the visible to short-wave infrared (SWIR) portion of the electromagnetic spectrum to capture information about the earth's surface (Campbell & Wynne 2011). These optical sensors have become indispensable for mapping and monitoring land cover (Lautenbacher 2006) but the standard techniques used for land cover mapping are often less effective for mapping agricultural nets (Agüera, Aguilar & Aguilar 2008). Optical sensors can have a small number of discrete bands (multispectral) or a large number of contiguous bands (hyperspectral) (Campbell & Wynne 2011).

Multispectral Landsat imagery has been widely used for mapping plasticulture (Lanorte et al. 2017; Levin et al. 2010; Novelli et al. 2016; Novelli & Tarantino 2015). This high-resolution imagery is freely available, it has global coverage and it is useful for mapping land cover (Gibson & Power 2000). Lanorte et al. (2017) mapped plastic films and nets using Landsat-8 imagery. The classification achieved a user's accuracy of 87% and a producer's accuracy of 97% for the nets class. However, their study was limited by the small size and homogeneity of the study area. Novelli & Tarantino (2015) had earlier used Landsat-8 imagery to map agricultural nets involving four spectral indices, namely the normalized difference vegetation index (NDVI), the rescaled brightness temperature (RBT) index, the plastic surface index (PSI) and the normalized difference sandy index (NDSI). All the test sites achieved overall accuracies above 82%, with NDVI and PSI making significant contributions to these accuracies. Levin et al. (2010) compared the use of AISA-ES hyperspectral imagery and Landsat-7 ETM+ imagery for mapping agricultural nets. The hyperspectral imagery was able to use absorption features at 1218 nm, 1732 nm and 2313 nm in combination with NDVI to achieve a classification accuracy of 90%. The lower spectral and spatial

resolutions (30 m) of the Landsat-7 imagery led to a classification accuracy that was significantly lower than that of the hyperspectral imagery. Novelli et al. (2016) compared the use of Landsat-8 imagery and Sentinel-2 imagery for mapping plastic greenhouses. They followed an object-based approach with several spectral indices, including NDVI and the plastic-mulched land cover index (PMLI). Sentinel-2 significantly outperformed Landsat-8, owing the former's higher spatial resolution. Based on this outcome, Novelli et al. (2016) speculated that Sentinel-2 imagery could be used to map other types of plasticulture. Considering that Sentinel-2 imagery has not been used to map agricultural nets, the following section will discuss the properties of Sentinel-2 imagery that present this sensor as a viable source of imagery for this application.

## 1.3 SENTINEL-2 IMAGERY FOR LAND COVER CLASSIFICATION

Sentinel-2 is a high-resolution, space-borne sensor that captures multispectral imagery in the visible to SWIR portion of the electromagnetic spectrum. The onboard multispectral instrument (MSI) of Sentinel-2 acquires 13 spectral bands of which four have a spatial resolution of 10 m, six have a spatial resolution of 20 m and each of the remaining three has a spatial resolution of 60 m (Wang et al. 2016). The constellation of two satellites provides freely available data every five days with global coverage (Drusch et al. 2012).

The mapping of agricultural nets requires that the nets' signatures be separated from the surrounding agricultural and other land covers (Novelli & Tarantino 2015) because the spectral signatures of agricultural nets consist of the combined signatures of the underlying crops and the plastic net. Similarly, urban mapping requires the detection of objects that represent a spectral mixture of artificial material and vegetation (Levin et al. 2010). Consequently, the extant studies combined the methods used to map land cover in agricultural and in urban areas to classify agricultural nets (Levin et al. 2010).

The Sentinel-2 sensor has three bands in the red edge (RE) region, namely bands five to seven which are useful for vegetation mapping (Clevers & Gitelson 2012). The RE refers to the region of extreme change in the reflection of healthy vegetation measured between the red and NIR portions of the electromagnetic spectrum (Horler, Dockray & Barber 1983). Immitzer et al. (2016) explored the suitability of Sentinel-2 imagery for the classification of land cover in agricultural and forested areas. They specifically aimed to determine the importance of each Sentinel-2 band for this application. They found that band 5, the first RE band, was the most important feature for detecting agricultural land cover and the third most important for detecting forested land cover. The SWIR bands (bands 11 and 12) ranked among the top five most important bands for both agriculture and forest classifications. They determined that Sentinel-2 imagery was highly effective for large-scale land cover classification. Belgiu & Csillik (2018) later used multitemporal

NDVI imagery, derived from Sentinel-2 imagery, to classify agricultural land and achieved accuracies exceeding 85% for two of their three study sites. However, they recommended that NDVI should be used in addition to the spectral bands and not as the only classification feature. Maponya, Van Niekerk & Mashimbye (2020) used multitemporal Sentinel-2 imagery for the mapping of crop types. They found that the multitemporal imagery produced higher accuracies than single-date imagery. Other studies that have demonstrated the suitability of Sentinel-2 imagery for land cover classification are those by Varga et al. (2018) and Prins & Niekerk (2020).

Lefebvre et al. (2016) proposed the use of Sentinel-2 imagery to update an existing urban data set, which had originally been created using Landsat-8 imagery. The results showed that both the spectral and the spatial characteristics of the Sentinel-2 imagery were effective for mapping urban land cover. They also found that the Sentinel-2 imagery improved the geometric accuracy of the existing Landsat-8 classification. Pesaresi et al. (2016) compared the use of Sentinel-2 and Landsat-8 imagery for mapping urban land cover to detect built-up areas in Italy. Sentinel-2 was shown to outperform Landsat-8 and it was concluded that Sentinel-2 imagery was highly effective for mapping highly heterogenous landscapes due to the sensor's high spatial and spectral resolutions. The aptitude of Sentinel-2 imagery for mapping plastic greenhouses, agriculture and complex urban landscapes allude to viability of Sentinel-2 imagery for mapping agricultural nets. South Africa has a prominent need for accurate maps of agricultural areas that include agricultural nets. The following section expands on the role of agricultural nets within the agricultural sector of South Africa.

## 1.4 AGRICULTURAL NETS IN SOUTH AFRICAN

Agriculture is a prominent sector in the South African economy that contributed more than R80 billion to the country's gross domestic product (GDP) in 2017 (Matsei 2016). With the country's population projected to grow by two percent per year (SSA 2017) and the adverse effects of climate change threatening our agricultural productivity (SANBI 2013), South Africa's food security is under threat (Matsei 2016). Agricultural nets are considered to play a major role in the adaptive strategies needed to ensure food security and economic development in the country (Pienaar 2018). However, where other countries such as Spain (Aguilar et al. 2016), Italy (Blanco et al. 2018) and Israel (Levin et al. 2010) have proactively implemented programmes to map and analyse the efficacy of agricultural nets, South Africa is yet to investigate this. Consequently, only limited information is available about the current extent, the location and the effect on crop yield of agricultural nets within South Africa. Figure 1.1 shows what agricultural shade nets used in South Africa typically look like.

Adapted from Knitex (2020)

Figure 1.1 Agricultural shade nets covering crops in the Western Cape province, South Arica

## 1.5 PROBLEM FORMULATION

Accurate and complete maps of agricultural activities are needed for effective management and policy implementation in the agricultural sector. Remote sensing is a proven method for accurately mapping large agricultural areas. However, the diverse spectral properties of agricultural nets make them difficult to map using remote sensing. To successfully map these nets it is important to understand their spectral dynamics and to experiment with a range of classification strategies. Several authors have studied the spectral properties of agricultural nets (Agüera, Aguilar & Aguilar 2008; Hemming et al. 2008; Levin et al. 2010). They have published that three important factors affect their spectral properties, namely the types and seasonal variations of the crops under the nets, the physical characteristics of the nets, and the angle of illumination (Levin et al. 2010). The accurate mapping of nets therefore requires an understanding of the spectral dynamics of agricultural nets and the ways how the spectral signatures of nets are affected by underlying crops.

Several classification approaches have been followed to map plasticulture (Aguilar et al. 2016; Carvajal et al. 2006; Hörig et al. 2001). Generally, the use of imagery with high spatial resolutions lead to the most accurate classification results. Very-high-resolution imagery acquired with WorldView-3 and QuickBird is particularly effective, but this imagery is expensive so limiting its viability for mapping large areas (Carleer, Debeir & Wolff 2005). High-resolution imagery from Landsat-8 and Sentinel-2 have been accessed for mapping plasticulture (Levin et al. 2010; Novelli et al. 2016). The spatial resolution of Landsat-8 imagery proved to be inadequate, although ancillary classification features, such as NDVI, were found to improve accuracy (Levin et al. 2010). Sentinel-2 imagery yielded higher accuracies than those of Landsat-8 imagery (Novelli et al. 2016). Sentinel-2 imagery has been proven useful in diverse land cover mapping applications, including the mapping of plastic greenhouses (Novelli et al. 2016), but has not yet been evaluated for mapping agricultural nets. Hence a clear need exists to access the efficacy of spectral indices,

texture features and different classification algorithms for mapping agricultural nets using Sentinel-2 imagery. Little is also known about the spectral signatures of nets used in South Africa and how these signatures change with the seasonal variations of underlying crops. Such information is essential to developing a strategy for mapping nets in South Africa. This research therefore intends to answer the following research questions:

1. What are the spectral properties of agricultural nets as captured by the Sentinel-2 MSI?
2. How do the underlying crops affect the spectral signatures of agricultural nets?
3. Which spectral indices, texture features and classification algorithms are the most effective for mapping agricultural nets using Sentinel-2 imagery?
4. To what extent can Sentinel-2 be used to cost-effectively map specific crops grown under nets at regional (provincial) scale?

The information gained by answering these questions will add to the body of knowledge required to develop a robust methodology for mapping the distribution of agricultural nets across South Africa. The following section will outline the aims and objectives through which the research questions will be addressed.

## 1.6 RESEARCH AIMS AND OBJECTIVES

The primary aim of this study is to develop a spectral profile of agricultural nets using Sentinel-2 imagery and the secondary aim is to demonstrate how the spectral profile can be used to map agricultural nets and the specific crops grown under the nets. To achieve these aims, six objectives are pursued:

1. review the relevant literature on the properties of agricultural nets, multispectral classification techniques and the approaches to accuracy assessment;
2. acquire appropriate remotely sensed data and collect suitable reference data for spectral analysis, classifier training and accuracy assessment;
3. compile a spectral profile for agricultural nets in the Western Cape using Sentinel-2 imagery;
4. determine the influence underlying crops have on the spectral signatures of agricultural nets;
5. develop and demonstrate a method for differentiating agricultural nets in the Western Cape from other land covers using Sentinel-2 imagery;

6. interpret the results within the context of finding operational solutions for mapping agricultural nets in South Africa.

A systematic research design was created to complete the objectives and address the aims of this study. The research will be presented in five chapters which are outlined with the research design in the following section.

## 1.7 RESEARCH DESIGN

The research is both experimental (Chapter 3) and methodological (Chapter 4) in nature. Chapters 2 and 3 report on the investigation of the spectral properties of nets and the experimentation with a range of different classification procedures respectively. The results of these exercises are used to make recommendations for developing robust operational procedures for mapping agricultural nets in the Western Cape. Empirical data, comprising digital satellite imagery, and quantitative data, comprising point (locational) samples of agricultural nets, were collected. The satellite data were used to construct a spectral profile of areas covered by agricultural nets and to develop a method for the classification of the nets. The point samples were used as reference data. Qualitative and quantitative methods were used to assess the accuracy of the classification methods.

The research is reported in five chapters as shown in Figure 1.1. Chapter 1 presents the research background, the research problem, the research aims and objectives, and the research design. In Chapter 2 the theory and practice relating to remote sensing, preprocessing techniques, classification algorithms and methods, Sentinel-2 applications and approaches to accuracy assessment are covered and reviewed. Thus Chapter 2 addresses Objective 1 and lays the theoretical foundations for Chapters 3 and 4. Chapters 3 and 4 both relate to Objective 2. The use of digital satellite (Sentinel-2) data for classification are described. Chapter 3 covers the use of Sentinel-2 imagery to construct spectral signatures of agricultural nets in the Western Cape. These signatures are used to better understand the spectral properties of nets and to investigate the effects of seasonal variation on the separability of nets, thereby addressing Objectives 3 and 4. Chapter 4 documents the use of Sentinel-2 data classification procedures for mapping table grapes under nets in the Western Cape, as envisaged by Objective 5. Quantitative and qualitative assessments of the classifications are reported. Chapters 3 and 4 are written as publication-ready, stand-alone articles. Duplication among the chapters, particularly in terms of the literature reviewed, the study area descriptions and data collection overviews, is consequently unavoidable. In Chapter 5 the study's findings are summarized, the research aims and objectives are revisited, the study's limitations are identified, recommendations are made and conclusions are drawn (Objective 6).

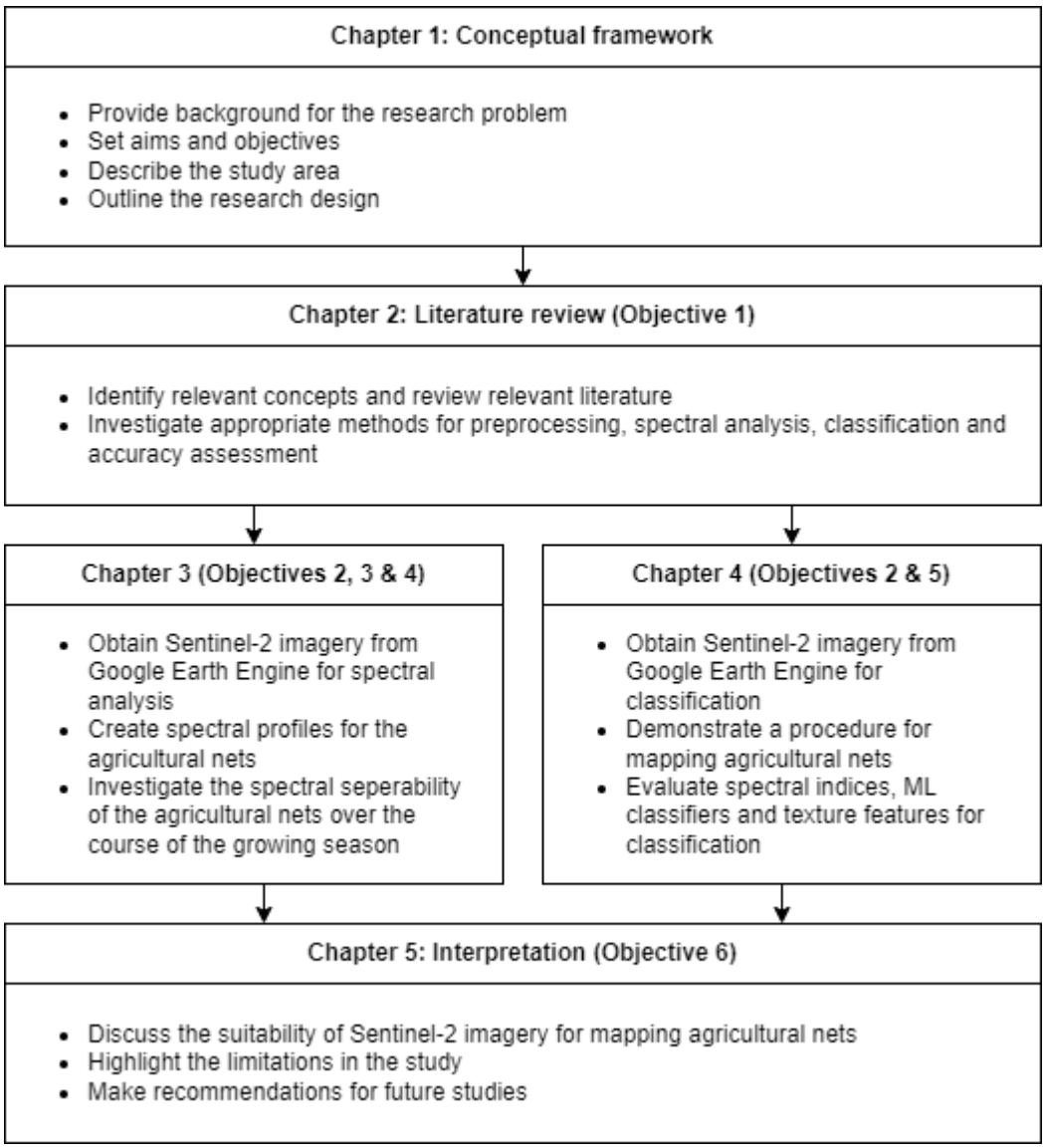


Figure 1.1 Research design

This research intents to address the need for accurate maps of agricultural nets in South Africa. Given the diverse agricultural practices in South Africa, the scope has been narrowed to focus on agricultural nets in the Western Cape and the following section provides information about the agricultural practices of this province.

## 1.8 STUDY AREA

The research will focus on agricultural nets in the Western Cape province of South Africa (Figure 1.2). The Western Cape covers an area of 12 938 600 ha of which 79% is used for agriculture as grazing and cultivated fields (DEADP 2011). The province has a typical Mediterranean climate characterised by warm, dry summers and mild winters with high rainfall (Cowling et al. 1996).

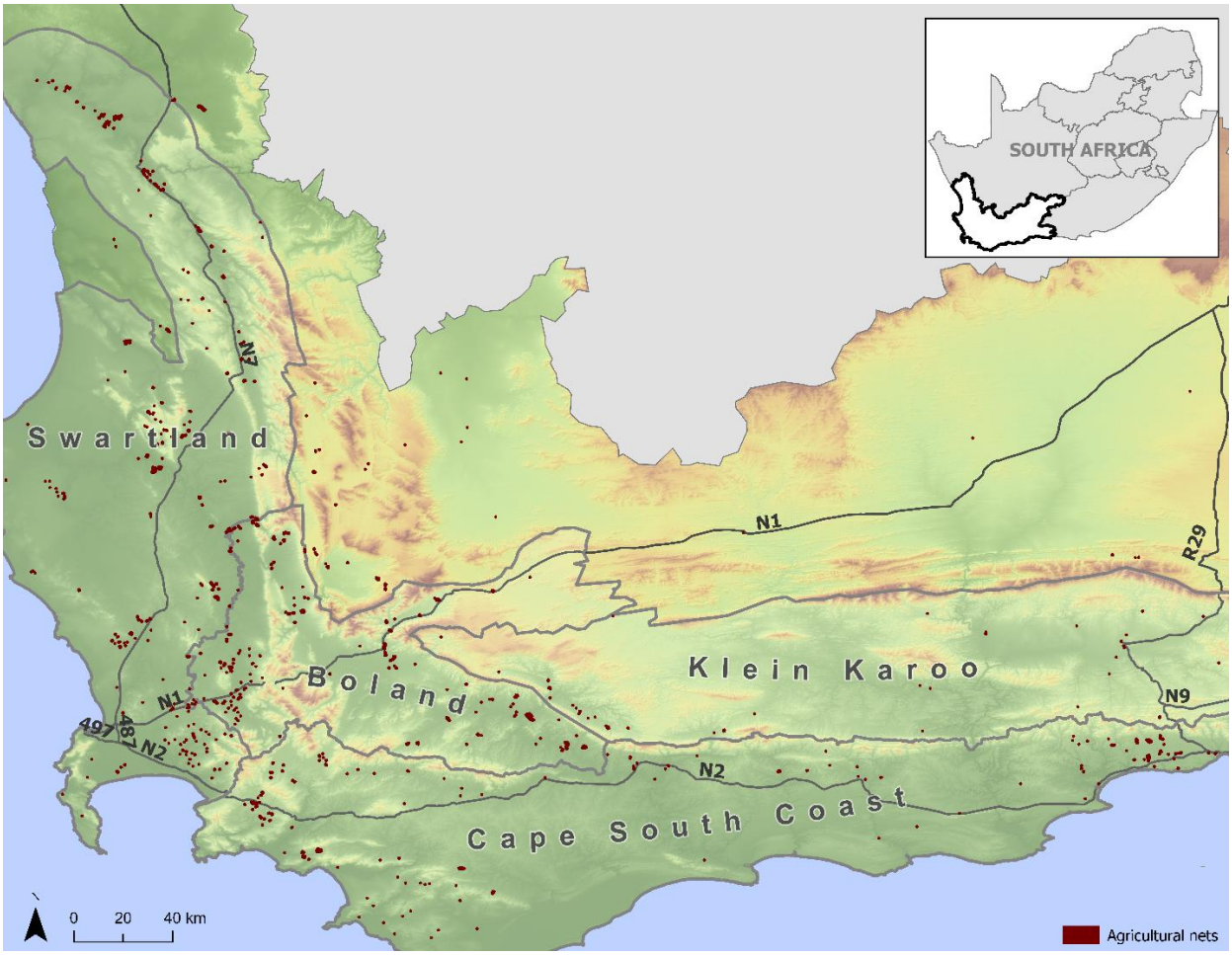


Adapted from Pienaar (2018)

Figure 1.2 Location of known agricultural nets in the Western Cape province

There are four major agricultural regions in this province: the Cape South Coast which is known for wheat, barley and intensive vegetable production; the Klein Karoo which mainly produces stone fruit, table grapes and lucerne; the Boland which primarily produces wine grapes and stone fruit; and the Swartland which is a major wheat-growing area (Vink & Tregurtha 2003). A prominent feature in these agricultural areas is the use of agricultural nets, which are the focus of this research.

## 1.9 SYNOPSIS

The current chapter has motivated the need for accurate, large-scale maps of agricultural areas, including agricultural nets, in South Africa. Research gaps around the spectral signatures of agricultural nets and the use of Sentinel-2 imagery for mapping nets have been identified. The reasons behind the selection of Sentinel-2 imagery as the focus of this research has been discussed. The aims and objectives required to address the research gaps have been stated and a clear research design and focus area have been outlined. The following chapter will investigate the literature that relate to the current study.

# CHAPTER 2: MAPPING PLASTICULTURE USING REMOTE SENSING: A LITERATURE REVIEW

A clear understanding of the concepts and theories pertaining to classification approaches, remote sensing techniques and spectral signatures is an essential prelude to mapping agricultural nets using remote sensing. In Chapter 2 these concepts are discussed and the relevant literature is reviewed in the pursuit of developing robust procedures for the mapping of agricultural nets at regional scales.

## 2.1 PRINCIPLES OF REMOTE SENSING

Remote sensing is the science of acquiring information about an object, scene or phenomenon without interacting with the intended target (Tempfli et al. 2009). Information is obtained by detecting and recording reflected energy, storing this data and interpreting the produced image (Lillesand, Kiefer & Chipman 1994). The process of remote sensing relies on five mechanisms, namely the emission of energy; the propagation of the energy through the atmosphere, the interaction of the energy with the target, the recording of the reflected energy and the interpretation and analysis of the recorded data (Campbell & Wynne 2011). In each of the following subsections a brief exposition is given of concepts relating to remote sensing and its application to crop mapping. They are, in order, the electromagnetic spectrum, atmospheric windows, active and passive sensors, digital imagery and image classification.

### 2.1.1 Electromagnetic spectrum

Remote sensing requires an energy source to capture imagery. This energy specifically refers to electromagnetic radiation (EMR) which is primarily produced by the sun (Campbell & Wynne 2011). EMR is a type of energy consisting of an electrical field and a magnetic field that oscillate at a perpendicular angle to the direction of propagation (Campbell & Wynne 2011). The electric and magnetic fields can both be conceptualized as waves that travel at the speed of light which is $3\times10^8$ m/s. EMR is classified by frequency and wavelength. The frequency of a wave, measured in hertz, is the number of waves that pass a fixed point in space in one second. Wavelength, measured in metres, is the length of a single wave cycle (Tempfli et al. 2009). The range of EMR is known as the electromagnetic spectrum (Lillesand, Kiefer & Chipman 1994). Table 2.1 lists the different divisions (principal regimes) and the corresponding wavelength intervals of the electromagnetic spectrum (Campbell & Wynne 2011).

Table 2.1 Principal regions of the electromagnetic spectrum

| Division | Wavelength range |
|---|---|
| Gamma rays | < 0.03 nm |
| X-rays | 0.03 – 300 nm |
| Ultraviolet radiation | 0.30 – 0.38 µm |
| Visible light | 0.38 – 0.72 µm |
| Near-infrared | 0.72 – 1.30 µm |
| Mid-infrared | 1.30 – 3.00 µm |
| Far-infrared | 7.00 – 1000 µm |
| Microwave region | 1 mm – 30 cm |
| Radio region | ≥ 30 cm |

Adapted from Campbell & Wynne (2011)

The regions, shown in Table 2.1, that are used for remote sensing are the visible light, near-infrared, mid-infrared and microwave regions as these regions correspond to atmospheric windows (Campbell & Wynne 2011). The concept of atmospheric windows will be explained in Subsection 2.1.2.

### 2.1.2 Atmospheric windows

Emitted EMR must travel through layers of atmosphere to reach target objects on the earth's surface (Lillesand, Kiefer & Chipman 1994). Atmospheric particles interact with the EMR through several mechanisms, including scattering and absorption (Campbell & Wynne 2011).

*Atmospheric scattering* is characterised by the redirection of EMR by atmospheric particles (Lillesand, Kiefer & Chipman 1994). The degree to which the path of the EMR is altered depends on the wavelength of the incoming radiation, the size and characteristics of the particles and the distance that the EMR must travel to reach the earth's surface. Scattering causes the atmosphere to have its own illumination which enables remote sensors to measure brightness from both the target object and the inherent illumination of the atmosphere (Kaufman et al. 1997).

*Atmospheric absorption* occurs when atmospheric particles prevent or strongly attenuate the propagation of EMR through the atmosphere (Campbell & Wynne 2011). The degree of absorption is dependent on the wavelength of the incoming radiation. Consequently, certain portions of the electromagnetic spectrum are unaffected or only partially affected by atmospheric absorption (Lillesand, Kiefer & Chipman 1994). These portions are called atmospheric windows (Figure 2.1) and are utilized in remote sensing as they allow EMR to freely move through the atmosphere and to be recorded by sensors (Tempfli et al. 2009). Figure 2.1 shows the percentage of energy that is

allowed to pass through the atmosphere (transmission) without being absorbed for each region of the electromagnetic spectrum.

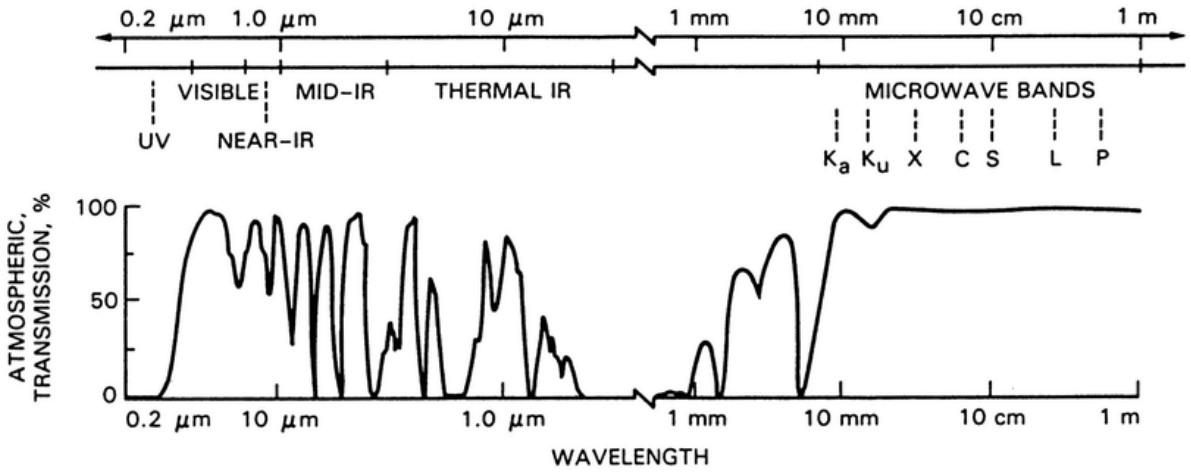


Source: Kuplich (2001)

Figure 2.1 Percentage of atmospheric transmission for each region of the electromagnetic spectrum

The atmospheric windows are located in areas of high transmission (Ketsdever 2014) and the three major atmospheric windows, shown in Figure 2.1, occur in the visible, infrared and microwave regions of the electromagnetic spectrum (Campbell & Wynne 2011). The visible and infrared regions are used by active sensors and the microwave region is used by passive sensors (Lillesand, Kiefer & Chipman 1994). Subsection 2.1.3 explains the differences between active and passive sensors.

### 2.1.3 Active and passive sensors

Sensors that record reflected or re-emitted solar energy are called passive sensors (Lillesand, Kiefer & Chipman 1994), whereas active sensors produce and record their own source of energy (Tempfli et al. 2009). Both sensor types record the intensity of certain wavelength regions to produce digital images (described in Subsection 2.1.4). Passive sensors are generally associated with optical sensors, whereas active sensors are associated with microwave sensors (Turner et al. 2003). Optical remote sensing typically utilizes wavelengths between 0.4 and 14 µm which include the visible, near-infrared, mid-infrared and far-infrared (thermal) portions of the electromagnetic spectrum (Figure 2.1). EMR from these regions primarily originate from reflected solar energy, although a portion of the far-infrared section consists of re-emitted solar energy (Turner et al. 2003). Microwave sensors are active sensors that use radar waves in the microwave portion. The region of microwave radiation is significantly larger than the optical wavelengths and ranges from 0.75 cm to 1 m (Turner et al. 2003). Both active and passive sensors record and store their

respective types of energy as digital values stored in a digital image. This process is discussed in the following subsection.

### 2.1.4 Digital imagery

Modern remote sensors use specialized instruments to systematically scan the earth's surface to create a regular grid of values that can be used to create a coherent digital image (Campbell & Wynne 2011). Digital images consist of an array of pixels each containing a single value pertaining to information about a specific location on the earth (Gibson & Power 2000). These values are usually stored as binary integers in the range 0 to 255 and are known as digital numbers (Morisette, Privette & Justice 2002). The specific characteristics of a pixel and its corresponding digital number are dependent upon the resolution of the sensor used to capture the pixel (Turner et al. 2003). The image resolution of a sensor is dependent on four separate aspects, namely spatial resolution, spectral resolution, radiometric resolution and temporal resolution (Campbell & Wynne 2011).

*Spatial resolution* is the measure of the smallest discernible object within an image and is primarily determined by the instantaneous field of view (IFOV) (Liang, Li & Wang 2012). The IFOV refers to the zone of visibility of a sensor at a given time and it determines the visible area on the ground (Morisette, Privette & Justice 2002). This area is called the resolution cell which determines the maximum spatial resolution of the sensor (Lillesand, Kiefer & Chipman 1994). Spatial resolution is measured in metres on the ground. Low spatial resolution refers to images where only large objects are visible, while high spatial resolution refers to an image where smaller objects are visible (Tempfli et al. 2009). ESA (2018) classifies sensors with a spatial resolution greater than 60 m as low-resolution, 15 m to 30 m as medium-resolution, 5 m to 15 m as high-resolution, and 30 cm to 5 m as very-high resolution.

*Spectral resolution* represents the sensor's ability to divide a received signal into wavelength intervals (Campbell & Wynne 2011). Therefore, the spectral resolution determines the number of bands that are provided by a sensor (Tempfli et al. 2009). A sensor with narrow intervals for each band is considered to have fine spectral resolution (Gibson & Power 2000). Most optical systems record EMR from more than one portion of the electromagnetic spectrum so that these systems are classified as either multispectral or hyperspectral. Multispectral sensors capture fewer bands within several separate regions of the electromagnetic spectrum, whereas hyperspectral sensors collect many narrow, near-contiguous bands (Liang, Li & Wang 2012).

*Radiometric resolution* is a sensor's ability to distinguish different brightness values within a scene (Jensen 2016). Sensors that have course radiometric resolution are less sensitive to small changes

in brightness and typically capture a scene using a small number of intensity values as opposed to an image with fine radiometric resolution that uses a large number of values (Lillesand, Kiefer & Chipman 1994). Most digital images use 255 different brightness values to capture a scene (Campbell & Wynne 2011).

*Temporal resolution* describes the length of time that passes between successive acquisitions of a single scene by a sensor (Liang, Li & Wang 2012). The ability of a sensor to capture the same scene at different periods allows a sensor to be used for monitoring changes on the earth's surface. These types of images are called multitemporal images (Tempfli et al. 2009).

### 2.1.5 Image classification

Image classification is the basis of many environmental and socio-economic applications of remote sensing (Lu & Weng 2007). The process of image classification involves grouping pixels into thematic classes based on their spectral properties (Campbell & Wynne 2011). Modern image classification involves a computer program that recognizes the relationship between the spectral information within an image and the real-life phenomenon represented by the spectral information (Li et al. 2014). Computers recognize spectral information through unsupervised or supervised learning. Unsupervised image classification is the process by which computers group pixels together based on similar features without the use of categorized training samples (Olaode et al. 2014). Features refer to the spectral attributes used to group the pixels. Unsupervised classification algorithms use clustering whereby pixels are conceptualized as vectors with multiple spectral values and grouped according to their distribution in image space (Tempfli et al. 2009). Three popular unsupervised classifiers used in remote sensing are ISODATA, k-means and modified k-means. Supervised classification uses user-defined samples of known identity to classify pixels of unknown identity (Campbell & Wynne 2011). Supervised algorithms include either statistical methods, such as minimum distance and maximum likelihood, or modern non-parametric, machine learning (ML) classifiers such as decision trees (DT), k-nearest neighbour (KNN), random forest (RF), neural networks (NN) and support vector machines (SVM).

Image classification can be conducted using either a per-pixel or an object-based approach (Li et al. 2014). Traditional per-pixel classification methods, also known as per-pixel image analysis (PPIA), group individual image pixels into thematic classes. However, as remote sensors evolved and improved in spatial resolution, per-pixel methods became incapable of handling the internal variability of complex scenes (Dey, Zhang & Zhong 2010). This led to the development of object-based image analysis (OBIA) that aggregates spectrally homogenous pixels to form image objects using image segmentation algorithms. These image objects are then individually classified based on the spectral characteristics of the entire object (Blaschke 2010). Image segmentation algorithms

are designed to divide an image into contiguous, spectrally homogenous groupings of pixels known as image objects (Espindola et al. 2006). Dey, Zhang & Zhong (2010) reviewed the suitability of several segmentation algorithms for use in optical remote sensing. They divided the segmentation algorithms into two categories, namely model-driven (top-down) algorithms and image-driven (bottom-up) algorithms.

*Image-driven* segmentation algorithms construct initial objects based solely on pixels having similar values and then use the statistical features of the objects to guide the segmentation (Tong et al. 2012). These include edge-detection algorithms, which are usually used for feature extraction, and the watershed segmentation algorithm (Dey, Zhang & Zhong 2010). Watershed segmentation regards an image as a topological surface and divides regions into theoretical catchment regions based on the pixel values (Beucher 1992). Although this algorithm is rarely used in remote sensing as it often causes oversegmentation, it is useful for segmenting images before applying multiresolution segmentation (MRS) (Beucher 1992).

*Model-driven* segmentation algorithms assume that objects exist in a predetermined pattern. The algorithm uses prior knowledge of object features (texture, shape or colour) to guide the segmentation (Cremers, Sochen & Schnörr 2006). A model-driven algorithm that has gained popularity for remote sensing applications is MRS (Dey, Zhang & Zhong 2010). This algorithm begins with an initial object (which can be a single pixel) and merges adjacent objects based on similar attributes (Darwish, Leukert & Reinhardt 2003). A user-defined homogeneity threshold that incorporates scale, shape and compactness, determines the similarity of image objects. The incorporation of these features makes the algorithm especially effective for high-resolution imagery and complex scenes (Dey, Zhang & Zhong 2010).

The preceding sections covered the fundamental theoretical concepts of image classification using remote sensing. In Section 2.2 the properties and procedures for sourcing and preprocessing Sentinel-2 imagery will be discussed in the context of mapping plasticulture.

## 2.2 AN OVERVIEW OF SENTINEL-2 IMAGERY

The various sensors that have been used to map plasticulture were discussed in Chapter 1. Several studies found that very-high-resolution imagery was effective for mapping plastic-covered agriculture (Agüera, Aguilar & Aguilar 2008; Aguilar et al. 2015; Aguilar et al. 2016; Novelli et al. 2016; Tarantino et al. 2012). But the high cost of very-high-resolution imagery makes it expensive to map large areas using this imagery (Levin et al. 2010). As a more cost-effective option, Landsat imagery was investigated to map agricultural nets. Unfortunately, the spatial resolution (30 m) of Landsat imagery was too low to map the nets with the required accuracy.

Novelli et al. (2016) established that Sentinel-2 imagery performed better than Landsat-8 imagery for mapping plastic greenhouses and they suggested the use of Sentinel-2 imagery for mapping other agricultural nets. The Sentinel-2 sensor provides free, high-resolution imagery with global coverage and presents a cost-effective option for mapping plasticulture. However, Sentinel-2 imagery has not yet been used to map agricultural nets, thus presenting the gap that warranted this research. The following subsections briefly discuss the properties of Sentinel-2 imagery and procedures for sourcing and preprocessing Sentinel-2 imagery.

### 2.2.1 Properties of Sentinel-2 imagery

The Sentinel-2 sensor provides multispectral, high spatial resolution imagery with global coverage (Drusch et al. 2012). The satellite's orbit is sun-synchronous at 716 km above the earth's surface and it has a five-day revisit period (Drusch et al. 2012). Table 2.2 records the band allocation and descriptions of the 13 Sentinel-2 bands. The bands have varying spatial resolutions that range from 10 to 60 m.

Table 2.2 Band allocation and description of Sentinel-2 imagery

| Band | Band ID | Spectral resolution (nanometres) | Spatial resolution (metres) |
|---|---|---|---|
| Coastal aerosol | 1 | 433 - 453 | 60 |
| Blue | 2 | 458 - 523 | 10 |
| Green | 3 | 543 - 578 | 10 |
| Red | 4 | 650 - 680 | 10 |
| Vegetation red edge 1 | 5 | 698 - 713 | 20 |
| Vegetation red edge 2 | 6 | 733 - 748 | 20 |
| Vegetation red edge 3 | 7 | 773 - 793 | 20 |
| Near-infrared (NIR) | 8 | 785 - 900 | 10 |
| Near-infrared narrow | 8A | 855 - 875 | 20 |
| Water vapour | 9 | 935 - 955 | 60 |
| Shortwave-infrared cirrus | 10 | 1360 - 1390 | 60 |
| Shortwave-infrared 1 (SWIR1) | 11 | 1565 - 1655 | 20 |
| Shortwave-infrared 2 (SWIR2) | 12 | 2100 - 2280 | 20 |

Adapted from Kramer (2002)

The main objectives of the Sentinel-2 mission are to provide freely available imagery for three European mapping services and seven information services (Drusch et al. 2012). The European Land Monitoring Service (EUROLAND) uses Sentinel-2 imagery to monitor land cover change

and urban development. The Biophysical Parameter Service (BioPar) uses the imagery to classify continental vegetation, monitor the energy budget and model the water cycle. The Seasonal and Annual Change Monitoring Service (SATChMo) aims to provide seasonal, Europe-wide land cover data and land cover change data. The information services for which the Sentinel-2 sensor were designed aim to provide data for spatial planning, agri-environmental monitoring, water monitoring, forest monitoring, land carbon estimation, natural resource monitoring in Africa, and global crop monitoring (Drusch et al. 2012). Consequently, Sentinel-2 imagery has become an essential tool for a number of research applications, including the classification of plastic-mulched land cover (PML) (Lu, Tao & Di 2018) and the classification of plastic greenhouses (Aguilar et al. 2016). Sentinel-2 imagery can be obtained from several sourced and requires preprocessing to be used for land cover classification. Subsection 2.2.2 explores the sources and preprocessing procedures that have been used for Sentinel-2 imagery as a precursor for plasticulture mapping.

### 2.2.2 Preprocessing and sources of Sentinel-2 imagery

Preprocessing is the sequence of corrective operations conducted to prepare raw remote sensing imagery for analysis. The two most common operations are radiometric and geometric correction (Campbell & Wynne 2011). Radiometric correction ensures that the digital numbers in a scene accurately represent the reflected radiation from the surface (Russ 1995). These adjustments are necessary to address radiometric interference caused by factors like variations in illumination, shadows, sensor noise, sensor error, atmospheric conditions or atmospheric scattering (Campbell & Wynne 2011). By contrast geometric correction rectifies errors caused by the inherent relationship between sensor geometry and Earth geometry. This correction also converts data from image coordinates to real-world coordinates (Russ 1995).

The European Space Agency (ESA) supplies Sentinel-2 imagery that has undergone different levels of preprocessing. Level 0 and Level 1A data products provide raw compressed and uncompressed data respectively. Level 1B products have been radiometrically corrected and converted to radiance values. Level 1B products are used to collect ground control points (GCPs) for geometric correction. Level 1C products consist of orthorectified top of atmosphere (TOA) reflectance values that have been resampled to create a regular grid of pixels. ESA provides several options to convert the TOA reflectance values to bottom of atmosphere (BOA) reflectance values, this additional step produces the Level 2A product.

Another popular source of Sentinel-2 imagery is Google Earth Engine (GEE). GEE is a cloud-computing platform created to aid the analysis of spatial data (Mutanga & Kumar 2019). This platform hosts imagery from a variety of different satellites, including both Level 1C and Level 2A Sentinel-2 imagery (Pahlefi, Danoedoro & Kamal 2021). Level 2A products are derived from

the Level 1C products by running Sen2Cor, an atmospheric correction processor. This processor was designed specifically to transform single-date, Level 1C products, which represent TOA reflection, to Level 2A products that represent surface reflection (Main-Knorn et al. 2017). Lu, Tao & Di (2018) used Level 2A Sentinel-2 imagery, obtained from the Copernicus Open Access Hub, to map PML cover in Xinjiang, China. Borgogno-Mondino, Palma & Novello (2020) acquired Level 1C Sentinel-2 imagery from GEE and used the Sen2Cor algorithm to convert the digital numbers to surface values. The imagery was used to extract the spectral signatures of plastic-covered vineyards. Data preprocessing is an essential prelude to data analysis. The following sections will discuss different image analysis techniques, including image transformation and image classification.

## 2.3 IMAGE TRANSFORMATION FEATURES USED FOR MAPPING PLASTICULTURE

Image transformation describes a set of functions whereby the spectral information within a scene is modified to highlight specific characteristics (Campbell & Wynne 2011). The Hughes effect, first described by Hughes (1968), explains the decrease in accuracy that occurs when too many variables are considered for classification. According to Lu & Weng (2007), image transformation methods aid classification by addressing the Hughes effect, as these operations reduce redundant information by extracting pertinent spectral data to create new features. Digital image processing offers a nearly limitless range of image transformation techniques, including spectral indices and texture features (Russ 1995). Owing to their significance in plasticulture mapping, a selection of spectral indices is discussed in the next subsection, followed by attention given to textural features and feature selection.

### 2.3.1 Spectral indices

Spectral indices are linear combinations of spectral bands that indicate the relative abundance of features of interest (Jackson 1983). According to Jensen (2016), a spectral index must: (1) be scalable to indicate the abundance of a particular land cover; (2) normalize or reduce noise to allow consistent spatial comparison; and (3) apply to specific and measurable surface phenomena. Spectral indices were initially developed using simple band ratios to visualize the growth of vegetation. Vegetated areas present a unique spectral challenge as they represent complex scenes that are influenced by growth cycles, soil brightness, moisture and environmental factors (Russ 1995). More than 40 different vegetation indices have been proposed to enhance the response of vegetation while reducing the influence of the above factors. Vegetation indices are based on the notion that vegetation has a high reflectance in the near-infrared (NIR) portion of the EMS and a

low reflectance in the red portion of the spectrum owing to the reaction of chlorophyll to EMR (Campbell & Wynne 2011). The following subsections will examine spectral indices that have been used for mapping plasticulture, starting with vegetation indices and then exploring indices relating to other land cover.

#### 2.3.1.1 Vegetation indices

Basic vegetation indices are computationally simple and effective for the identification of healthy vegetation. However, they fail to compensate for factors such as soil brightness and atmospheric interference (Russ 1995). The NDVI is the most widely used basic vegetation index in remote sensing (Jensen 2016). The index is expressed as:

$$NDVI = \frac{(NIR-RED)}{(NIR+RED)} \qquad \text{Equation 2.1}$$

where NDVI is the normalized difference vegetation index;

NIR is the near-infrared band; and

RED is the red band.

The NDVI is a normalized index with a range between -1 and 1, where values closer to 1 indicate the presence of healthy vegetation (Xue & Su 2017). Jia et al. (2014) showed that the inclusion of the NDVI as a feature for land cover mapping not only improved the classification accuracy by a statistically significant degree, but also aided in vegetation type discrimination. Belgiu & Csillik (2018) made use of the NDVI to decrease the dimensionality of a large multitemporal data set for crop classification. This approach was successful and achieved an average overall accuracy of over 86%. Hasituya & Chen (2017) found that the NDVI contributed significantly toward increasing the classification accuracy while mapping PML. In contrast, Perilla & Mas (2019) found that the NDVI increased the confusion between vegetation, plastic greenhouses and nets.

One limitation of the NDVI is that this index is sensitive to the effects of soil brightness, atmospheric brightness, cloud cover and shadow (Xue & Su 2017). These limitations led to the development of additional indices that consider soil and atmospheric brightness (Bannari et al. 1995). Kaufman & Tanre (1992) proposed the atmospheric resistant vegetation index (ARVI). This index was based on the idea that the red band is affected by the atmosphere to a larger degree than the NIR band due to the difference in their wavelengths. The index compensates for atmospheric brightness by modifying the red band value with the difference in brightness between the red and the blue bands. The ARVI is expressed as:

$$ARVI = \frac{NIR-((2\times RED)-BLUE)}{NIR+((2\times RED)-BLUE)}$$ Equation 2.2

where ARVI is the atmospheric resistant vegetation index;

NIR is the near-infrared band;

RED is the red band; and

BLUE is the blue band.

According to Kaufman & Tanre (1992), the ARVI shares a similar dynamic range with the NDVI, but it is four times less sensitive to atmospheric brightness. However, the index's accuracy decreases when vegetation is sparse due to the increased effect of soil brightness (Bannari et al. 1995). Soil brightness has a major effect on the computation of soil indices (Bannari et al. 1995). Consequently, indices such as the NDVI or the ARVI, which both fail to compensate for soil brightness, have limitations when applied to scenarios of sparse vegetation. Huete (1988) addressed these limitations by developing the soil-adjusted vegetation index (SAVI) that considers the soil characteristics of the target scene. The SAVI index is expressed as:

$$SAVI = \frac{NIR - RED}{NIR + RED + L} \times (1 + L)$$ Equation 2.3

where SAVI is the soil-adjusted vegetation index;

NIR is the near-infrared band;

RED is the red band; and

L is the relative soil constant.

Both Panda et al. (2010) and Vani & Mandla (2017) compared the use of the SAVI to other vegetation indices, including the NDVI, for land cover classification. Vani & Mandla (2017) found that the NDVI outperformed the SAVI for indicating relative vegetation abundance in all cases, except for semi-arid areas. Similarly, Panda et al. (2010) concluded that the effect of soil brightness is negligible is cases of high vegetation abundance and found that the NDVI outperformed the SAVI. Liu & Huete (1995) speculated that the atmosphere and soil brightness interact with vegetation in a complex manner which cannot be modelled independently by indices such as the SAVI or the ARVI. They proposed a new index, the enhanced vegetation index (EVI), that uses a feedback mechanism that simultaneously compensates for atmospheric and soil brightness. The EVI is expressed as:

$$EVI = G \times \frac{NIR - RED}{NIR + C1(RED) - C2(BLUE) + L}$$ Equation 2.4

where EVI is the enhanced vegetation index;

G is the canopy background adjustment;

NIR is the near-infrared band;

RED is the red band;

BLUE is the blue image band;

C1 is the first aerosol-resistant coefficient;

C2 is the second aerosol-resistant coefficient; and

L is the canopy background adjustment factor.

Ahmad (2012) compared the EVI, the SAVI and the NDVI for the classification of land cover. The EVI achieved the best classification accuracy when using coefficients values of: L = 1, C1 = 6, C2 = 7.5 and G = 2.5. Arvor et al. (2011) employed the EVI successfully for land cover classification but found that the performance of the EVI was dependent on how well the coefficient values were able to model the target scene.

#### 2.3.1.2 Indices relating to other land cover types

Indices such as the NDVI, the SAVI and the EVI are aimed at the detection of the abundance of vegetation. However, spectral indices can be used to detect the relative abundance of a number of different phenomena, such as plastic-covered agriculture (Xue & Su 2017). Tarantino et al. (2012) determined that the visible atmospherically resistant index (VARI) was the most important feature, compared to spectral bands and texture features, in mapping plastic-covered vineyards using aerial imagery. The VARI is expressed as:

$$VARI = \frac{GREEN - RED}{GREEN + RED - BLUE}$$ Equation 2.5

where GREEN is the green band;

RED is the red band; and

BLUE is the blue band.

The advantage of the VARI is that it only uses spectra within the visible portion of the EMS, thus making it applicable to a wide range of sensors, including true-colour aerial imagery. However,

Tarantino et al. (2012) also criticized the index as it did not use several plastic absorption features identified by Levin et al. (2010).

Lu, Di & Ye (2014) proposed an index that discriminates PML in a decision-based classifier. Their plastic-mulched land cover index (PMLI) is expressed as:

$$PMLI = \frac{NIR-GREEN}{NIR+GREEN} \quad \text{Equation 2.6}$$

where PMLI is the plastic-mulched land cover index;

NIR is the near-infrared band; and

GREEN is the green band.

Lu, Di & Ye (2014) classified the PMLI values greater than 0.69 as PML. The classification achieved an accuracy of 78% for the PML class. Both the PMLI and the VARI have been criticized by Yang et al. (2017) for failing to capture the dynamic spectral nature of plasticulture structures that changes over time, is highly dependent on the crops that the structures cover and resembles man-made surfaces both spectrally and texturally. Yang et al. (2017) developed the plastic greenhouse index (PGI) to compensate for the limitations of the PMLI and the VARI. The index is based on the results of spectral separability analyses conducted on plastic greenhouses in the target scene using Landsat-8 imagery. The PGI is expressed as:

$$PGI = 100 \times \frac{BLUE \times (NIR-RED)}{1-Mean(BLUE+GREEN+RED)} \quad \text{Equation 2.7}$$

where PGI is the plastic greenhouse index;

NIR is the near-infrared band;

Blue is the blue band; and

RED is the red band.

Perilla & Mas (2019) determined that the PMLI and the PGI did not significantly increase the separability between surrounding land cover and protected agriculture, including agricultural nets. Novelli & Tarantino (2015) looked to Landsat-8 OLI and TIRS imagery to create an index that accounts for different types of plastic coverings for crops. The index, known as the plastic surface index (PSI), utilizes the thermal bands of the TIRS sensor to identify plastic coverings that increase the temperature over crops (Novelli & Tarantino 2015). The index is expressed as:

$$PSI = \frac{RED - \left(\frac{BT + SWIR}{2}\right)}{RED + \left(\frac{BT + SWIR}{2}\right)}$$ Equation 2.8

where RED is the red band;

SWIR2 is the SWIR band; and

BT is the rescaled brightness temperature.

BT is calculated as:

$$BT = \frac{T - T_{min}}{T_{max} - T_{min}}$$ Equation 2.9

where T is the brightness temperature;

$T_{min}$ is the minimum brightness temperature for the study area; and

$T_{max}$ is the maximum brightness temperature for the study area.

The index contributes significantly to the separability between the plasticulture classes and the surrounding land cover classes. However, the use of the thermal bands limits the usability of this index as thermal bands are not typically available for multispectral sensors (Novelli & Tarantino 2015). Aside from spectral indices, spectral texture is also exploited to aid image classification. A brief introduction of texture features and their application to mapping plasticulture is given in Subsection 2.3.2.

### 2.3.2 Texture features

Li et al. (2012) define image texture as the visual effect caused by spatial variation in tonal quantity over relatively small areas. In the field of remote sensing, a number of texture features have been developed to identify and analyse surface objects (Haralick, Shanmugam & Dinstein 1973).

Haralick, Shanmugam & Dinstein (1973) proposed a set of 14 statistical texture features that exploit the grey-level co-occurrence matrix (GLCM) and the grey-level difference vector (GLDV) of imagery to extract texture features. These methods have since become the main approaches to texture analysis (Agüera, Aguilar & Aguilar 2008). Many scholars have used texture features to aid the classification of plastic greenhouses. Carvajal et al. (2006) investigated the use of texture features, specifically employing the GLCM method, for the per-pixel classification of greenhouses using QuickBird imagery. Although the addition of the texture features improved the overall accuracy by an average of two percent, the margin of increase was deemed insignificant compared to the additional processing time required to compute the texture features. They noted that the

texture model parameters, specifically window size, significantly affected the performance of the classification. Sothe et al. (2017) used texture features for mapping successional forest stages. They determined that a seven-by-seven pixel window size produced the best results using Sentinel-2 imagery. Zheng et al. (2017) and Pandit, Tsuyuki & Dube (2020) also recommended a seven-by-seven pixel window size when creating texture features for land cover classification using Sentinel-2 imagery. Similarly, Agüera, Aguilar & Aguilar (2008) conducted a per-pixel classification of plastic greenhouses using ten GLCM texture features, namely homogeneity, contrast, dissimilarity, mean, standard deviation, entropy, angular second moment (ASM), correlation, GLDV ASM and GLDV entropy. The texture features made no significant improvement to classification accuracy. Carvajal et al. (2006) found that most of the texture features did not aid the classification of greenhouses. However, the inclusion of the mean feature did decrease the errors of commission, and the ASM feature decreased errors of omission in the greenhouse class. Texture features have also been used in object-based classification of greenhouses. For example, Chaofan et al. (2016) compared WorldView-2 and Landsat-8 for mapping plastic greenhouses and found that texture features increased the accuracy by a small margin, but this margin was insignificant for the Landsat-8 imagery. Aguilar et al. (2014), Aguilar et al. (2015) and Aguilar et al. (2016) similarly concluded that texture features made no significant difference to classification accuracy when mapping plastic greenhouses. In contrast to these results, Tarantino et al. (2012) employed texture features to map plastic nets with very-high-resolution aerial imagery. They used feature space optimization for feature selection and the ASM of the blue band was shown to facilitate the classification significantly.

Spectral indices and texture features can significantly improve the spectral separability of classes when used with spectral bands. However, the addition of ancillary classification features can increase the dimensionality of feature sets which can decrease classification accuracy (Guyon & Elisseeff 2003). Feature selection addresses this problem and will be discussed in the following subsection.

### 2.3.3 Feature selection

Feature selection methods are used to reduce the dimensionality of feature sets by eliminating redundant features in the preparations for classification (Guyon & Elisseeff 2003). These methods are deemed important in modern classification practices as they improve the performance of ML classifiers that can be sensitive to high dimensionality. Furthermore, feature selection reduces the computational power and time required to classify large data sets (Ma et al. 2017). According to Guyon & Elisseeff (2003), feature selection methods can be grouped into three categories, namely wrapper, filter and embedded methods. Wrapper methods use existing ML algorithms to select

features that achieve the highest classification accuracy (Stromann et al. 2019). Filters rank features according to a statistical metric and remove the low-scoring features. Embedded methods find the best preforming subset of features during classifier training (Guyon & Elisseeff 2003).

A number of feature selection approaches have been used to improve the accuracy of plasticulture classifications. Tarantino et al. (2012) used the feature space optimization (FSO) tool to select the optimum set of features for classifying vineyard nets using aerial imagery. The algorithm selected the VARI spectral index and the ASM texture feature of the blue band for classification (Tarantino et al. 2012). Hasituya & Chen (2017) used RF feature ranking, a wrapper method, to select features for mapping PML using Landsat-8 imagery. The results showed that the spectral bands were the most important for classification compared to the spectral indices and texture features, although the mean texture feature also ranked high. Specifically, the visible and SWIR1 bands were ranked the highest. The results also indicated that the importance of features changed throughout the growing season of the vegetation under the PML. Both Tarantino et al. (2012) and Hasituya & Chen (2017) found that the use of feature selection methods improved the accuracy of classification and provided valuable insight about which features were most appropriate for the classification. The appropriate selection of features is highly dependent on which ML algorithm is used for classification (Guyon & Elisseeff 2003). In Section 2.4, several ML algorithms that have been used to classify plasticulture are discussed.

## 2.4 MACHINE LEARNING CLASSIFIERS

ML classifiers are a group of algorithms that construct classification models based on information provided by labelled training data (Talukdar et al. 2020). These models are used to classify unlabelled pixels into the specified thematic classes. The ability of ML classifiers to model complex classification problems have resulted in their extensive application in the field of remote sensing (Lary et al. 2016). In the following two subsections some common ML algorithms used for land cover classification are introduced first and then several ML classifiers for mapping plasticulture are compared.

### 2.4.1 Introduction to machine learning algorithms

The ML algorithms that have been applied to land cover mapping problems, including plasticulture mapping, are DT, RF, support vector machine (SVM) and NN. The following paragraphs outline each of these ML algorithms and point out their advantages and disadvantages.

DTs are supervised classifiers that use a series of binary rules to assign pixels or objects to classes (Safavian & Landgrebe 1991). Univariant DTs consider a single feature at decision nodes, whereas a multivariant DT considers multiple features at decision nodes (Yildiz & Alpaydin 2012). DTs

are computationally efficient, make no-statistical assumptions about the data and can classify a range of different data types (Pal & Mather 2003). However, the algorithm has been criticized for its lack of transferability, it's inability to classify data in high-dimensional feature space and for being prone to overfitting. The accuracy of the classification is also heavily dependent on the selection of features (Nair & Bindhu 2016).

SVMs have become popular for a number of remote sensing applications, especially those where limited training data are available (Mountrakis, Im & Ogole 2011). The classifier is a supervised, non-parametric ML algorithm that aims to separate training samples in feature space using a statistical hyperplane. This hyperplane can be based on a number of kernel functions, including linear, polynomial or radial basis function (RBF) (Mountrakis, Im & Ogole 2011). The performance of SVMs is greatly dependent on the appropriate selection of the kernel function for a particular application (Kavzoglu & Colkesen 2009). SVMs are sensitive to outliers and the performance can decrease significantly if the training data are noisy or if the classes have similar spectral characteristics (Mountrakis, Im & Ogole 2011).

RF has rapidly become one of the most popular classifiers for remote sensing applications (Belgiu & Drăguţ 2016). RF is an ensemble classifier, because it uses a number of different models to conduct a classification (Waske & Braun 2009). RF uses a set of DTs, which are constructed from a subset of the training samples to classify objects or pixels. The training sample set is usually split with two thirds being used to train the classifier and the remaining one third used to validate the model (Belgiu & Drăguţ 2016). The two important features that separate RF classifiers from simple DT classifiers are: (1) each tree built by RF uses a random subset of the training samples selected with replacement; and (2) each node in a tree uses a random subset of features to create the binary split (Horing 2010). Furthermore, unlike DTs, RF is less sensitive to the input parameters, less prone to overfitting and automatically determines the accuracy of the model and the importance of the variables used (Horing 2010).

NN is a complex ML algorithm that mimics the human brain. It uses multiple layers of decision nodes (resembling neurons) to classify image objects or pixels (Atkinson & Tatnall 1997). NNs are effective for image classification owing to their ability to classify complex data sets with varying statistical distributions, incorporating prior knowledge to the problem, and handling different data types (Atkinson & Tatnall 1997). However, NNs have been used less frequently than algorithms such as RF and SVM for image classification because parameter selection for NNs is difficult. The algorithm is also difficult to implement, it is processing intensive and the model is sensitive to the selection of features (Mas & Flores 2008).

### 2.4.2 Comparison of machine learning classifiers used for plasticulture mapping

Lu, Di & Ye (2014) used a univariant DT to classify PML using the NDVI and the PMLI as classification features. This DT classification achieved an overall accuracy of 97% and concluded that DTS are effective for mapping PML. However, the study concluded that the DT model was not transferable and it achieved low accuracies when applied to a different scene. Aguilar et al. (2015) used a DT for an object-based classification of crops under plastic greenhouses. The classification included multitemporal Landsat images, texture features and vegetation indices to classify the greenhouses, achieving an overall accuracy of 81%. Two other studies that recommend the use of DT classifiers for mapping plasticulture are those by Aguilar et al. (2015) and Aguilar et al. (2016).

Hasituya et al. (2016) used Landsat-8 imagery to test the effect of different kernel functions and feature sets for the classification of PML using SVMs. The linear function produced the highest overall accuracy of 93% using both spectral and texture features. Chaofan et al. (2016) also used the linear kernel for SVMs to classify plastic greenhouses with Landsat-8 imagery. The classification achieved an overall accuracy of 91.5%. Lanorte et al. (2017) used an SVM and selected the RBF as a kernel function with Landsat-8 imagery to map plastic films and nets and achieved an overall accuracy of 87%. Other studies in which SVMs were used for mapping plasticulture are those of Lu, Tao & Di (2018) and Hasituya & Chen (2017).

RF has been extensively used to map plasticulture, including PML and plastic greenhouses (Hasituya et al. 2016; Hasituya & Chen 2017; Lu, Tao & Di 2018; Novelli & Tarantino 2015). Lu, Tao & Di (2018) compared RF and SVM for object-based mapping of PML using Sentinel-1 and Sentinel-2 imagery. The highest overall classification accuracy was achieved by SVM using spectral indices, spectral bands and texture features as input, although the difference in classification accuracy between RF and SVM was marginal (1.5%). The most important Sentinel-2 features were the NDVI, band 8 and band 1. Hasituya & Chen (2017) compared RF and SVM for per-pixel PML mapping using Landsat-8 data and found that RF significantly outperformed SVM. Both classifications were carried out using EnMAP-Box, which is a tool used for image classification. Novelli et al. (2016) used RF for an object-based classification of plastic greenhouses. RF was implemented using STATISTICAv10® with 500 trees as a precautionary value. The method produced an accuracy of 91% using Sentinel-2 imagery for both segmentation and classification.

Carvajal et al. (2006) employed a NN to detect plastic greenhouses. The classification accuracy improved when texture features were used and achieved an overall accuracy of 85%. Shao & Lunetta (2012) found that SVM outperformed NN for land cover classification when limited training data was available. The results of SVM were more reliable when different features were used for classification. Sun et al. (2021) applied an NN to classify plastic greenhouses with Sentinel-2 imagery. The method achieved an average overall accuracy of 87% using single-date imagery and 91% using multitemporal imagery. ML algorithms have been used in both pixel- and object-based classification. In Section 2.4, these approaches are compared for mapping plasticulture.

## 2.5 PER-PIXEL AND OBJECT-BASED APPROACHES FOR MAPPING PLASTICULTURE

The effectiveness of object-based classification has been demonstrated for a number of classification applications, including plasticulture mapping (Aguilar et al. 2015; Aguilar et al. 2016; Aguilar et al. 2018; Chaofan et al. 2016; González-Yebra et al. 2018; Lu, Tao & Di 2018; Novelli et al. 2016; Tarantino et al. 2012). The object-based classification approach achieved accuracies greater than 90% for mapping plastic nets (Tarantino et al. 2012) and plastic greenhouses (Aguilar et al. 2018) when using very-high-resolution imagery. However, poorer accuracies were achieved with low-resolution imagery. For instance, when Chaofan et al. (2016) used Landsat-8 imagery for the object-based classification of plastic greenhouses, the highest overall accuracy achieved was 85%. In attempts to improve the accuracies of plasticulture classifications using low-resolution imagery, several scholars have used low-resolution imagery in combination with very-high-resolution imagery (Aguilar et al. 2015; González-Yebra et al. 2018; Novelli et al. 2016). Both Aguilar et al. (2015) and Novelli et al. (2016) explored WorldView-2 imagery during the segmentation process, after which the objects were classified using Landsat-8 and Sentinel-2 imagery. Novelli et al. (2016) reported a significant increase in classification accuracy, especially for the greenhouse class, when using WorldView-2 for segmentation. In following a similar approach, González-Yebra et al. (2018) used very-high-resolution orthoimagery to create segmentation objects for plastic greenhouses and then conducted the classification using Landsat-8 imagery. A different method was proposed by Lu, Tao & Di (2018), who used both Sentinel-1 and Sentinel-2 imagery to classify PML to achieve an overall accuracy of 94%.

Most authors that used object-based classificaion for plasticulture successfully applied the MRS algorithm for segmentation (Aguilar et al. 2015; Aguilar et al. 2016; Aguilar et al. 2018; Chaofan et al. 2016; González-Yebra et al. 2018; Novelli et al. 2016). However, the success rate of MRS is

highly dependent on the selection of appropriate parameters (Dey, Zhang & Zhong 2010). Smith (2010) proposed a method to optimize the selection of the scale parameter by using the RF algorithm. The method was used to identify three critical image object scales that were successfully applied to classify land cover using 11 SPOT scenes, with an average accuracy of 85%. Drăguţ, Tiede & Levick (2010) developed a tool called estimation of scale parameter (ESP) to determine the optimal scale parameter for MRS. The tool iteratively creates image objects at different scales by calculating the local variance for each scale. The most appropriate scale is selected based on the rate of change of the local variance. The authors concluded that the method is robust and accurate. Novelli et al. (2016) developed an open-source tool called AssesSeg. The tool uses an adjusted version of the Euclidean distance 2 (ED2) supervised discrepancy measure to estimate the MRS segmentation parameters from Sentinel-2, Landsat-8 and WorldView-2 imagery. AssesSeg was subsequently applied by González-Yebra et al. (2018) to estimate the segmentation parameters for mapping plastic greenhouses using Landsat-5 and Landsat-7 imagery.

Due to the major issue of parameter selection for OBIA, a number of scholars have experimented with per-pixel classification to map plasticulture (Agüera, Aguilar & Aguilar 2008; Carvajal et al. 2006; Hasituya & Chen 2017; Lanorte et al. 2017; Lu, Di & Ye 2014; Novelli & Tarantino 2015; Yang et al. 2017). Lanorte et al. (2017), for example, mapped plastic films and nets using Landsat-8 imagery. The classification achieved an accuracy of 95%. Yang et al. (2017) achieved an average overall accuracy of 92% using Landsat ETM+ imagery to map plastic greenhouses. Hasituya & Chen (2017) achieved an overall accuracy of 97% using multitemporal Landsat-8 imagery for mapping PML. Sun et al. (2021) achieved an average overall accuracy of 87% using a single Sentinel-2 image and 91% using multitemporal imagery when conducting a per-pixel classification of both PML and plastic greenhouses. In order to compare different classification procedures, robust methods for accuracy assessments are required. Accuracy assessment approaches will be explored in Section 2.6.

## 2.6 ACCURACY ASSESMENT

In the field of remote sensing, accuracy is the term used to describe the degree to which a map or image correctly portrays reality (Foody 2002). Accuracy assessments are required to ascertain the quality and usability of data for thematic classification maps (Congalton 1991). According to Millard & Richardson (2015) the accuracy of a classification depends on the training sample size, the number of classes in the classification, the sampling scheme and the accuracy metric being used. These factors, as they relate to land cover classification, are discussed in the following subsections.

### 2.6.1 Training samples

Training and validation data, collectively known as ground truth data, are closely related and can be sourced from the same image or independent data sources (Curran & Williamson 1985). The quality of this data affects the training of the classifier as well as the validity of the accuracy assessment (Millard & Richardson 2015). It is therefore vital that careful consideration must be given to the collection of ground truth data, the sample size and the sampling scheme (Congalton 1991).

Training data can be collected from various sources like field surveys, digitized vector data, aerial imagery, satellite imagery or thematic maps. These sources differ in terms of accessibility, accuracy and applicability. There are many different approaches to the collection of training data and the appropriate approach depends on the nature of the classification and the accuracy metric being used (Congalton 1991). Guidelines have been established to promote the collection of applicable training samples (Curran & Williamson 1985; Millard & Richardson 2015; Zhou 1996). Curran & Williamson (1985) emphasized the importance of representative ground truth data, stating that samples should have sufficient representation of each training class and account for the variation within a class. Therefore, they recommended that samples are balanced between classes and that samples should be collected at the same scale as the spatial resolution of the ground truth imagery (Curran & Williamson 1986). Zhou (1996) agreed with the approach recommended by Curran & Williamson (1985), but found fault with the traditional method of manual, visual interpretation in the collection of ground truth data. They proposed that manually collected training samples must be analysed for spectral separability before they are used for training or validation. This ensures that the classifier is able to distinguish different classes and serves as a method to test the quality of training samples (Zhou 1996).

The appropriate sample size for both training and validation is a much debated topic among scholars (Congalton 1991; Curran & Williamson 1986; Curran & Williamson 1985; Foody 2002; Millard & Richardson 2015). Traditional methods used the distribution of values in a scene to estimate the number of samples required for training and validation. The estimations were based on the variations within the scene (Congalton 1991). But, this method failed to recommend a number of samples that reflected the confusion between classes and therefore could not be used to produce an error matrix (Fitzpatrick-Lins 1981). Fitzpatrick-Lins (1981) recommended the use of a normal approximation equation to determine a larger number of samples that meet the statistical requirements of an error matrix. Although this method produced statistically sound results, Congalton (1991) regarded the method to be impracticable when time and cost were considered. As an alternative, Congalton (1991) recommended 50 samples per class for areas smaller than 1

million acres and 75 or 100 samples per class for larger areas. Subsequently, Li et al. (2014) compared 15 classification algorithms using Landsat TM data for land cover classification in an exercise to determine the effect of training sample size on classifier accuracy. The larger sample sets (>200) preformed the best for all classifiers, however for RF and SVM the difference in accuracy between 100 samples and 240 samples was less than 3%. Moreover, Li et al. (2014) advised that achieving representative samples of each class was more important than collecting a large number of samples.

Sampling schemes are categorized according to the spatial distributions of samples (Curran & Williamson 1985). A poor sampling scheme selection may lead to bias or the undersampling of certain classes, ultimately resulting in the over- or underestimation of error in a classification (Congalton 1991). Although there is disagreement among scholars about the best sampling scheme, simple random, stratified random and cluster sampling schemes are the most popular for assessing land cover classifications (Congalton 1991; Curran & Williamson 1985; Plourde & Congalton 2003). Campbell & Wynne (2011) describe simple random sampling as the generation of random sample points in a manner that every area in a scene has an equal probability of being sampled. Stratified random sampling divides the study area into strata based on the classes and then generates points randomly within the strata. Cluster sampling generates cluster centres and then assigns sample points around the centres. According to Congalton (1991), simple random sampling provides the most unbiased samples, but it tends to under sample certain classes. Stratified random sampling is recommended by Plourde & Congalton (2003) as this method ensures that all classes are represented and it contains minimal bias as points are distributed randomly within classes. Curran & Williamson (1985) endorsed cluster sampling because this scheme considers time, cost and accessibility constraints. Congalton (1991) prescribes that clusters should contain no more than ten points so as to avoid errors caused by spatial autocorrelation. Once representative samples have been collected, these samples must be analysed using accuracy metrics. In Subsection 2.6.2, different measures of accuracy will be described and evaluated.

### 2.6.2 Measures of accuracy

The approaches to accuracy assessment in remote sensing have progressed in type from qualitative visual interpretation to locational, quantitative methods (Congalton 1991). The modern, quantitative methods are grouped into descriptive (user's accuracy, producer's accuracy, overall accuracy, balanced accuracy), analytical (kappa statistic) and statistical significance measures (McNemar test, Z-score) (Congalton 1991). In the following three subsections, each of these metrics are discussed in turn.

#### 2.6.2.1 Descriptive measures

The use of an error matrix is the most common descriptive method used in remote sensing (Janssen & Van der Wel 1994). An error matrix refers to a cross-tabulation method that compares the class labels of classified pixels with the labels of reference pixels (Foody 2002). Image objects can be used as accuracy assessment units, but for the sake of brevity the term ‘pixels’ is henceforth used for all types of units.

Confusion matrices indicate inter-class confusion that can be used to adjust classifications to improve accuracy. Three accuracy measures can be derived from an accuracy matrix, namely user’s accuracy, producer’s accuracy and overall accuracy (Foody 2002). *User’s accuracy* is calculated as the number of correctly classified samples divided by the total number of pixels in a class produced by the classification data. Users accuracy relates to the errors of omission in a class which are the pixels that belong to a particular class that have been misclassified and therefore omitted from the true class (Campbell & Wynne 2011). A user’s accuracy of 80% for X means that 80% of the pixels labelled as X represent class X in reality (Janssen & Van der Wel 1994).

*Producer’s accuracy* is calculated by dividing the number of correctly classified pixels of a class by the total number of pixels within that class reported by the reference data (Janssen & Van der Wel 1994). Producer’s accuracy is an indication of the errors of commission present in a data set. Errors of commission are pixels that have been misclassified and committed to the wrong class (Campbell & Wynne 2011). A producer’s accuracy of 80% indicates that 80% of the pixels that represent class X in reality have been correctly classified as X (Janssen & Van der Wel 1994).

*Overall accuracy* is the most widely used measure for indicating classification accuracy (Carfagna & Gallego 2006). This measure is calculated by dividing the total number of correctly classified pixels by the total number of pixels in the error matrix (Campbell & Wynne 2011). Overall accuracy indicates the general agreement between the classification and the real-life phenomenon that the classes aim to represent (Congalton 1991). Many researchers have used per-pixel confusion matrices with overall, producer’s and consumer’s accuracy as their accuracy metrics (Aguilar et al. 2015; Chaofan et al. 2016; González-Yebra et al. 2018; Hasituya & Chen 2017; Lu, Di & Ye 2014; Lu, Tao & Di 2018; Novelli et al. 2016). Novelli & Tarantino (2015) used a confusion matrix to assess the classification accuracy of plastic-covered vineyards. Instead of collecting validation samples for each class, they commend the use of a binary mask that gives a better indication of the success of the proposed methodology for mapping vineyard nets in particular. The binary mask is used to construct a binary confusion matrix which indicates the level of agreement between the mask and the classified nets (Novelli & Tarantino 2015).

Regarding binary classification, McKeown et al. (1999) proposed three additional summary statistics that can be derived from the confusion matrix, namely the detection percentage, branching factor and quality percentage. Detection percentage is the portion of pixels correctly classified as the target class. The branching factor is the number of pixels incorrectly classified as the target class for every correctly classified pixel. Quality percentage is a measure of overall classification quality which, unlike overall accuracy, accounts for all misclassifications (McKeown et al. 1999). Agüera, Aguilar & Aguilar (2008) employed detection percentage, branching factor and quality percentage measures to compare the performance of QuickBird and IKONOS for the detection of plastic greenhouses. These metrics do not, however, compensate for binary classifications with imbalanced classes. Tharwat (2018) advocates the use of the balanced accuracy (BA) metric, which combines sensitivity and specificity to compensate for unbalanced classes. Sensitivity, also known as the true positive rate, is the positive detection rate compared to the total number of positive samples (Luque et al. 2019). In the context of plasticulture, sensitivity is the total number of identified plastic coverings in relation to the total number of pixels that represent plastic coverings. Specificity, or the true negative rate, is the ratio of correctly classified negative values to the total number of negative values. Regarding plasticulture mapping, specificity is the total number of pixels correctly classified as non-plastic coverings compared to the total number of non-plastic covering pixels. BA considers both these metrics and is expressed as:

$$BA = \frac{1}{2}\left(\frac{TP}{TP+FN} + \frac{TN}{TN+FP}\right) \qquad \text{Equation 2.10}$$

where $TP$ is the number of correctly classified positive values;

$FN$ is the number of falsely classified negative pixels;

$TN$ is the number of correctly classified negative values; and

$FP$ is the number of falsely classified positive values.

#### 2.6.2.2 Analytical measures

The kappa statistic, first proposed by Cohen (1960), is a popular analytical measure of classification accuracy (Campbell & Wynne 2011). Kappa (κ) quantifies the difference between the observed agreement between two data sets and the agreement between the data sets obtained per chance (Campbell & Wynne 2011). Congalton (1991) and Fitzpatrick-Lins (1981) regard the kappa statistic as a superior measure of accuracy to the overall accuracy because kappa

compensates for chance agreement which occurs frequently in spatial data sets due to spatial autocorrelation. The kappa statistic is calculated using the following equation:

$$\hat{k} = \frac{n\sum_{i=1}^{n} X_{ii} - \sum_{i=i}^{n} X_{i+}X_{+i}}{n^2 - \sum_{i=i}^{n} X_{i+}X_{+i}} \qquad \text{Equation 2.11}$$

where $\hat{k}$ is the kappa statistic;

$n$ is the sample size;

$X_{ii}$ is the observed agreement; and

$X_{i+}$ and $X_{+i}$ are the estimates of expected agreement for each category.

Fitzgerald & Lees (1994) tested the ability of the kappa statistic and overall accuracy to capture the known agreement between two data sets. Kappa emerged as the more effective method, as the statistic modelled the agreement more accurately. Nonetheless, many scholars still prefer to use both the kappa statistic and overall accuracy to quantify the quality of their land cover classifications (Huang, Davis & Townshend 2002; Manandhar et al. 2009; Rodriguez-Galiano et al. 2012). González-Yebra et al. (2018) used the kappa statistic for the accuracy assessment of their classification of plastic greenhouses.

#### 2.6.2.3 Measures of statistical significance

Apart from accuracy measures such as the kappa statistic and overall accuracy, additional measures have been considered to determine whether the differences between classification accuracies are statistically significant (Bostanci & Bostanci 2013). Two such measures are the McNemar's test and the Z-test. The McNemar test, first proposed by (McNemar 1974), is a non-parametric statistical test applied to paired nominal data. The test produces a P-value which describes the statistical significance between the paired data which, in the case of land cover classification, is the difference between two classification results (Bostanci & Bostanci 2013). The McNemar test has been recommended by Foody (2002), Manandhar et al. (2009), and Rodriguez-Galiano et al. (2012) to determine the statistical validity of differences in accuracy results.

Hasituya & Chen (2017) suggested the use of the Z-test to measure statistical significance between kappa statistic values when comparing the accuracy of different feature sets and image dates for mapping PML. The Z-test is a flexible metric that allows the comparison of classifications which use different types of imagery, those conducted with different acquisition times or those using

different classification algorithms (Congalton & Green 2009). This metric assumes a normal distribution thus excluding its use for skewed data sets (Hasituya & Chen 2017).

The most effective accuracy assessment approaches use descriptive measures, analytical measures and statistical measures together. The use of a confusion matrix is the most popular method of accuracy assessment in land cover classification. The inclusion of confusion matrix metrics, especially OA, therefore allows classification procedures to be compared to methods used by other scholars through a common metric (Janssen & Van der Wel 1994). Analytical and statistical measures then provide useful information that, when used in conjunction with descriptive measures, provides a more wholistic view of the quality of the classifications.

The accuracy of classifications is affected by several factors. One major factor is whether the imagery used for classification has the necessary resolution to capture distinguishable signatures of the classes in the study area (Tempfli et al. 2009). As such, classification accuracy is an indication of how suitable a sensor is for a particular purpose. Another indicator of how well a sensor is able to capture a particular phenomenon is through spectral analysis (Herold, Gardner & Roberts 2003). The following section covers methods of spectral analysis and how these methods have been used to investigate the spectral properties plasticulture.

## 2.7 SPECTRAL ANALYSIS OF PLASTICULTURE

Remote sensors can measure the spectral response of an object over a range of wavelengths, which can be visualized as a spectral curve known as a spectral signature (Campbell & Wynne 2011). The specific characteristics of an object's spectral signature can be used to identify or classify the objects in a scene (Tempfli et al. 2009). However, the success of the classification is highly dependant on how well the classification strategy can separate and identify unique spectral signatures. Spectral seperability refers to how easily spectral signatures from different land cover types can be distinguished (Herold, Gardner & Roberts 2003). The following subsections will cover studies that have investigated the spectral signatures of plasticulture, followed by a discussion of spectral separability measures and how they have been applied to plasticulture.

### 2.7.1 Spectral properties of plasticulture

Aside from the hyperspectral sensors discussed in the first chapter, a number of multispectral sensors have also been employed to investigate the spectral properties of plastic-covered agriculture (Borgogno-Mondino, Palma & Novello 2020; Hasituya & Chen 2017; Lu, Di & Ye 2014; Tarantino et al. 2012; Yang et al. 2017).

Lu, Di & Ye (2014) have, for example, extracted the average radiance per regions of interest (ROI) for eight land cover classes using Landsat-5 TM imagery. An analysis of these spectral signatures was applied to create rules to classify PML and to select spectral indices to aid classification. The PML signatures that were obtained at the beginning of the growing season closely resembled the fallow land and bare land classes. However, the PML signatures were significantly different from the water and crop classes (Lu, Di & Ye 2014). Hasituya & Chen (2017) extracted the spectral signatures of five land cover types using Landsat-8 imagery over a five-month period. The signatures were created using the average reflectance of 40 pixels per class. The spectral signatures changed dramatically over the course of the five months due to crop growth. The PML signatures closely resembled bare ground at the beginning of the growing season and then changed to resemble vegetation toward the end of the growing season. Consequently, scholars recommend multitemporal imagery for discriminating plastic films from vegetation. Yang et al. (2017) used Landsat ETM+ imagery to analyse the spectral properties of plastic greenhouses to facilitate the development of a spectral index. Spectral signatures were constructed for eight classes, including cropland, plastic greenhouses and soil, by sampling 20 pixels per class. The signatures indicated that (1) plastic greenhouses had higher reflectance than uncovered crops and bare fields over the visible spectrum; (2) the NIR-red slope is relatively independent of the presence of plastic greenhouses; (3) the greenhouse signatures closely resembled the shape of the crop signatures; and (4) the blue band is the most effective for separating plastic greenhouses and crops. Tarantino et al. (2012) achieved similar results while investigating plastic vineyard nets using very-high-resolution aerial imagery. The signatures for nets resembled the shape of the uncovered vineyards, but reflectance was higher for the red, green and blue bands. The reflectance difference in the blue band was the most significant for discriminating nets from other classes. Borgogno-Mondino, Palma & Novello (2020) used Sentinel-2 imagery to extract spectral signatures from covered and uncovered vineyards. Although the results showed higher reflectance values for the covered vineyards, the shape of the covered vineyards resembled that of the uncovered vineyards. They concluded that the Sentinel-2 sensor was able to capture a reliable signature of crops under nets.

### 2.7.2 Spectral separability of plasticulture

The ability of a sensor to distinguish between the spectral signatures of different land cover classes is dependent on the differences between the signatures (Herold, Gardner & Roberts 2003). Various approaches can be followed to quantify the differences between spectral signatures (Richards & Jia 2006). Two popular approaches are statistical measures and distance measures (Schmidt & Skidmore 2003). Statistical measures, such as the Mann-Whitney U-test, determine whether the differences between spectral signatures are statistically significant. These measures therefore

provide a good indication of the ability of a sensor to capture objects at a spectral resolution acceptable for classification (Schmidt & Skidmore 2003). The Mann-Whitney U-test is a non-parametric test and does not assume that the samples have a normal distribution. The test determines whether the variance within classes is significantly greater than the variance between classes (Artigas & Yang 2006). Schmidt & Skidmore (2003) relied on the Mann-Whitney U-test to identify wavelength intervals that could be used to differentiate between different species of coastal vegetation. A significance level of 0.01 was applied and it was found that more than 75% of the species were separable for most of the wavelength intervals. Using a significance level of 0.01 is popular for testing the statistical significance of seperability measures (Artigas & Yang 2006; Van Til, Bijlmer & De Lange 2004). Amani et al. (2018) compared the use of RapidEye imagery, Sentinel-2 imagery, ASTER imagery and Landsat-8 imagery for mapping wetland types. The Mann-Whitney U-test was applied to determine each sensor's ability to discriminate between different wetland types. The measure was also used to compare the ability of different indices, texture features and spectral bands to increase the separability between classes. A significance level of 0.05 was specified. Matongera et al. (2017) employed a similar method to determine suitable features for vegetation mapping using Landsat-8 OLI. Another study that turned to the Mann-Whitney U-test to investigate spectral signatures is that of Van Til, Bijlmer & De Lange (2004).

Distance measures quantify the distance between object spectra in feature space (Schmidt & Skidmore 2003). Gunal & Edizkan (2008) have described three distance measures frequently used to quantify spectral separability, namely Bhattacharyya distance, Jeffries-Matusita (JM) distance, and transformed divergence (TD). The less frequently used Mahalanobis distance quantifies the distance between two measurements in multivariant feature space (Richards 1993). Bhattacharyya distance is similar to Mahalanobis distance but with no assumption that the standard deviation between two samples is equal. In remote sensing the Bhattacharyya distance is often incorporated with JM distance which uses the Bhattacharyya distance to rank features for feature selection (Qiu et al. 2014). JM distance is a parametric measure that makes use of the distance between class means and the distribution of class values to determine class separation (Dabboor et al. 2014). JM distance is calculated by:

$$JM_{ij} = 2(1 - e^{-B}) \qquad \text{Equation 2.12}$$

where $B$ represents the Bhattacharyya distance, expressed as:

$$B = \frac{1}{8}(m_i - m_j)^t \left\{\frac{\sum i + \sum j}{2}\right\}^{-1} (m_i - m_j) + \frac{1}{2}\ln\left\{\frac{\left|\frac{(\sum i + \sum j)}{2}\right|}{\sqrt{|\sum i||\sum j|}}\right\}$$ Equation 2.13

where $i$ and $j$ are the two class signatures;

$m_i$ and $m_j$ are the mean vectors of signatures i and j; and

$\sum i$ and $\sum j$ are the covariance matrices of signatures i and j.

Transformed divergence (TD) quantifies spectral distance by decreasing the weights given to classes as the spectral distance between classes increases (Jensen 2016). This algorithm is computationally more effective than the Bhattacharyya and JM distance measures and is calculated with the following formula:

$$TD_{ij} = 2000(1 - e^{-\frac{d_{ij}}{8}})$$ Equation 2.14

where

$$d_{ij} = \frac{1}{2}tr\{(C_i - C_j)(C_j^{-1} - C_i^{-1})\} + \frac{1}{2}tr\{(C_i^{-1} + C_j^{-1})(m_i - m_j)(m_i - m_j)^t\}$$ Equation 2.15

where $i$ and $j$ are the two class signatures;

$tr$ is the trace function;

$m_i$ and $m_j$ are the mean vectors of signatures i and j; and

$C$ is the covariance matrix of each class.

Both TD and JM range from 0 to 2. According to Jensen (2016), classes that achieve a score of 1.9 are considered to have good separation, while scores lower that 1.7 indicate poor separability.

TD and JM distance have both been used for the spectral analysis of plasticulture. Perilla & Mas (2019) used TD to determine which band combinations of Sentinel-2 imagery increased the separability between protected agriculture (which included nets and plastic greenhouses) and surrounding land cover. The bands that produced the highest separability, and subsequently used for classification, were Blue, NIR, SWIR1, SWIR2 (Perilla & Mas 2019). Lanorte et al. (2017) used JM to access the quality of classifier training samples. They noted a very high degree of separability between the net and plastic film classes. However, the separation between the plasticulture (net and film) classes and the vegetation class was low. It should be noted that the

samples were acquired towards the end of the growing season of the crops under the plastic nets and films, which affects the class seperability (Lanorte et al. 2017).

The literature revised in the preceding paragraphs prove that agricultural nets have complex spectral signatures that are affected by the sensor used to capture the signatures, the physical properties of the nets and the spectral characteristics of the crops under the nets. The insights gained through the study of these spectral properties, and their separability from surrounding land cover, have proved invaluable to inform classification strategies.

## 2.8 SYNOPSIS

This chapter has provided a review of the literature on remote sensing and image classification, specifically as the latter applies to the classification of plasticulture. The contents relate directly to Objective 1 as they provide insight into the properties of agricultural nets, multispectral classification techniques and the approaches to accuracy assessment. Technical topics such as spectral signatures, spectral indices, texture features and classification algorithms have been explored to build a foundation for the strategies developed in the next chapters.

Objective 2 is to acquire appropriate remotely sensed data and collect suitable reference data for spectral analysis, classifier training and accuracy assessment. Although very-high-resolution imagery is effective for mapping plasticulture, it is evident that a knowledge gap exists regarding the use of Sentinel-2 imagery for mapping agricultural nets. The vital advantages of Sentinel-2 imagery are the accessibility of imagery, the global coverage, the short revisit time and the superior spectral and spatial resolutions of Sentinel-2 imagery compared to other freely available data such as Landsat imagery. Therefore, Sentinel-2 imagery will be acquired to capture and distinguish the spectral signatures of agricultural nets and to demonstrate the potential of Sentinel-2 for mapping plasticulture. The literature confirms GEE to be a valuable platform for obtaining level 2A Sentinel-2 products for spectral analysis and classification (Amani et al. 2020).

Objectives 3 and 4 respectively aim to develop a spectral profile of agricultural nets in the Western Cape using Sentinel-2 multispectral imagery and to describe the influence underlying crops have on the spectral signatures of agricultural nets. Agricultural nets have diverse spectral properties (Levin et al. 2010). It is important to understand the spectral variation of nets and how variation changes over time to inform crucial decisions about the optimal time of the year to map nets, which classification scheme to use and which ancillary features to include. Borgogno-Mondino, Palma & Novello's (2020) investigation of the differences between covered and uncovered vineyards over the course of a year has confirmed that the signatures of the covered vineyards do change over time. Regrettably, they did not compare the spectral signatures to surrounding land cover nor

investigate the seperability of the covered vineyards. The analyses in Chapter 3 are devoted to comparing the spectral signatures of various covered crops with their uncovered counterparts to further our understanding of the relationships between the spectral signatures of agricultural nets and the underlying crops based on Sentinel-2 imagery. Perilla & Mas (2019) used the JM algorithm to quantify the seperability of their classes to inform feature selection for plasticulture mapping. In this study the JM algorithm will be used to compare the separability of agricultural nets from surrounding land cover over the course of a year. The results of these exercises will lay the foundation for addressing Objective 5 in Chapter 4.

Objective 5 aims to develop and demonstrate a method for mapping nets using Sentinel-2 imagery. According to the literature several ML algorithms have been applied to map plasticulture. RF and SVM have been used frequently to map plastic greenhouses and PML (Chaofan et al. 2016; Hasituya et al. 2016; Lu, Tao & Di 2018). The linear kernel emerged as the most effective function for mapping plastic greenhouses and PML using SVM (Hasituya et al. 2016; Lanorte et al. 2017). NN has been proven effective for mapping plastic greenhouses using Sentinel-2 imagery (Sun et al. 2021). However, the RF, SVM and NN algorithms have not yet been used to classify agricultural nets, so there is a research gap regarding the performance of RF, SVM and NN for mapping agricultural nets using Sentinel-2 imagery. The challenge of filling this gap is taken up in Chapter 4. Per-pixel and object-based approaches have been followed in other studies to map plasticulture. The OBIA approaches were effective when using VHR imagery but achieved lower accuracies than per-pixel classification using medium-resolution Landsat imagery. Additionally, parameter selection for segmentation is also presented as a limitation of OBIA. This justified the choice of per-pixel classification applied in Chapter 4.

The addition of spectral indices and texture features to aid the classification of plasticulture has yielded varying degrees of success. For example, Hasituya & Chen (2017) found that NDVI contributed significantly to the classification accuracy for mapping PML using Landsat-8 imagery with RF and SVM classifiers, whereas Perilla & Mas (2019) experienced that NDVI, PMLI and PGI made no significant impact on the classification accuracy of mapping plasticulture (including nets) using Sentinel-2 imagery and the maximum entropy classifier. The current study's evaluation of the NDVI, the SAVI, the EVI, the PMLI and the PGI for classifying agricultural nets in the Western Cape is reported in Chapter 4. The investigation of the performance of these indices has never been done using RF, SVM and ANN classifiers and Sentinel-2 imagery in the Western Cape. The usefulness of GLCM texture features in the classification of nets was demonstrated by Tarantino et al. (2012). Texture features have also been shown to improve the performance of ANN for mapping plastic greenhouses (Carvajal et al. 2006). Chapter 4 reports on the performance

of texture features for the classification of nets. The addition of spectral indices and texture features increases the number of classification features which can decrease classification accuracy due to the Hughes effect (Hughes 1968). RF feature ranking will be used to select features for classification as this algorithm provides valuable insights about the importance of features for classification accuracy. Hasituya & Chen (2017) and Hasituya et al. (2016) have corroborated the effectiveness of RF feature ranking in feature selection to improve the classification accuracy in mapping PML.

Classification accuracy can be measured by several different methods of which the error matrix is the most routinely used (Foody 2002). The classification exercise done in Chapter 4 aims to map agricultural nets. Novelli & Tarantino's (2015) used a mask, indicating the presence and absence of plasticulture, to construct a binary error matrix for accuracy assessment. This approach highlighted the ability of the classification strategy to distinguish plasticulture from surrounding land cover and is therefore appropriate for the current study. Similarly, the validated use of the overall accuracy and kappa statistic metrics to evaluate the classification accuracy by Aguilar et al. (2015), Chaofan et al. (2016), González-Yebra et al. (2018), Hasituya & Chen (2017), Lu, Di & Ye (2014), Lu, Tao & Di (2018) and Novelli et al. (2016) justifies the use of these two metrics for evaluating the classifications of agricultural nets in Chapter 4. The BA metric, designed to compensate for unbalanced binary confusion matrices, is adopted in this study because the classification deals with an unbalanced error matrix. The McNemar test for statistical significance will be used to determine whether the results of the different classification strategies (in terms of feature selection and ML algorithm) are statistically different. This will allow the performance of the different classifiers and feature sets to be compared accurately.

In the final chapter, the key findings of the current study will be discussed and the potential of Sentinel-2 imagery as a source of data for mapping agricultural nets will be evaluated. So completing Objective 6 by interpreting the results within the context of finding operational solutions for mapping agricultural nets in South Africa.

# CHAPTER 3: SPECTRAL AND TEMPORAL ANALYSIS OF AGRICULTURAL NETS USING SENTINEL-2 IMAGERY[1]

## 3.1 ABSTRACT

The use of agricultural nets has increased rapidly worldwide. Consequently, the study of these nets has become popular in remote sensing. However, the mapping of nets presents several challenges due to their diverse spectral properties. Understanding these spectral properties is essential for developing an operational mapping solution. This study's primary aim is to investigate the spectral properties of agricultural nets using Sentinel-2 imagery. The secondary aim is to gain insight into the effect of seasonal variability on the spectral signatures of nets. Sentinel-2 imagery was acquired from 1 June 2019 to 30 May 2020 for 12 test sites in the Western Cape province of South Africa. The imagery was used to extract the spectral signatures of nets covering grape, citrus and berry crops as well as for surrounding land cover. The spectral signatures of the covered crops were compared with the uncovered signatures of the same crop type. The Jeffries-Matusita (JM) distance was calculated for different combinations of crop types and land cover for each acquisition period. Reliable signatures of crops under nets were obtained using Sentinel-2 imagery so confirming the potential of Sentinel-2 imagery for mapping crops under nets. Summer was shown to be the best time to map nets in the Western Cape, because that is when the crops under the nets reach maturity and present unique spectral characteristics that make their spectral signatures easier to separate. The results provide valuable insight into the spectral dynamics of nets, particularly in the Western Cape, that can be exploited to develop an operational solution for mapping nets at regional scale.

## 3.2 INTRODUCTION

The study of agricultural nets has become increasingly popular in the field of remote sensing (Al-Helal & Abdel-Ghany 2011; Blanco et al. 2018; Lanorte et al. 2017; Levin et al. 2010). This newfound interest stems from the extensive and steadily expanding use of nets worldwide (Levin et al. 2010). The advantages of agricultural nets are increased yields, earlier harvests, the reduced need for pesticide and herbicide applications, protection from extreme weather conditions such as wind, hail and frost, a decreased need for irrigation and the improvement of crop quality (Scarascia-Mugnozzo, Sica & Russo 2011). Nets are used for a variety of applications and they differ in terms of their physical and spectral properties. The nets are therefore difficult to detect and to map using remotely sensed data, particularly when using multispectral sensors (Levin et al.

[1] This chapter is formatted as a standalone, publication-ready article. Some duplication with Chapters 2 and 4 should consequently be expected.

2010). Levin et al. (2010) have described two major challenges associated with the unique spectral characteristics of agricultural nets. First, the spectral properties of nets vary over time due to dust accumulation and the change of the vegetation spectra under semi-transparent nets. Second, the variations in plastic compound, thickness, density, transparency and colour of nets result in different spectral signatures recorded for the agricultural nets (Levin et al. 2010).

Several studies have investigated the spectral response of agricultural nets using remote sensing. Most of these studies used hyperspectral sensors to investigate the signatures (Hörig et al. 2001; Kühn, Oppermann & Hörig 2004; Levin et al. 2010; Shahak et al. 2004; Sica & Picuno 2008). These studies led to the identification of a number of absorption features at 1218, 1732, 1800 and 2320 nm, which facilitated the classification of agricultural nets with hyperspectral imagery (Agüera, Aguilar & Aguilar 2008; Aguilar et al. 2014; Arcidiacono & Porto 2012; Carvajal et al. 2010; Tarantino et al. 2012). Levin et al. (2010) found the spectral resolution of Landsat-7 to be too low to detect these absorption features. Yang et al. (2017) compared the separability of plastic greenhouses to surrounding land cover using Landsat TM and ETM+ imagery with the goal being to identify Landsat bands that improve the separability of the plastic-covered crops and uncovered crops. The visible and near-infrared (NIR) bands turned out to be the most important bands for separating plastic greenhouses from the bare soil and urban classes (Yang et al. 2017) and the shortwave-infrared (SWIR) region proved the most effective for separating greenhouses from fields planted with crops (Yang et al. 2017). Borgogno-Mondino, Palma & Novello (2020) compared the spectral signatures of covered and uncovered vineyards using Sentinel-2 imagery to determine whether the spectral and spatial resolutions of Sentinel-2 were adequate to detect a reliable signature of vineyards through the nets. They found that nets do not limit the monitoring of covered vineyards using Sentinel-2 imagery. However, none of these studies investigated the separability of net signatures captured by the Sentinel-2 sensor.

Spectral separability describes how easily spectral signatures can be differentiated by classifiers (Richards & Jia 2006). Wicaksono & Aryaguna (2020) determined that high spectral separability between classes significantly improved the overall accuracy of the classification, especially when machine learning (ML) classifiers were used. Therefore, to map agricultural nets successfully the net signatures must be spectrally separable from surrounding land cover. This requires high inter-class spectral variability and low intra-class spectral variability (Aplin 2004). Intra-class variation is the spectral variation of samples within a single class (Debba, Cho & Mathieu 2009), whereas inter-class variation refers to the spectral variation between different land cover classes (Debba, Cho & Mathieu 2009). Debba, Cho & Mathieu (2009) observed that land cover with high intra-class variation resulted in lower accuracies for such classes.

The spectral variation within and among land cover classes is affected by several factors, namely the temporal variation of land cover, the classification scheme, the selection of training samples and the resolution of the sensor (Carrao et al. 2007; Debba, Cho & Mathieu 2009; Guerschman et al. 2003; Wicaksono & Aryaguna 2020). Hu et al. (2017) noted that the overall accuracies of their land cover classification differed by as much as 30% depending on the phenological stage of the crops being mapped. Other studies in which significant effects of seasonal variation on classification accuracy have been listed are those by Hestir et al. (2008), Dudley et al. (2015) and Guerschman et al. (2003). Most of the studies investigating methods to map plasticulture have used imagery acquired when the crops planted under the nets are mature (Aguilar et al. 2014; González-Yebra et al. 2018; Novelli et al. 2016; Tarantino et al. 2012; Yang et al. 2017) so that little is known about the impact seasonal variations may have on classification accuracy. One exception is the work by Aguilar et al. (2015) in which crops under nets were mapped for different times in the growing season in southern Spain. Significant differences in overall accuracy among the different dates were produced, with the imagery acquired during August producing the highest accuracies.

The selection of training classes and the collection of training samples play crucial roles in ensuring that classes are distinguishable (Wicaksono & Aryaguna 2020). Guerschman et al. (2003) concluded that the number of training classes impacts largely on the accuracy of land cover classifications, their results showing that inter-class separability decreased as the number of classes increased, so resulting in poorer accuracies for classifications with more classes. Consequently, the mapping of plasticulture has witnessed the use of various approaches for class selection. Tarantino et al. (2012), for example, excluded urban and water land covers from their classification scheme due to an insufficiency of training samples available for these classes in their study area. The selected classes included agricultural nets, bare soil, crops and natural vegetation, resulting in an overall accuracy of 90% (Tarantino et al. 2012). Lanorte et al. (2017) and Aguilar et al. (2014) did include urban land cover as a class for mapping plasticulture, but both studies noted significant confusion between the bare soil, agricultural nets and urban classes. Clearly, more investigations of the spectral separability of agricultural nets from other land cover classes are required to determine which classification scheme is most suitable for mapping plasticulture.

Class separability is further affected by the resolution of the imaging sensor and not all systems have the requisite resolution for capturing the spectral information to effectively map certain land cover features (Wicaksono & Aryaguna 2020). Carrao et al. (2007) and Mishra et al. (2012) have underlined this importance of high spatial resolution to increase spectral separability between land cover classes and Carrao et al. (2007) went even further by noting that high spatial resolution

contributed significantly more to classification accuracy than does improved spectral resolution. This conclusion is supported by Herold, Gardner & Roberts (2003) who found that higher spectral resolution imagery improves the classification of complex spectral classes only marginally.

The use of agricultural nets has increased rapidly in recent years in South Africa with an estimated area of 2 400 ha in 2016 (Pienaar 2018). The proliferation of these nets has complicated the application of existing remote sensing methods for mapping and monitoring agricultural land use and practices (Van Niekerk et al. 2018). The development of a solution to the problem of mapping crops under agricultural nets is essential to improved farm management and agricultural policy making. The Sentinel-2 mission, launched in 2014 to provide high-resolution imagery for land cover mapping and monitoring (Phiri et al. 2020), potentially provides a practical resolution to the issue of mapping and monitoring agricultural nets at regional scales. However, it is still unclear whether the spectral and physical properties of nets, as they relate to the spectral and spatial resolution of Sentinel-2 imagery, are suitable.

The primary aim of this article is to analyse the spectral signatures (as captured by Sentinel-2 imagery) of different types of agricultural nets and crops that they cover. The study evaluates the ability of Sentinel-2 imagery to spectrally discern different agricultural nets from surrounding land cover. The purpose of this exercise is to determine whether Sentinel-2 imagery has sufficient spectral and spatial resolutions to distinguish between covered and uncovered crops of the same type, and between different netted crops and other types of land cover. The secondary aim is to investigate the effect of seasonal variation on the intra- and inter-class separability of agricultural nets. The results are interpreted in the context of finding an operational solution for mapping and monitoring agricultural nets, and the crops they cover, over large and complex regions such as the Western Cape.

## 3.3 METHODS

In the following subsections, the methods that were used to achieve the aims of the present study are outlined. Specifically, the following will be explained: how the test sites were selected, the phenology of the crops relevant to the study, how Sentinel-2 imagery and ground samples were obtained and how the separability analysis was conducted.

### 3.3.1 Study area

The Western Cape province, which covers an area of 129 370 km$^2$, is the study area. This province is situated on the south-western edge of South Africa where the southern and western coastal boundaries are bordered by the warm Mozambique current and the cold Benguela current respectively (Van Niekerk & Joubert 2011). These currents, along with the diverse topography of

the province, have resulted in a unique climatic profile (Du Plessis 2017). The study area is divided into four main climate regions, namely the South Coast, the Klein Karoo, the Boland, and the Swartland (Van Niekerk & Joubert 2011). This diversity of climates allows for a variety of agricultural practices, including the growing of grains, fruits, vegetables, and nuts (Pienaar 2018).

The Western Cape's agricultural sector is estimated to contribute R25 billion to South Africa's GDP (Vink & Tregurtha 2003). Vink & Tregurtha (2003) specifically highlight the fruit industry as the backbone of the agricultural economy in the Western Cape. The fruit cultivars grown in the study area are especially sensitive to climatic variations with high yields being largely dependent on cold winters and sufficient water availability during the dry, hot summers (GreenAgri 2016). As a result, Western Cape farmers have had to find innovative ways to address the variable rainfall, increased temperatures and extreme weather conditions caused by climate change. One such strategy is the use of agricultural nets (Bryan et al. 2009). In the Western Cape, fruit varieties make up 88% of crops under nets, with grape, citrus and berry varieties prevalent (Pienaar 2018). Consequently, these three crop types were chosen as the focus of this study.

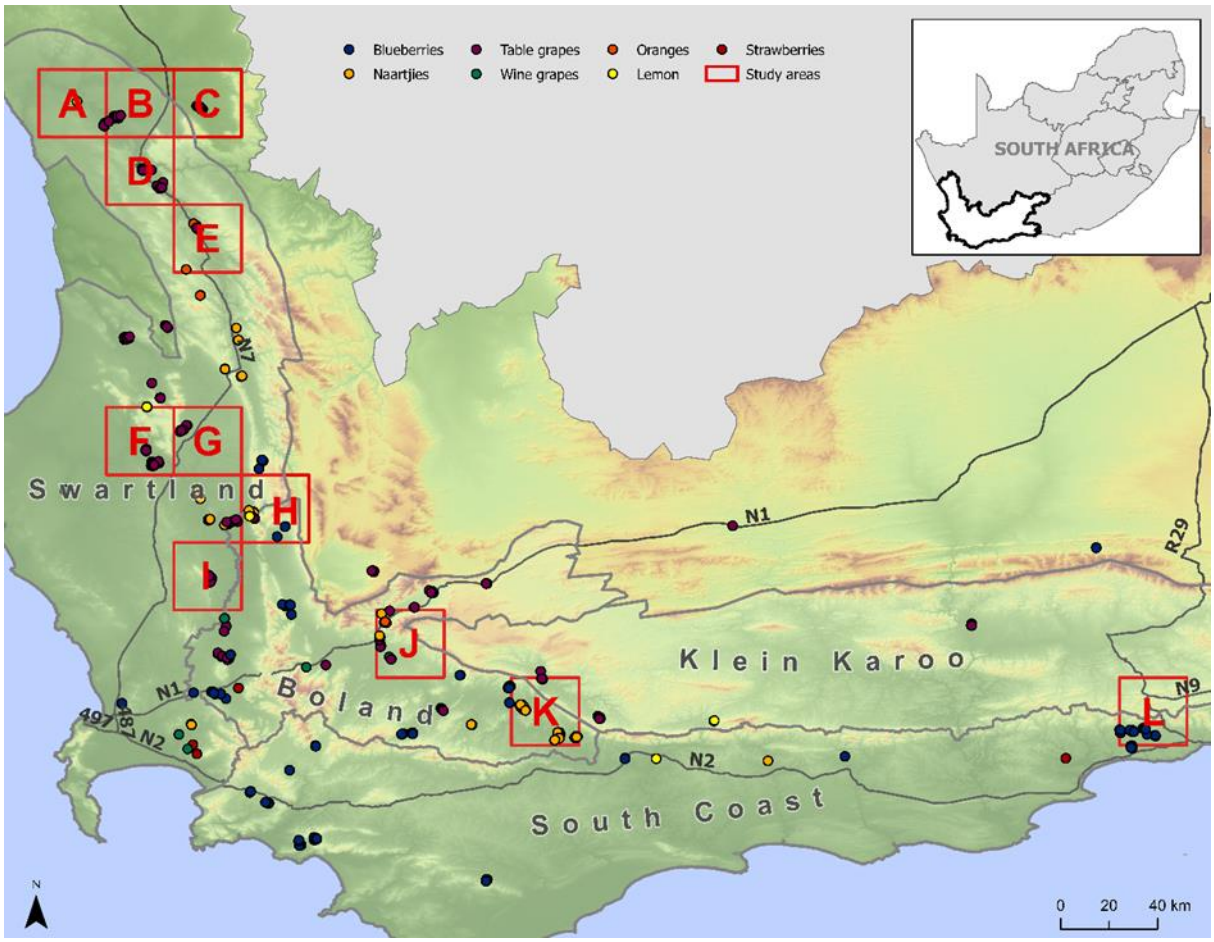


Adapted from Pienaar (2018)

Figure 3.1 Location of the selected test sites in the Western Cape and how they relate to the grape, citrus and berry varieties that are typically grown under agricultural nets in the region

Figure 3.1 shows the twelve 25x25 km test sites selected for sample collection and the location of grape, citrus and berry varieties under nets. The sites were chosen for four specific reasons, namely 1) cloud-free Sentinel-2 imagery is available for the sites for the duration of the growing season; 2) the sites contain a good representation of the diverse types of nets used in the Western Cape regarding size, density and shape; 3) the sites adequately represent the occurrence of the three targeted crop types, as well as other typical rural land cover types; and 4) spatially they cover all four climate regions of the Western Cape.

### 3.3.2 Phenology of grape, citrus and berry crops in the Western Cape

Phenology describes the key events that occur in the biological life cycles of plants or animals (Liang 2019). The phenological stages of the grape, citrus and berry crops grown in the Western Cape are shown in Figure 3.2.

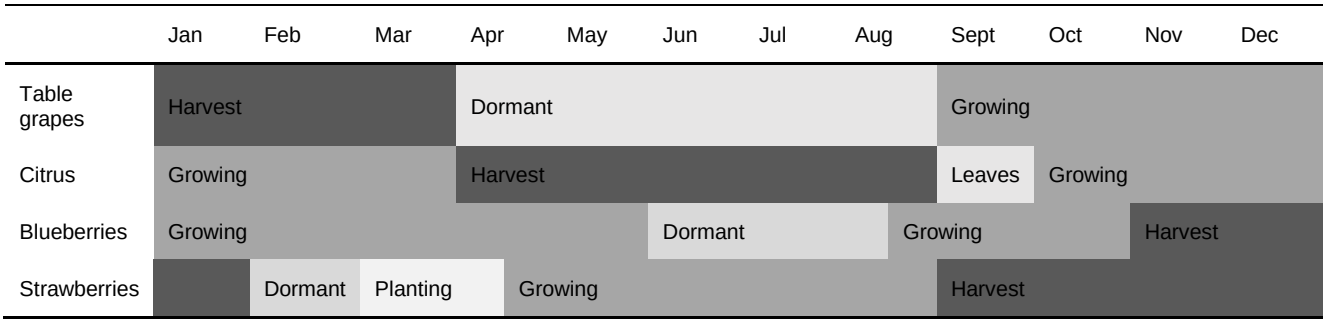


Figure 3.2 Phenological stages of grape, citrus and berry crops grown in the Western Cape

Table grapes make up 99% of grapes grown under nets in the Western Cape (Pienaar 2018). There are four major phenological stages in the production of table grapes, namely the dormant stage, the bud-break stage, the blooming stage and the ripening stage which ends with the harvest (Araujo, Abiodun & Crespo 2014). During dormancy, which occurs from April to August, the vines lose their leaves and enter a dormant state. Bud-break, typically occurring from September to October, is when the vines show the first signs of growth as new leaves start to form (Araujo, Abiodun & Crespo 2014). Blooming occurs when new flowers are formed and fruit formation begins, from November to December. The grapes then ripen and harvesting is done from January to March (Araujo, Abiodun & Crespo 2014).

The primary citrus varieties grown in the Western Cape are lemons, naartjies (tangerines) and oranges. Stander (2015) has described the three major phenological phases of citrus trees in the Western Cape. Blooming occurs from the end of September to mid-October and fruit development is from November to December. Citrus fruits reach maturity around April and the harvest season continues until August. Citrus trees maintain their leaves after the harvest (Stander 2015).

Blueberries and strawberries make up the bulk of berry crops grown under nets within the Western Cape (Pienaar 2018). Darnell et al. (1992) has identified five phenological stages of blueberries. Vegetative development occurs from December to April and flower bud initiation is from April to June. During the dormant phase (June to August) the blueberry leaves discolour and fall from the bush. The flower bloom and fruit development begin in phase four which ranges from August to October. Fruit mature and are harvested from October to December. Strawberry planting occurs from March to April and the flower bud initiation and blooming stages from April to August. Strawberries reach maturity and are harvested from October to the beginning of January (Water 2010).

### 3.3.3 Acquisition of Sentinel-2 imagery

The required Level 2A Sentinel-2 products were acquired using the Google Earth Engine (GEE) platform. GEE is a cloud-computing platform launched in 2010 to provide access to remote sensing data sets and advanced computational infrastructure (Amani et al. 2020). Level 2A products are created using the Sen2Cor package which is used to preform terrain- and atmospheric corrections, and to convert top of atmosphere (TOA) values to surface reflection.

Table 3.1 Sentinel-2 bands and their features

| Band number | Description | Wavelength interval (nm) | Spatial resolution |
|---|---|---|---|
| B1 | Coastal aerosol | 433 - 553 | 60 |
| B2 | Blue | 458 - 523 | 10 |
| B3 | Green | 543 - 578 | 10 |
| B4 | Red | 650 - 680 | 10 |
| B5 | Vegetation red edge 1 | 698 - 713 | 20 |
| B6 | Vegetation red edge 2 | 733 - 748 | 20 |
| B7 | Vegetation red edge 3 | 773 - 793 | 20 |
| B8 | Near-infrared (NIR) | 785 - 899 | 10 |
| B8A | Narrow NIR | 855 - 875 | 20 |
| B9 | Water vapour | 935 - 955 | 60 |
| B10 | Cirrus shortwave-infrared (SWIR) | 1362 - 1392 | 60 |
| B11 | SWIR 1 | 1565 - 1655 | 20 |
| B12 | SWIR 2 | 2100 - 2280 | 20 |

Adapted from Kramer (2002)

Each Sentinel-2 image contains 13 bands where bands 2, 3, 4 and 8 have a spatial resolution of 10 m; bands 5, 6, 7, 8A, 11 and 12 have a spatial resolution of 20 m; and bands 1, 9 and 10 have a

spatial resolution of 60 m. Band 10 is used exclusively for atmospheric correction and is therefore excluded from the analysis (ESA 2018). All bands were resampled to 10 m. Each band's spatial resolution, description and wavelength interval is given in Table 3.1.Vegetation signatures change rapidly within a single season (Dudley et al. 2015). To investigate the effect of phenological changes on the spectral signatures of nets, frequent and cloud-free images are required for the entire growing season of the targeted crops. Hence a total of 288 images, 24 images per test site, were collected for the period June 2019 to May 2020. Table 3.2 lists the acquisition dates of the images collected for each test site.

Table 3.2 Acquisition dates of Sentinel-2 imagery

| Study site | Acquisition dates | Study site | Acquisition dates |
|---|---|---|---|
| A | 3 Jun; 15 Jun; 3 Jul; 20 Jul; 9 Aug; 17 Aug; 1 Sept; 16 Sept; 1 Oct; 16 Oct; 2 Nov; 16 Nov; 5 Dec; 17 Dec; 1 Jan; 16 Jan; 3 Feb; 18 Feb; 1 Mar; 16 Mar; 3 Apr; 18 Apr; 5 May; 20 May; | G | 14 Jun; 25 June; 10 Jul; 15 Jul; 9 Aug; 19 Aug; 3 Sept; 23 Sept; 3 Oct; 16 Oct; 2 Nov; 17 Nov; 2 Dec; 17 Dec; 1 Jan; 16 Jan; 10 Feb; 15 Feb; 1 Mar; 16 Mar; 14 Apr; 25 Apr; 10 May; 20 May; |
| B | 3 Jun; 15 June; 3 Jul; 20 Jul; 9 Aug; 17 Aug; 1 Sept; 16 Sept; 1 Oct; 16 Oct; 2 Nov; 15 Nov; 5 Dec; 17 Dec; 1 Jan; 16 Jan; 3 Feb; 18 Feb; 1 Mar; 16 Mar; 3 Apr; 18 Apr; 5 May; 20 May; | H | 14 Jun; 25 June; 10 Jul; 15 Jul; 9 Aug; 19 Aug; 3 Sept; 23 Sept; 3 Oct; 18 Oct; 14 Nov; 22 Nov; 2 Dec; 17 Dec; 1 Jan; 16 Jan; 10 Feb; 15 Feb; 6 Mar; 16 Mar; 14 Apr; 25 Apr; 10 May; 20 May; |
| C | 3 Jun; 15 June; 3 Jul; 18 Jul; 2 Aug; 17 Aug; 1 Sept; 16 Sept; 1 Oct; 16 Oct; 2 Nov; 15 Nov; 5 Dec; 15 Dec; 1 Jan; 16 Jan; 3 Feb; 18 Feb; 1 Mar; 16 Mar; 3 Apr; 18 Apr; 5 May; 15 May; | I | 14 Jun; 25 June; 5 Jul; 15 Jul; 9 Aug; 19 Aug; 3 Sept; 23 Sept; 3 Oct; 18 Oct; 2 Nov; 17 Nov; 2 Dec; 17 Dec; 1 Jan; 16 Jan; 10 Feb; 15 Feb; 1 Mar; 16 Mar; 14 Apr; 25 Apr; 10 May; 20 May; |
| D | 8 Jun; 15 June; 3 Jul; 20 Jul; 9 Aug; 17 Aug; 1 Sept; 16 Sept; 1 Oct; 16 Oct; 2 Nov; 15 Nov; 5 Dec; 17 Dec; 1 Jan; 16 Jan; 10 Feb; 18 Feb; 1 Mar; 16 Mar; 3 Apr; 18 Apr; 5 May; 20 May; | J | 14 Jun; 25 June; 5 Jul; 15 Jul; 9 Aug; 19 Aug; 3 Sept; 23 Sept; 3 Oct; 18 Oct; 14 Nov; 22 Nov; 2 Dec; 17 Dec; 1 Jan; 16 Jan; 10 Feb; 15 Feb; 1 Mar; 16 Mar; 14 Apr; 25 Apr; 10 May; 20 May; |
| E | 3 Jun; 15 June; 3 Jul; 15 Jul; 4 Aug; 17 Aug; 1 Sept; 16 Sept; 1 Oct; 16 Oct; 2 Nov; 17 Nov; 2 Dec; 17 Dec; 1 Jan; 16 Jan; 3 Feb; 18 Feb; 1 Mar; 16 Mar; 3 Apr; 18 Apr; 3 May; 18 May; | K | 7 Jun; 15 June; 5 Jul; 15 Jul; 1 Aug; 21 Aug; 3 Sept; 23 Sept; 3 Oct; 15 Oct; 4 Nov; 19 Nov; 2 Dec; 17 Dec; 1 Jan; 16 Jan; 12 Feb; 15 Feb; 1 Mar; 21 Mar; 2 Apr; 20 Apr; 2 May; 20 May; |
| F | 8 Jun; 15 June; 10 Jul; 15 Jul; 9 Aug; 17 Aug; 3 Sept; 16 Sept; 1 Oct; 16 Oct; 2 Nov; 15 Nov; 5 Dec; 17 Dec; 1 Jan; 16 Jan; 8 Feb; 15 Feb; 1 Mar; 16 Mar; 3 Apr; 18 Apr; 8 May; 20 May; | L | 7 Jun; 27 June; 14 Jul; 22 Jul; 1 Aug; 21 Aug; 14 Sept; 25 Sept; 5 Oct; 15 Oct; 4 Nov; 19 Nov; 14 Dec; 24 Dec; 3 Jan; 28 Jan; 12 Feb; 18 Feb; 14 Mar; 28 Mar; 2 Apr; 22 Apr; 2 May; 22 May; |

Two images were collected per month for each site, the first image was captured at the start of each month (the closest image to the 1st of each month) and the second during the middle of each month (the closest image to the 15th of the month).

### 3.3.4 Acquisition of land cover samples

Sample polygons for nine land cover classes, namely *grape nets*, *citrus nets*, *berry nets*, *grape crops without nets*, *citrus crops without nets*, *berry crops without nets*, *all crops without nets*, *natural vegetation*, *bare fields*, *natural bare ground*, *water and urban*; were collected in the test sites. The samples were manually collected on-screen using very-high resolution aerial imagery as

reference data. Table 3.3 records the number of pixels sampled for each land cover class, the percentage of the total area covered by the class that was sampled, and the total percentage of the total test area covered by each class.

Table 3.3 Samples collected for each spectral class

| Class | Number of pixels | Percentage of class sampled | Percentage of study area covered by class |
|---|---|---|---|
| Grape nets | 645 079 | 100% | < 1% |
| Citrus nets | 380 145 | 100% | < 1% |
| Berry nets | 95 055 | 100% | < 1% |
| Grape crops | 647 178 | 23% | 2% |
| Citrus crops | 647 348 | 30% | < 1% |
| Berry crops | 206 544 | 100% | < 1% |
| All crops | 1 855 713 | 13% | 12% |
| Natural vegetation | 646 117 | 15% | 8% |
| Bare fields | 646 031 | 18% | 7% |
| Natural bare | 647 289 | 1% | 32% |
| Water | 646 024 | 18% | 7% |
| Urban | 384 488 | 27% | <1% |

The *citrus nets*, *berry nets*, *berry crops* and *urban* classes were under sampled, as there were limited occurrences of these classes in the sampling areas. The remaining classes have a similar number of training samples.

### 3.3.5 Spectral signatures and separability analysis

The sampled pixels were used to extract spectral values from each of the Sentinel-2 scenes. These values were used to create spectral signatures for each land cover class for the start and middle of each month. The separability between the nine classes was calculated for each acquisition period using the Jeffries-Matusita (JM) algorithm. JM distance is a statistical metric used to quantify the separability between two signatures in feature space (Dabboor et al. 2014). The metric ranges between 0 and 2, where a value of 0 indicates no separability between signatures and 2 indicates complete separability (Dabboor et al. 2014). Within the field of remote sensing, values lower than 1.7 are considered to have poor separability (Jensen 2016). The JM algorithm was implemented using the statistical computing language R (Tippmann 2015).

## 3.4 RESULTS

The outcomes of the separability analysis are summarized in the following subsections. Specifically, the net classes' separability with surrounding land cover, their average seperability per month and the spectral signatures of the three net classes and their corresponding uncovered crops will be visualized. The JM distance between the spectral signatures of each class can be found in Appendix A.

### 3.4.1 Separability analysis

Figure 3.3 shows the mean JM distance between *grape nets* and each of the other classes by season obtained by calculating the JM distance between *grape nets* and each other class for each acquisition period. The JM distances were averaged per season for each class. Similarly, Figures 3.4 and 3.5 respectively illustrate the mean JM distance of *citrus nets* and *berry nets* against the other classes per season. The standard deviation of the JM distances per each class is demonstrated by the error bars for Figures 3.3, 3.4 and 3.5.

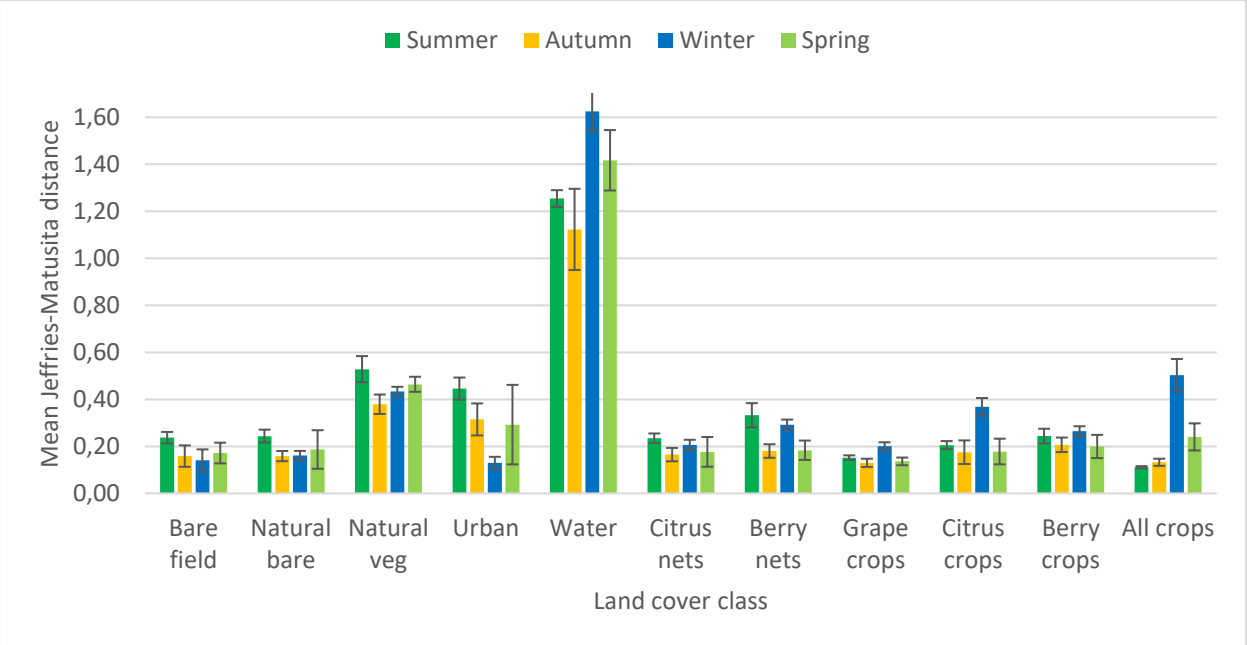


Figure 3.3 Mean Jeffries-Matusita distance between *grape nets* and each class per season

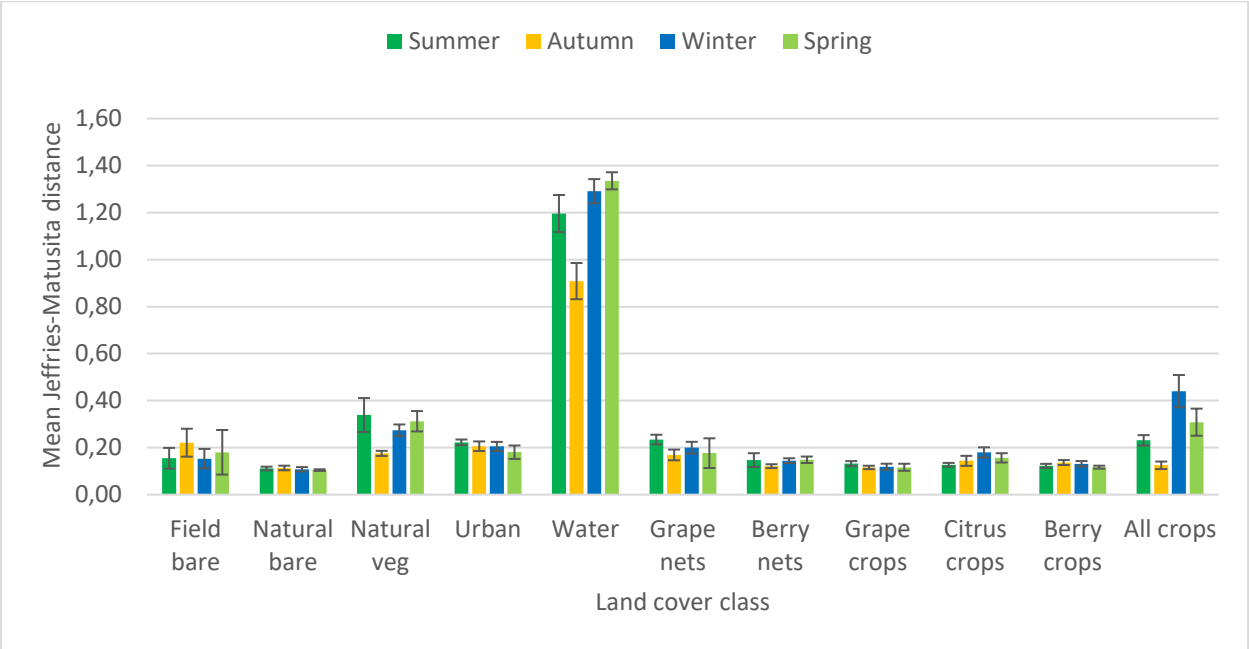


Figure 3.4 Mean Jeffries-Matusita distance between citrus nets and each class per season

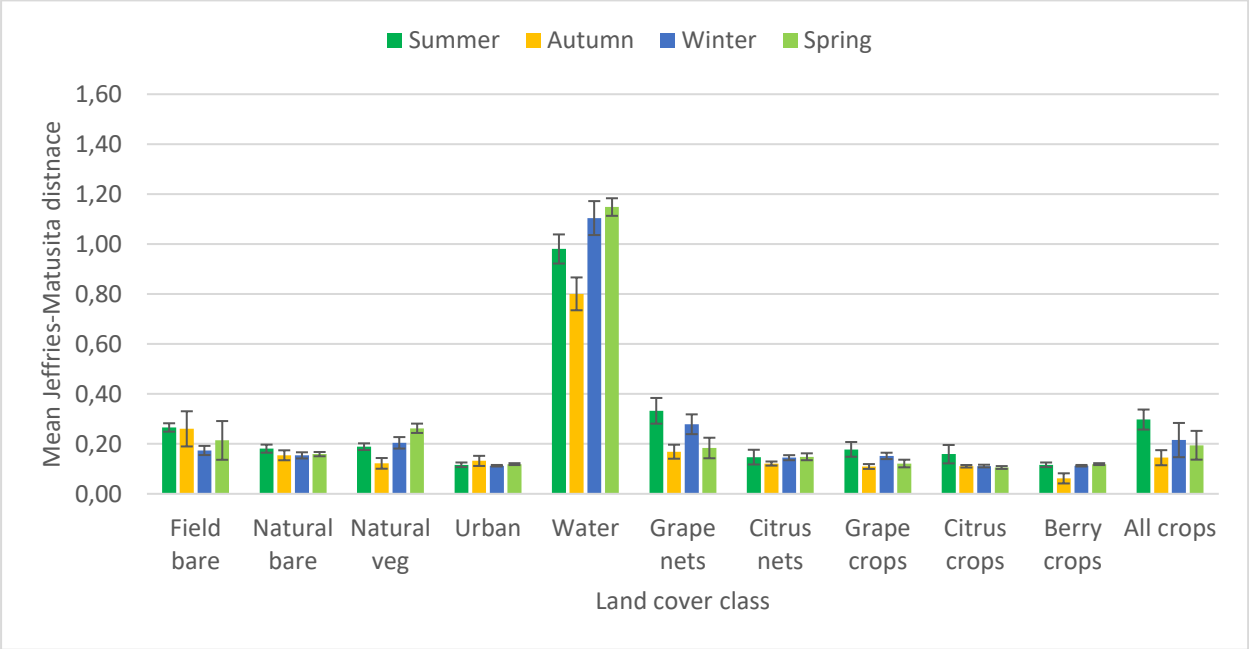


Figure 3.5 Mean Jeffries-Matusita distance between *berry nets* and each class per season

Figures 3.3, 3.4 and 3.5 all confirm that there are seasonal variations that affect the separability of the netted and the other land cover classes. Furthermore, all three net classes clearly achieve the highest separability values with the *water* class.

The *grape nets* class (Figure 3.3) shows the greatest seasonal variations in separability per class and, aside from the *water* class, *grape nets* returned JM distance values of less than 0.6 when paired against all the other land cover classes. The lowest separability values are recorded between *grape nets* and the bare ground classes (*bare field*, *natural bare*), the crop classes (*grape crops*, *citrus crops*, *berry crops*, *all crops*) and the other net classes (*citrus nets*, *berry nets*). Regarding the separability between *grape nets* and the bare ground classes, the highest separability scores are

evident in summer for both the *bare field* and *natural bare* classes. This is followed closely by the values for spring with lowest values achieved in winter and autumn. The separability between *grape nets* and the crop classes is the highest in winter. During winter, the separability values between *grape nets* and *citrus crops*, and between *grape nets* and *all crops*, are especially high compared to the other crop classes. The separability between *grape nets* and the crop classes is the second highest in summer, whereas the poorest separability values for the crop classes and *grape nets* are associated with autumn and spring. The separability between *grape nets* and *grape crops* is marginally lower than the separability of *citrus crops* and *berry crops*. The separability between *grape nets* and the other crops under nets (*citrus nets*, *berry nets*) are the highest in summer, followed closely by winter, then by spring and autumn. *Grape nets* attain a good degree of separability with *natural vegetation* and *urban* land cover compared to those for the other classes. However, *grape nets* reached its lowest separability against *urban* during winter.

It is evident in Figure 3.4 that all the classes, except *water*, have separability of less than 0.4. Similar to the separability scores of *grape nets* (Figure 3.3) the separability of *citrus nets* is lowest for the bare ground, crops and other net classes. *Citrus nets* also manifest low separability with the *urban* class. As with *grape nets*, the separability between *citrus nets* and *all crops* is the highest for winter. The separability scores between *citrus nets* and the other classes (Figure 3.4) show less seasonal variability compared to that of *grape nets* (Figure 3.3).

As with the separability values of *citrus nets*, Figure 3.5 affirms that the values of *berry nets* are less than 0.4 for all classes except *water*. The *berry nets'* separability values exhibit similar seasonal variations to those of *grape nets*. The lowest separability scores characterise the *urban* class, although the *bare field*, *natural bare*, *grape nets*, *citrus nets*, *grape crops*, *citrus crops* and *berry crops* classes all have low separability scores with the *berry nets* class. The separability between *berry nets* and *berry crops* is particularly low during autumn.

The mean JM distances of all the classes for *grape nets*, *citrus nets* and *berry nets* are graphically portrayed in Figure 3.6 for each image acquisition period. The means were calculated by averaging the JM distances of each class for each acquisition period.

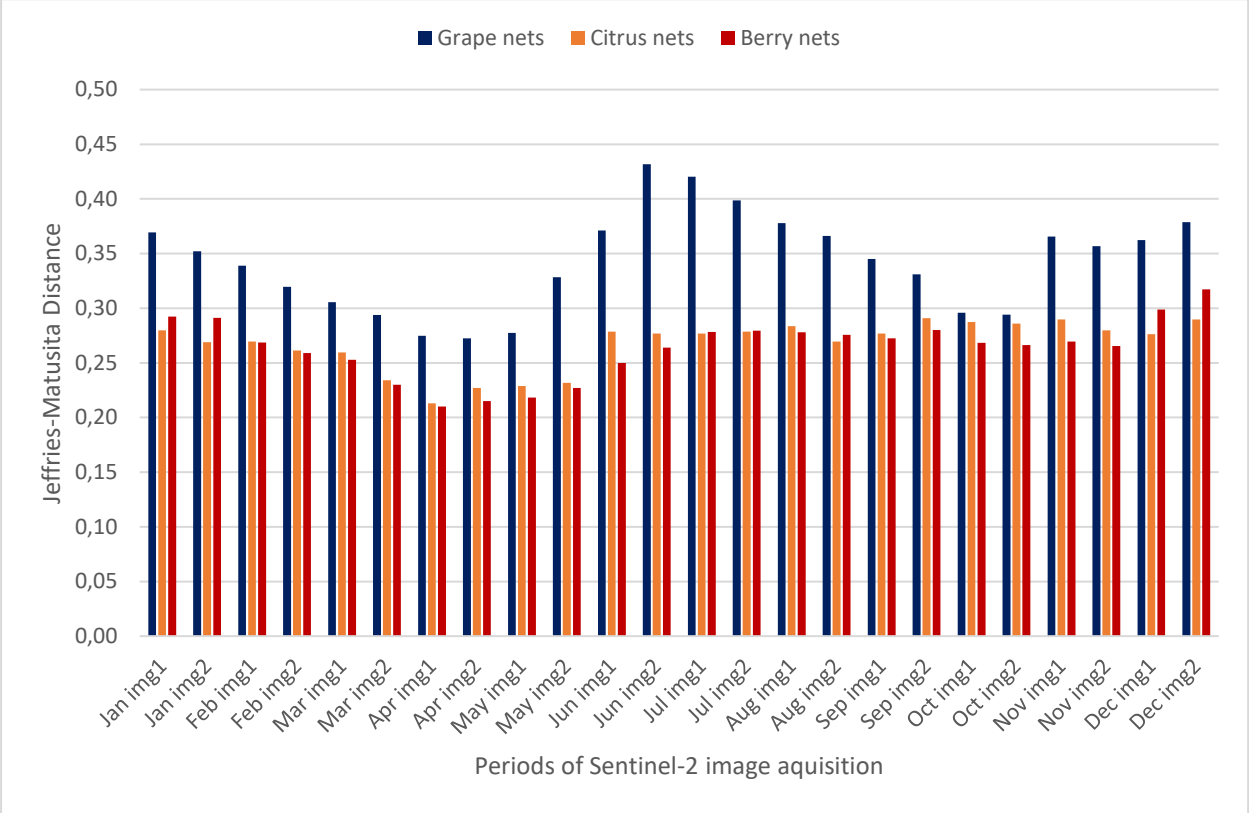


Figure 3.6 Mean Jeffries-Matusita distances of all the classes for *grapes nets*, *citrus nets* and *berry nets* for each image acquisition period

The illustration clearly shows that the *grape nets* class achieve relatively high (0.27 to 0.43) separability scores for all the acquisition periods compared to the *citrus nets* and *berry nets* classes with scores (< 0.3). The *citrus nets* and *berry nets* classes reach similar separability values throughout the year. The *grape nets* class is consistently more separable than the other two net classes.

All three classes (*grape nets*, *citrus nets* and *berry nets*) earn their highest separability scores in the summer (Dec to Feb) and winter (Jun to Aug) months, with the *grape nets* class achieving the overall highest separability value of 0.43 at the end of June. In contrast, *berry nets* and *citrus nets* achieve their highest JM distance values at the end of December. The *grape nets* class also gains high separability values during December, but not as high as during June and July. Compared to the relatively high summer and winter scores, relatively low separability scores are achieved during the spring months (Sept to Nov) with the lowest separability scores recorded during autumn (Mar to May).

### 3.4.2 Spectral signatures

Spectral signatures show the reflectance recorded by each band of a sensor for a particular land cover. These signatures can be used to compare the spectral response of different land cover to inform feature selection for classification (Mutanga, Adam & Cho 2012).

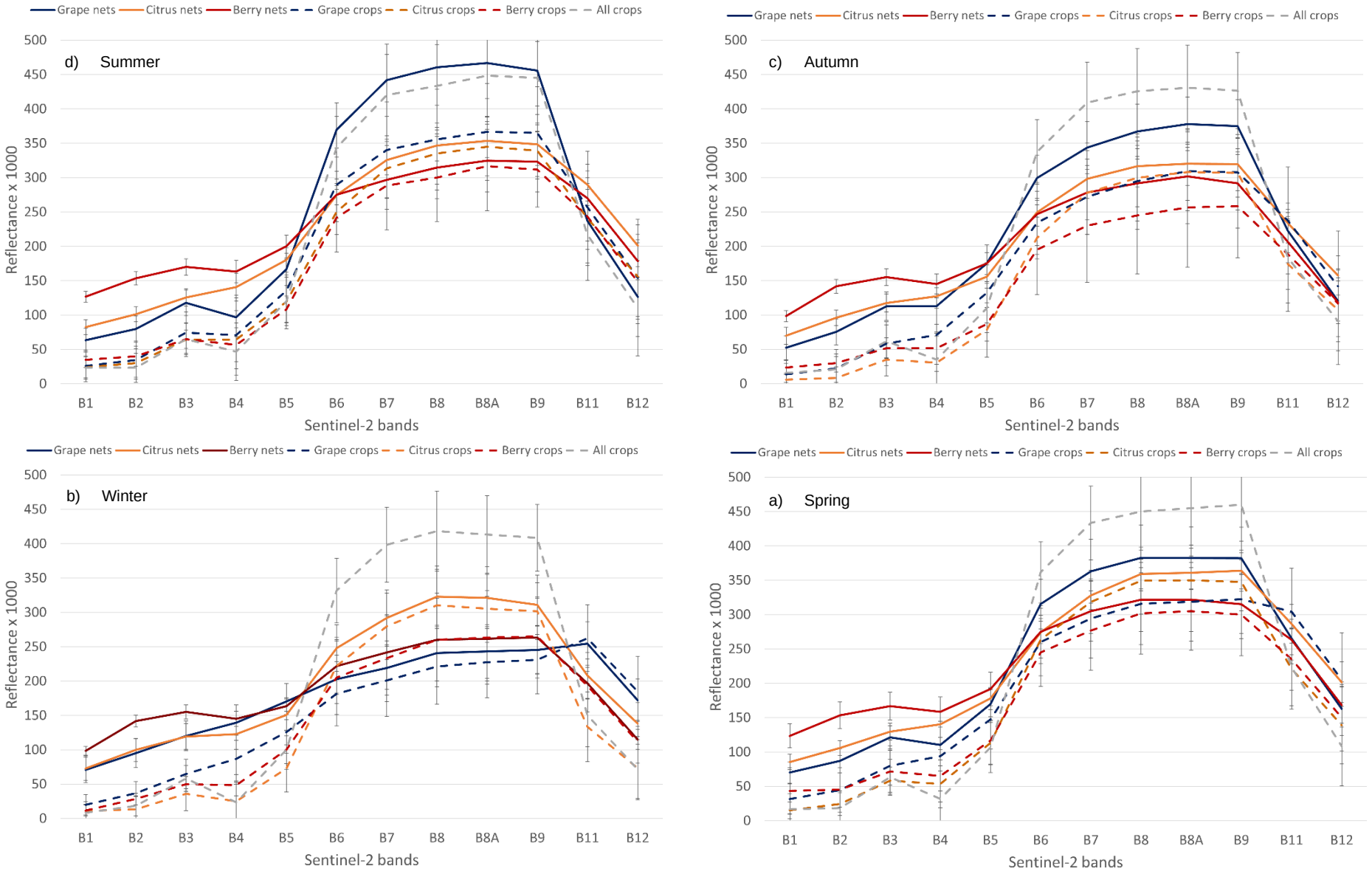


Figure 3.7 Mean spectral signatures of the *grape nets*, *citrus nets*, *berry nets*, *grape crops*, *citrus crops*, *berry crops*, and *all crops* classes for a) Summer, b) Autumn, c) Winter and d) Spring where the error bars represent the standard deviation of the signatures

Figures 3.7a to d compare the seasonal mean spectral signatures of *grape nets*, *citrus nets* and *berry nets* to *grape crops*, *citrus crops*, *berry crops* and *all crops*. It is evident in Figure 3.7 that higher reflectance values were consistently recorded in bands 1 (coastal aerosol), 2 (blue), 3 (green), and 4 (red) for net-covered crops, compared to uncovered crops. However, the shapes of the covered crop signatures mimic the shape and seasonal changes of their uncovered counterparts. The standard deviation of the spectral signatures for all seven classes are high throughout the year, particularly for the NIR (8 and 8A) and SWIR (11 and 12) bands.

The signature shapes of the seven classes change according to season. From summer to winter the *grape nets* and *grape crops* signatures decrease in reflectance for bands 6 to 9 which correspond to the red edge (RE) and near infrared (NIR) regions of the electromagnetic spectrum (EMS). Furthermore, during this period, both these classes increase in reflectance for bands 11 and 12 which correspond to the SWIR region of the EMS. The reflectance in the RE and NIR regions then increases during spring in contrast to decreasing reflectance in the SWIR region.

The spectral signature of the *citrus nets* shows less variation over the seasons than the case of *grape nets* but there is a decrease in reflectance in the RE and NIR regions for both *citrus nets* and *citrus crops* during autumn. Furthermore, the reflectance of *citrus nets* is higher than the reflectance of *citrus crops* in all the Sentinel-2 bands. The difference between these two signatures is larger in the visible (bands 1, 2 and 3) and SWIR (bands 11 and 12) regions than in the RE and NIR regions (bands 5, 6, 7, 8 and 8A).

For bands 2, 3 and 4 (visible region), the reflectance of *berry nets* is higher than all the other classes over the course of the entire year. However, during the winter months the *berry nets* and *berry crops* signatures decrease in reflectance in the RE and NIR regions. In winter, these two signatures are nearly identical in the RE, NIR and SWIR regions of the EMS.

## 3.5 DISCUSSION

According to Jensen (2016), classes that have JM scores lower than 1.7 are considered to have poor separability. The foregoing analysis of separability established that all three net classes achieved separability values lower than 0.6 for all the classes except water (Figures 3.3, 3.4 and 3.5). These findings make it clear that the agricultural nets exhibit a poor degree of separability from most of the surrounding land covers in the study sites. Nets vary greatly in their thickness, density, transparency, light dispersal as well as their ultraviolet and infrared absorption properties (Levin et al. 2010). Consequently, the spectral variance in each net class is high and this decreases their separability from other land cover classes (Du & Sun 2008). This low separability is

attributable to the large variations in the net signatures. This is substantiated by the large standard deviations recorded for the *grape nets*, *citrus nets* and *berry nets* spectral responses (Figure 3.7).

The separability of all three net classes is particularly low for the *urban*, *bare field*, *natural bare*, *grape nets*, *citrus nets*, *grape crops*, *citrus crops* and *berry crops* classes (Figures 3.3, 3.4 and 3.5). These results agree with findings in other studies where a high degree of confusion is noted between the net and urban (Aguilar et al. 2015; Aguilar et al. 2016; Levin et al. 2010; Yang et al. 2017), crop (Lanorte et al. 2017; Tarantino et al. 2012; Yang et al. 2017), bare soil (Lanorte et al. 2017; Yang et al. 2017), natural vegetation (Lanorte et al. 2017; Tarantino et al. 2012), and other plastic covering classes (Aguilar et al. 2014; Aguilar et al. 2015; Levin et al. 2010).

Levin et al. (2010) attribute the poor separability of nets and built-up structures to vertical mixing, i.e. when the net signature and the signature of the crops under the net combine to form a single mixed pixel value. This type of mixing is most prevalent when high-to medium-resolution imagery is used to capture agricultural nets. These mixed signatures resemble the signatures of urban land cover which comprise artificial structures and surrounding vegetation (Levin et al. 2010). This explains why the separability between agricultural nets and urban land cover is low. Aguilar et al. (2016) found that the confusion between white buildings and thicker plastic coverings, such as films and nets with low porosity, was particularly high. In the Western Cape berry crops are primarily covered to protect the plants from hail and extreme weather conditions whereas citrus and grape crops are primarily covered to provide shading and protection from birds (Ngubane 2018; Tarantino et al. 2012). Such so-called hail nets are made from thicker, more durable plastic with a lower porosity than the shade and pest nets (Castellano et al. 2008). This likely explains the lower separability registered for the *berry nets* versus the *urban* class, as the thicker and denser nets resemble built-up features (i.e. high reflectance in the visible bands).

Tarantino et al. (2012) used aerial imagery to compare the spectral signatures of uncovered vineyards to those of vineyards grown under nets. The analysis of the three bands, namely red, green and blue (RGB), revealed that the reflection of the covered vineyards was higher than that of the uncovered vineyards for all three bands. Similarly, the results presented in Figure 3.7 show that covered vineyards have higher reflectance values in the RGB bands (bands 2, 3 and 4) compared to those of uncovered vineyards. The results in Figure 3.7 expand on that of Tarantino et al. (2012) by revealing that netted citrus and berries also have higher reflectance values than uncovered citrus and berries, and that this phenomenon occurs consistently throughout the year. This is attributable to white objects usually having very high reflectance values in the visible region of the EMS (Lillesand, Kiefer & Chipman 1994) and to the fact that most nets in the Western Cape are white (Pienaar 2018). This finding bodes well for finding an operational solution to classifying

agricultural nets in the province. Levin et al. (2010) have compared the spectral signature of shade nets captured by a hyperspectral sensor to the signature extracted from a Landsat-7 image and found that the hyperspectral sensor detected three major absorption features at 1218, 1732 and 2313 nm. However, the spectral and spatial resolutions of Landsat-7 imagery were too low to detect these features (Levin et al. 2010). Likewise Figure 3.7 shows that Sentinel-2 imagery is unable to detect these unique absorption features, but it does illustrate that the spectral signatures of covered and uncovered crops of the same type are similar in shape. This signifies that Sentinel-2 imagery can capture a reliable signal of the crops under nets. This finding corroborates those of Borgogno-Mondino, Palma & Novello (2020) who compared the spectral signatures of uncovered and covered vineyards captured by Sentinel-2 and found that the imagery was able to capture the unique spectral properties of the vineyards under the nets. This finding suggests that Sentinel-2 imagery could potentially be used to map crops under nets.

However, the spectral signatures of crops can change dramatically over time as crops enter different phenological stages (Levin et al. 2010). This, in turn, can cause the spectral signatures of agricultural nets to change according to the phenological stages of the crops they cover (Levin et al. 2010). The foregoing analysis proves that the signatures of the crops and the signatures of the nets change throughout the seasons (Figure 3.7) to the extent that changes in reflectance of each covered crop mimic the changed reflectance of the corresponding uncovered crops. This suggests that the seasonal changes in the signature of the nets is caused by the underlying crops and that the Sentinel-2 imagery can capture the signature of the crops under the nets, although the effect of the nets is non-linear (not constant for all wavelengths). The separability of the agricultural nets from surrounding land cover also changes throughout the year (Figures 3.3, 3.4, 3.5 and 3.6). This seasonal variation is likely caused by the changing spectral signatures of the nets, as well as the crops grown in the test sites.

Yang et al. (2017) found that seasonal changes particularly affect the separability of nets from vegetation and bare classes. This effect is noticeable in Figure 3.3 which shows that *grape nets* demonstrate higher seasonal variation in separability compared to *citrus nets* and *berry nets*, especially when juxtaposed with the uncovered crops and *natural bare* classes. The visible appearance of vineyards changes dramatically throughout the year as the vineyards mature in summer, the vine foliage changes colour (from green to yellows and reds) in autumn and the leaves are shed in winter. *Grape nets* therefore have lower separability from other crop types during summer (Figure 3.3) because the signature of the mature vineyards resembles that of the crops in the test sites (Figure 3.7a). Tarantino et al. (2012) and Lanorte et al. (2017) all reported large errors of commission and omission between mature vineyards under nets and surrounding crops. The

separability of *grape nets* and other crops – particularly evergreen crops such as citrus – improve during winter as the vineyards colour and the vines enter dormancy (Figure 3.3). This is supported by the change in the spectral signature shape of *grape nets* during winter (Figure 3.7) which is noticeably different (flatter in the near-infrared region of the EMS) to the shape of the other classes of crops. However, as the leaves are shed, a larger proportion of the background soil signal influences the spectral signature of the vines, which decreases the separability of *grape nets* from the *bare ground*, *grape crops* and *natural bare* classes.

During autumn, vineyards start to discolour in preparation to leaf shedding, but this discolouration occurs at different rates within vineyards as well as among vineyards depending on the cultivars planted (Araujo, Abiodun & Crespo 2014). The effect is that the intra-class variation of vineyards is high during autumn. This may explain why the separability scores achieved by *grape nets* is lower in autumn than during the other seasons (Figures 3.3 and 3.6). Similarly, the intra-class variation of *grape nets* is higher in spring when vineyards flower at different rates depending on their cultivar and on chilling during winter (Araujo, Abiodun & Crespo 2014). The separability scores of *grape nets* are consequently lower in spring than in winter and summer. However, differences in bud-break rates do not seem to influence the separability as severely as the discolouration of the vineyards during autumn (compare Figures 3.3 and 3.6).

*Citrus nets* and *berry nets* both achieve lower mean separability scores than *grape nets* for each acquisition date (Figure 3.6) and show less seasonal variation in their spectral signatures and separability scores. *Citrus nets* and *berry nets* both represent multiple varieties. Specifically, *citrus nets* include the varieties oranges, tangerines, and lemons under nets and the *berry nets* class include the varieties blueberries and strawberries. The subtle differences among fruit varieties within classes increases intra-class variation that leads to the lower separability values for these classes (Figures 3.4, 3.5 and 3.6). In the case of *citrus nets*, the different citrus varieties have similar phenological stages and maintain their leaves throughout the year. Therefore, the spectral signature of *citrus nets* does not change as dramatically as for *grape nets* in Figure 3.7. In the case of *berry nets*, strawberries and blueberries have different phenological stages (Figure 3.2). By combining these berry varieties, the unique changes caused by the phenological changes of each variety are not captured by the averaged *berry nets* signature in Figure 3.7. Hence, the spectral profiles of the *berry nets* and *berry crops* classes show little seasonal variation. This is most likely why the separability scores of *berry nets* show less seasonal variation compared to those of *grape nets*. However, *berry nets* achieve lower separability scores in autumn (Figure 3.6) when the leaves of blueberry bushes – which make up the majority of the *berry nets* class – change colour, so causing an increase in intra-class variation. Another factor contributing to the low separability

scores recorded in the autumn for all three net classes is the discolouration in the leaves of other vegetation and crops within the test sites. This is corroborated by the decrease in separability during autumn for the *all crops* and *natural vegetation* classes (Figures 3.3, 3.4 and 3.5).

The analyses provide useful insight into the periods during the year that maximize the separability of the net classes from surrounding land cover (Figure 3.6). The highest separability scores for both *citrus nets* and *berry nets* are achieved toward the end of December. The *grape nets* class also achieve high separability scores in this period. These results point to the summer as the most appropriate time to map crops under nets in the Western Cape. During summer most of the crops under nets have already matured and their unique spectral properties have developed, making the different crop types under nets easier to differentiate (Aguilar et al. 2015). Aguilar et al. (2015) mapped crops under nets in southern Spain using multiple images throughout the crop-growing season and found that relatively high overall accuracy (67%) was achieved for the image captured in September towards the end of the growing season. They attributed this to the crops having reached maturity which resulted in a brighter and unique signature for each netted crop type studied (Aguilar et al. 2015). In the current study, *grape nets* achieve the highest separability values at the end of June so suggesting that this period will yield better results for mapping vineyards under nets.

The clear differences between the signatures of the different crop types under nets (Figure 3.7) forebode that any combining of the different nets into a single class will result in high levels of confusion in land cover classification when using Sentinel-2 imagery. The results of this study indicate that this problem can be addressed by separating the different crop types grown under nets into separate classes and then mapping these nets during summer, but more research is needed to test this possibility. Moreover, other methods such as spectral indices and texture features should be investigated to find ways to improve seperability. This present study has been constrained by limited availability of training data for the net classes. Future studies would benefit from separating the berries and citrus classes into their constituent varieties.

## 3.6 CONCLUSION

This chapter has reported on an investigation of the spectral signatures of different agricultural nets captured by Sentinel-2 imagery. The study sought to gain insight into how the presence of agricultural nets affects the signatures of crops under nets, with the primary aim was to evaluate the spatial and spectral capabilities of Sentinel-2 for mapping agricultural nets and the crops they cover. The secondary aim was to examine the effect of temporal variability on the separability of net signatures to determine which time of the year is best for mapping the different types of nets and the crops they typically cover. The mean spectral separability of *grape nets*, *citrus nets* and

*berry nets* classes were compared for the period June 2019 to May 2020 that corresponds to the fruit-growing season in the Western Cape.

The results give new insight into the spectral properties of agricultural nets, which is essential for developing mapping and monitoring solutions. The presence of nets was found not to dramatically change the characteristics (shape) of the spectral profiles of the crops they cover. For the most part, the spectral profiles of the netted crop classes mimic those of their respective uncovered counterparts. The reflectance of the netted classes tend to be higher, particularly in the visible spectrum of the EMS. The Sentinel-2 imagery is also able to capture the unique properties of the different nets as the signatures change due to seasonal variations of the crops under nets. This holds promise for Sentinel-2 imagery being used to differentiate crop types covered by nets.

The separability values of the net classes were generally low and the presence of nets increased the confusion between crops under nets with bare soil and urban land cover. It was also established that the seasonal variations of the crops under nets significantly affect the separability of agricultural nets from surrounding land cover. Notably, summer is the best time to differentiate between targeted crop types grown under nets, although winter is the most appropriate time for mapping covered vineyards.

The findings reported in this chapter represent the first attempt to understand the spectral dynamics of agricultural nets in a South African context and specifically in the context of using Sentinel-2 imagery. The findings also lay a solid foundation for developing a solution for mapping and monitoring crops grown under nets at regional scales. Such a solution is essential for expanding the capacity of existing remote sensing techniques used for agricultural monitoring to include crops grown under nets.

# CHAPTER 4: REGIONAL MAPPING OF TABLE GRAPES UNDER AGRICULTURAL NETS USING SENTINEL-2 IMAGERY[1]

## 4.1 ABSTRACT

The table grape industry is an integral part of South Africa's economy, contributing some R3 billion toward the gross domestic product. Over the last decade, this industry has been put under increasing strain due to climatic variations and extreme weather events. Many table grape farms are utilizing agricultural nets as an adaptation strategy to mitigate the potential impact of such variations on table grape production. However, agricultural nets have adverse environmental effects such as increased plastic waste pollution and the disruption of the water infiltration-run-off balance. Little is known about the extent of these impacts, mainly because no record of the netted areas exists. The mapping and monitoring of agricultural nets will provide a better understanding of their potential environmental impact at regional scales. Remote sensing has become a reliable tool for mapping and monitoring land cover over large areas, but the variable spectral properties and semi-transparent nature of nets pose a unique challenge to remote sensing applications. This study investigated the potential of Sentinel-2 imagery for mapping agricultural nets at regional (provincial) scale. Eight study sites which contain a variety of agricultural nets in terms of size, shape and density, were selected in the Western Cape province. Several configurations of image features, including spectral bands, spectral indices and grey-level co-occurrence matrix (GLCM) texture features, were used as input to random forest (RF), support vector machine (SVM) and neural network (NN) machine learning classifiers. The results show that NN preformed best with an overall accuracy of 97% and a kappa statistic of 0.87. RF and NN both proved to be effective classifiers for mapping agricultural nets with both achieving high average accuracies for the different feature sets. The Sentinel-2 bands contained the most important information for classification. The results of this study present Sentinel-2 imagery as a practical and viable source of data for mapping agricultural nets.

## 4.2 INTRODUCTION

South Africa accounts for 22% of the southern hemisphere's table grape exports, estimated at 63.5 million cartons per year (SATI 2020). In 2020 this industry employed 78 670 farm workers (SATI 2020) and contributed some R3 billion to the gross domestic product (Mtshiselwa 2020). However, the industry is under threat from climate change as table grapes are particularly sensitive to high temperatures, prolonged heat waves and reduced rainfall (GreenAgri 2016).

[1] This chapter is formatted as a standalone, publication-ready article. Some duplication with Chapters 2 and 3 should consequently be expected.

Agricultural nets are used to protect crops against sunburn, dehydration, hail, wind, snow, rain and pests (Briassoulis, Mistriotis & Eleftherakis 2007). These nets provide a versatile and cost-effective solution to adapt to the increased weather variability, unreliable rainfall and increased frequency of extreme weather conditions associated with climate change (Jones, Singels & Ruane 2015). The estimated global coverage of plastic nets was 86 000 ha in 1999; had tripled by 2002 and is predicted to increase exponentially as time progresses (Takakura & Fang 2002). In South Africa it has been estimated that 2323 ha of agricultural land had been covered by agricultural nets by 2017, the most notable increase occurring over citrus and table grape cultivars (Pienaar 2018).

The growing utilization of agricultural nets has three noteworthy implications. First, agricultural nets have become an important tool for increasing the quality and quantity of agricultural produce (Levin et al. 2010). As such, the area of plastic-covered agricultural is considered to be an indicator of agricultural intensification (Lim 2002). Second, these nets generate a large amount of plastic waste (Levin et al. 2010). In South Africa, the agricultural sector is responsible for 9% of the country's plastic consumption, of which 15% can be repurposed (PlasticsSA 2018). Third, agricultural nets have a major impact on the rate of evapotranspiration and water stress in crops, as well as the water infiltration-run-off balance of cultivated land (Levin et al. 2010). For these reasons, the monitoring and mapping of agricultural nets are essential for gauging the environmental and hydrological impacts of agricultural practices (Aguilar et al. 2014).

Remote sensing has become indispensable to agricultural applications. Frequent and accurate imagery over large areas facilitate the mapping and monitoring of crop extent, weed infestations, pest damage, plant health, nutrient needs, water use and water stress (Wójtowicz, Wójtowicz & Piekarczyk 2016). This information ensures the effective management of agricultural resources and agricultural waste (Wójtowicz, Wójtowicz & Piekarczyk 2016). However, the introduction of plastic netting prevents the application of standard remote sensing approaches for monitoring crop characteristics (Van Niekerk et al. 2018). New remote sensing methods are needed for monitoring crops under nets, but the application of such methods is dependent on knowing which crops are covered by nets. Due to their diverse applications, agricultural nets differ greatly regarding their physical properties (e.g. material, colour, density) and therefore present a unique challenge to remote sensing practices (Levin et al. 2010).

A number of studies have been devoted to mapping plasticulture using remote sensing (Aguilar et al. 2014; Aguilar et al. 2015; Aguilar et al. 2016; Carvajal et al. 2006; Tarantino et al. 2012). Invariably, very-high-resolution satellite imagery acquired by WorldView-2 (Aguilar et al. 2016), WorldView-3 (Aguilar et al. 2018), GeoEye-1 (Aguilar et al. 2014) and aerial imagery (Tarantino et al. 2012) have been employed for this purpose. Although these methods have proved to be

successful, very-high-resolution products are expensive and difficult to acquire, and therefore present an obstacle to mapping large areas (Boyle et al. 2014).

The medium- and high-resolution satellites, such as Landsat and Sentinel-2, are widely used for land cover mapping as they provide cost-effective imagery with global coverage (Thanh Noi et al. 2017). Novelli & Tarantino (2015) have implemented a rule-based classification of agricultural nets using Landsat-8 OLI and TIRS imagery. Their classification scheme used the normal difference vegetation index (NDVI), the plastic surface index (PSI) and the normalized difference sandy index (NDSI) to achieve an overall accuracy of over 80% for each study area. Lanorte et al. (2017) used Landsat-8 imagery in a per-pixel classification of plastic-covered (nets and films) vegetation. An overall accuracy of 95% was achieved by the support vector machine (SVM) classifier (Lanorte et al. 2017). Levin et al. (2010) simulated various spatial resolutions to map greenhouses in Israel and found that the optimal spatial resolution for mapping these greenhouses was 16 m or finer resolution. Therefore, Sentinel-2 imagery with a spatial resolution of 10 m, may be more appropriate for mapping plasticulture than with Landsat-8 imagery which has a spatial resolution of 30 m.

Sentinel-2 was launched in 2014 with the goal of providing high-resolution satellite imagery for land cover monitoring and other applications (Phiri et al. 2020). The products acquired by Sentinel-2 are freely available and therefore have the potential to contribute toward sustainable, global land cover mapping and monitoring initiatives (Phiri et al. 2020). Although Sentinel-2 imagery has not been used to map agricultural nets, Novelli et al. (2016) have compared Landsat-8 and Sentinel-2 imagery for object-based classification of plastic greenhouses. Sentinel-2 imagery outperformed Landsat-8 imagery by achieving an overall accuracy of 92% when using the random forest (RF) classification algorithm (Novelli et al. 2016). The RF algorithm is one of many machine learning (ML) algorithms like SVM and neural network (NN) that have been effectively applied to mapping applications (Maxwell, Warner & Fang 2018). ML methods have the unique ability to model complex class signatures so making these algorithms ideal for complex mapping problems, such as agricultural nets (Maxwell, Warner & Fang 2018). RF and SVM have been repeatedly utilized to map plasticulture (González-Yebra et al. 2018; Hasituya et al. 2017; Lu, Tao & Di 2018; Novelli et al. 2016). RF is an ensemble algorithm that uses a set of decision trees to classify data (Belgiu & Drăguţ 2016). SVM classifies data by isolating classes in feature space using a kernel function (Maxwell, Warner & Fang 2018). Although both classifiers can be used to map agricultural nets, Hasituya & Chen (2017) found that RF significantly outperforms SVM for mapping plastic-mulched land cover (PML). NN is not popular for mapping plasticulture with medium- and high-resolution imagery, but it has shown promise when used for mapping plastic greenhouses with

very-high-resolution imagery as input (Aguilar et al. 2014). Despite their effectiveness for remote sensing applications, ML algorithms have limitations when applied to high-dimensional and highly correlated data sets (Darst, Malecki & Engelman 2018). Georganos et al. (2018) have demonstrated that feature selection methods mitigate the effect of high dimensionality and significantly improve the accuracy and performance of ML classifiers.

A mapping solution that can accommodate table grapes planted under agricultural nets is urgently required to effectively map and monitor table grapes in South Africa. According to Aplin (2004) a successful land cover mapping solution requires the target feature to be spectrally separable from surrounding features; the remote sensor to have adequate resolutions to discriminate the target signature from the surrounding land cover; and an appropriate classification methodology. Sentinel-2 imagery has the potential to meet these requirements and to provide a practical solution for mapping agricultural nets and the crops they cover. The primary aim of this study is to evaluate the potential of Sentinel-2 imagery to identify and map nets covering table grapes. The secondary aim is to identify the spectral features and classification algorithms that are best suited for this application.

## 4.3 METHODS

The following subsections outline the procedures followed to achieve the above-mentioned aims. Specifically, these subsections address the selection of study sites for the experiment, the data acquisition and preprocessing, and the methods used for classification and accuracy assessment.

### 4.3.1 Study region and sites

The Western Cape province, located on the south-western coast of South Africa, was chosen as the study region (Figure 4.1). The province is the fourth largest in South Africa with an area of 129 449 $km^2$ and it is topographically and climatically diverse (Griffiths et al. 2010). The western part of the province borders the Atlantic Ocean and is characterised by a semi-arid microclimate due to the cold Benguela current. The eastern region borders the Indian Ocean, with its warm Agulhas current (Griffiths et al. 2010). Consequently, the eastern parts have a maritime climate with cool, moist winters and mild, moist summers (Griffiths et al. 2010). The interior of the province has a Mediterranean climate with hot, dry summers and cold, wet winters (Cowling et al. 1996). The eastern region is dominated by a range of folded sandstone mountains known as the Cape Fold Belt (Compton 2016). The valleys between these mountains provide fertile soils for a range of agricultural activities, including vineyards (table and wine grapes), fruit orchards and rooibos tea plantations (Compton 2016).

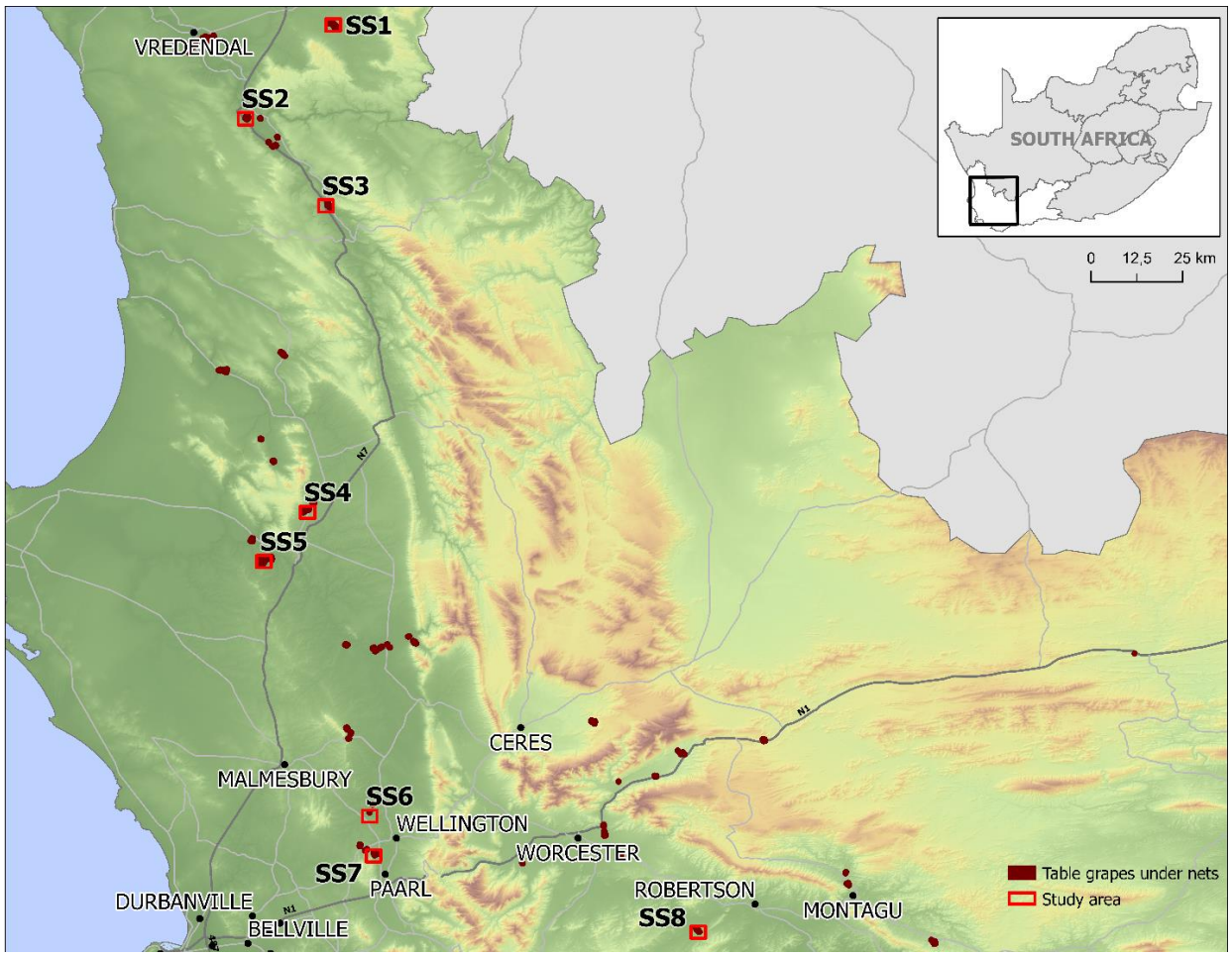


Adapted from Pienaar (2018)

Figure 4.1 Study sites in the Western Cape and the location of known table grape cultivation under agricultural nets

Three of the five primary South African table grape regions, namely the Olifants River region, the Berg River region and the Hex River region, are located in the Western Cape (SATI 2020). In the Western Cape table grapes vines are planted towards the end of winter and the grapes are harvested in mid- to end of summer depending on the specific cultivar (VinPro 2021). The Western Cape experienced a severe drought from 2015 to 2019 that caused a decline in agricultural productivity (Zwane 2019). Consequently, there has been a significant increase in the use of agricultural nets in the region (Pienaar 2018). In the Western Cape table grapes make up 36% of the crops grown under nets, while berry (19%) and citrus (15%) crops are often covered too (WCDoA 2018).

Selection of the study sites was based on four factors. First, the availability of the Western Cape Department of Agriculture (WCDoA) crop census (WCDoA 2018), a.k.a. the ‘Elsenburg fly-over data set’, comprising the digitized boundaries of agricultural fields and nets in the Western Cape. The digitizing of field and net boundaries are time-consuming and expensive processes that are infrequently carried out, especially at provincial scale. The preceding census of agricultural nets was conducted more than a decade ago (Pienaar 2018). Therefore, the Elsenburg fly-over data set, which is unique to the Western Cape, is an asset to this study. Second, cloud-free Sentinel-2

imagery is available for the study sites. Third, the sites represent the most common types of plastic nets found in the Western Cape in terms of their size, shape and plastic material used. Fourth, the sites were chosen to study the transferability of the method as they represent the different land use patterns and topography that characterise the Western Cape.

### 4.3.2 Data acquisition and preparation

#### 4.3.2.1 Sentinel-2 imagery

Sentinel-2 images with Level 2A processing were acquired using Google Earth Engine (GEE). Level 2A products have been geometrically corrected and contain 12 bands representing rescaled surface reflectance values (SIC 2016). The 12 bands comprise bands 1 and 9 that have a resolution of 60 m; bands 2, 3, 4 and 8 that have a resolution of 10 m; and bands 5, 6, 7, 8A, 11 and 12 that have a spatial resolution of 20 m. The Sentinel-2 sensor has an additional cirrus band (band 10) that is exclusively used for atmospheric correction and is therefore excluded from the Level 2A product (ESA 2018).

Table 4.1 Acquisition dates of Sentinel-2 images for the study sites

| Study site | Sentinel-2 image acquisition date |
|---|---|
| SS1 | 10 June 2020 |
| SS2 | 10 June 2020 |
| SS3 | 10 June 2020 |
| SS4 | 10 June 2020 |
| SS5 | 10 June 2020 |
| SS6 | 15 June 2020 |
| SS7 | 15 June 2020 |
| SS8 | 15 June 2020 |

All the bands were resampled to a spatial resolution of 10 m before being exported from GEE. All the images are cloud-free and captured between 10 and 15 June 2020 (Table 4.1). June corresponds with the pruning stage of the table grape production cycle and therefore represents a period when vines are dormant and bare (VinPro 2021).

#### 4.3.2.2 Training and reference data

In order to test the accuracy and transferability of the classification method, the test sites were divided into training and reference groups. SS1, SS2, SS4 and SS7 were chosen for model building (training) and sites SS3, SS5, SS6 and SS8 were used as reference. The training and the reference groups contain table grapes planted under a variety of net types and shapes, as well as a mixture

of surrounding land cover types that will facilitate the evaluation of the accuracy and transferability of the classification.

Digitised polygons of agricultural nets (sourced from the Elsenburg fly-over data set) was used to manually identify initial samples. A combination of Sentinel-2 imagery and very-high-resolution aerial imagery was then used to confirm these samples and identify additional ground truth for the eight sites. Five land cover classes were chosen for the classification, namely table grapes under agricultural nets (*grape nets*); non-netted (open), bare agricultural fields (*bare field*); rocky and sandy natural land cover (*bare natural*); non-netted (open) agricultural fields with crops (including but not limited to table grapes) present (*crops*); and natural vegetation (*natural vegetation).* The number of pixels collected for each class are summarized in Table 4.2.

Table 4.2 Number of pixels collected for each training class

| Class name | Grape nets | Bare field | Bare natural | Crops | Natural vegetation | Total |
|---|---|---|---|---|---|---|
| **SS1** | 6 323 | 3 107 | 4 474 | 1 546 | 1 069 | **16 519** |
| **SS2** | 3 774 | 5 576 | 4 130 | 3 748 | 3 833 | **21 061** |
| **SS4** | 6 996 | 4 541 | 9 566 | 8 076 | 6 711 | **35 890** |
| **SS7** | 4 074 | 5 814 | 3 748 | 5 530 | 5 465 | **24 631** |
| **Total** | **21 167** | **19 038** | **21 918** | **18 900** | **17 078** | **98 101** |

#### 4.3.2.3 Spectral indices

Spectral indices are band equations designed to create image features that highlight specific attributes in a data set (Campbell & Wynne 2011). These indices have been widely proven to aid the classification of plasticulture (Aguilar et al. 2014; Ihuoma & Madramootoo 2019; Levin et al. 2007; Lu, Tao & Di 2018; Yang et al. 2017). The most popular indices that have been applied to the mapping of agricultural nets are vegetation indices, specifically the NDVI (Levin et al. 2007), the optimized soil-adjusted vegetation index (OSAVI) (Ihuoma & Madramootoo 2019) and the enhanced vegetation index (EVI) (Aguilar et al. 2014); as well as specialized plasticulture indices, such as the plastic-mulched land cover index (PMLI) (Lu, Tao & Di 2018) and the plastic greenhouse index (PGI) (Yang et al. 2017). Each of these five indices was calculated according to the respective equations given in Table 4.3 and each applied as an additional predictor variable.

Table 4.3 Spectral indices used as additional predictor variables

| Spectral Index | Equation |
|---|---|
| **NDVI** | $\frac{B8 - B4}{B8 + B4}$ |
| **OSAVI** | $\frac{B8 - B4}{B8 + B4 + 0.16}$ |
| **EVI** | $2.5 \times \frac{B8 - B4}{B8 + C1 * B4 - C2 * B2 + L}$ |
| **PMLI** | $\frac{B8 - B3}{B8 + B3}$ |
| **PGI** | $\frac{B2 * (B8 - B4)}{1 - Mean(B2 + B3 + B4)}$ |

Note: B is the Sentinel-2 band; C1 = 6, C2 = 7.5, L = 1

#### 4.3.2.4 Texture measures

Image texture, defined as the visual effect caused by spatial variation in tonal quantity over a relatively small area, plays an important role in discerning differences between land cover classes (Liang, Li & Wang 2012). There are several methods for quantifying image texture, a frequently used one being a grey-level co-occurrence matrix (GLCM). The use of GLCM, first proposed by Julesz (1962), describes the occurrence of value pairs within an image window using a matrix. This approach has become fundamental in land cover classification methods and has been proven to improve the classification of plasticulture (Agüera, Aguilar & Aguilar 2008; Carvajal et al. 2006). Seven texture features were selected for inclusion in the feature set, namely mean, variance, homogeneity, contrast, dissimilarity, entropy and angular second moment (ASM). The selection of window size has a major impact on performance of the texture features for classification (Sothe et al. 2017). The features were therefore calculated for each of the bands with a window size of seven pixels, as recommended by Zvoleff (2020) .

### 4.3.3 Feature selection

The full feature set is detailed in Table 4.4, the set containing: the 12 Sentinel-2 bands, the NDVI, the OSAVI, the EVI, the PMLI and the PGI spectral indices, as well as the GLCM texture features which are mean, variance, homogeneity, contrast, dissimilarity, entropy and ASM for each of the 12 bands. Two approaches to the reduction of dimensionality were evaluated. First, the features were grouped into ten semantic subsets. Aside from reducing the number of features, this approach is a proven way of providing insight into the factors driving classification accuracies (Campos-Taberner et al. 2019).

Table 4.4 Feature set considered for classification agricultural nets covering table grapes

| Type | Feature | Total number of features |
|---|---|---|
| **Spectral bands** | B1, B2, B3, B4, B5, B6, B7, B8, B8A, B9, B11, B12 | 12 |
| **Spectral indices** | NDVI, OSAVI, EVI, PMLI, PGI | 5 |
| **GLCM texture features** | mean, variance, homogeneity, contrast, dissimilarity, entropy and ASM | 84 |

These subsets are: (1) the 12 bands (BANDS); (2) the 12 bands and the NDVI index (BANDS + NDVI); (3) the 12 bands and the OSAVI index (BANDS + OSAVI); (4) the 12 bands and the EVI index (BANDS + EVI); (5) the 12 bands and the PMLI index (BANDS + PMLI); (6) the 12 bands and the PGI index (BANDS + PGI); (7) all the indices (INDICES); (8) all the texture features (TEXTURE); (9) the 12 bands and all five indices (BANDS + INDICES); and (10) the 12 bands and the texture features (BANDS + TEXTURE). Second, feature selection was performed using the random forest recursive feature elimination (RF-RFE) algorithm on the full feature set. The removal of redundant or irrelevant features through feature selection is an established way of improving the accuracy of ML classifications (Khalid, Khalil & Nasreen 2014). The RF-RFE algorithm provides a solution to the problem of high-dimensional data sets by recursively training a random forest model and removing the lowest preforming features (Darst, Malecki & Engelman 2018). The model gives insights into the best preforming features and the effects of the size of feature sets has on the performance (Kuhn 2015). The caret library was used to preform RF-RFE in the R programming language (Kuhn 2015). The variable importance scores of the RF-RFE analysis were used to select features subsets of 10, 20, 40, 60, 80 and 101 features. A correlation matrix was constructed to determine the association between the different features. The absolute correlation coefficient can be interpreted in the following manner: values of 0 to 0.09 indicate negligible correlation, values of 0.1 to 0.39 indicate weak correlation, values of 0.4 to 0.69 indicate moderate correlation and values greater than 0.7 indicate high correlation (Schober & Schwarte 2018).

### 4.3.4 Classification of nets

The caret library, implemented using R, was used to execute the RF, the SVM and the NN classifiers (Kuhn 2015). The parameters were set according to the library recommendations for RF and NN. However, grid search was used to select the most appropriate parameters for SVM. Grid search is an exhaustive search algorithm that optimizes SVM parameters based on cross-validation as a performance metric (Syarif, Prugel-Bennett & Wills 2016). Furthermore, the linear kernel

function was used for SVM, as recommended by Hasituya et al. (2016) for the classification of plastic-covered vegetation. Each feature subset–classifier combination was iterated 100 times to allow for stochastic variations.

### 4.3.5 Accuracy assessment

Study sites SS3, SS5, SS6 and SS8, were used as reference sites to test the performance of the classifiers. Visual interpretation of the Sentinel-2 imagery, the aerial imagery and the Elsenburg fly-over data set was done to create reference masks for the presence (1) and absence (0) of agricultural nets in the four reference sites. These masks were used to construct binary confusion matrices for each classification iteration. Table 4.5 details the number of pixels included in the presence (1) and absence (0) classes for each reference site.

Table 4.5 Number of pixels indicating the presence and absence of nets for each reference mask

| Study site | SS3 | SS5 | SS6 | SS8 | Total |
|---|---|---|---|---|---|
| **Nets present (1)** | 3 840 | 31 277 | 5 724 | 17 057 | **57 898** |
| **Nets absent (0)** | 155 760 | 128 723 | 153 477 | 142 943 | **580 903** |
| **Total** | 159 600 | 160 000 | 159 201 | 160 000 | **638 801** |

Confusion matrices compare classified data with reference data and they are used to derive a number of meaningful statistics to quantify the accuracy of classifications (Tharwat 2018). Thus a confusion matrix was constructed and used to calculate the overall accuracy, kappa statistic and balanced accuracy. Overall accuracy and the kappa statistic respectively indicate the percentage of correctly classified pixels and the true agreement of pixels. These statistics are the most commonly implemented accuracy metrics for land cover classifications (Foody 2002). However, these methods produce biased results when applied to unbalanced data sets. Table 4.5 clearly shows an unbalanced data set with the total number of pixels representing the absence of nets far exceeding the number of pixels indicating the presence of nets. Therefore the balanced accuracy (BA) metric, which compensates for the differences in the number of pixels that indicate the presence or absence of nets, was included (Luque et al. 2019). The McNemar test was used to test the statistical significance of the differences between classifier performances. McNemar's test is a non-parametric test that uses the chi-squared value of dichotomous data to produce a P-value as output (Pembury Smith & Ruxton 2020). In this case P-values lower than 0.05 were considered significant.

## 4.4 RESULTS

The results produced by the procedures outlined in the preceding section are summarized in the following subsections, namely the spectral profile of the classes, the results of the feature selection and feature ranking, and the classification accuracy scores are visualized. The confusion matrix for each individual classification can be found in Appendix B.

### 4.4.1 Spectral profile of classes

Figure 4.2 shows the mean spectral reflectance of each land cover class over the 12 Sentinel-2 bands. The error bars represent the standard deviation of the spectral response per band.

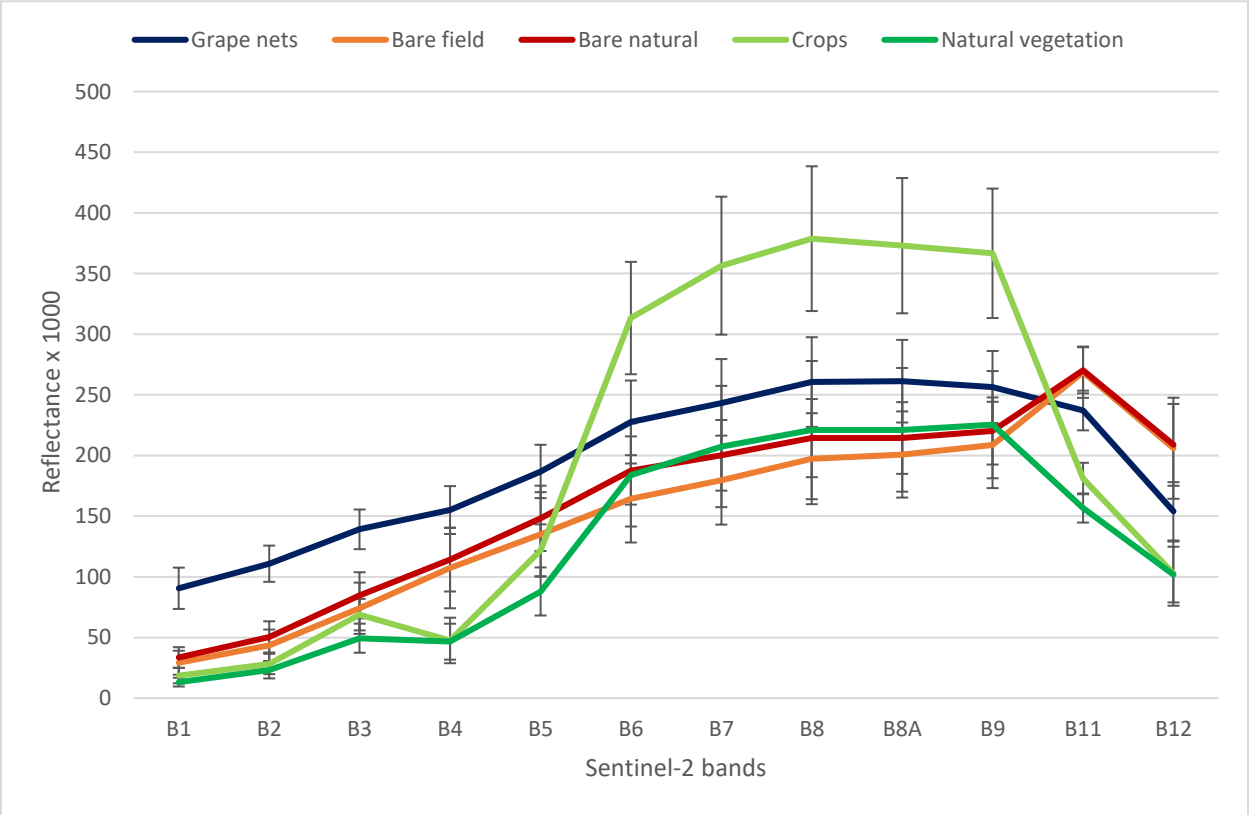


Figure 4.2 The mean spectral signature of each land cover class with the standard deviation displayed as error bars

The *grape nets* signature has higher reflectance in bands 2, 3 and 4, which corresponds to the visible region, compared to those of the other classes. In the RE to the near-infrared (NIR) regions (bands 6, 7, 8 and 8A) the reflectance of *grape nets* is lower than that of the *crops* class, but higher than *natural vegetation*, *bare fields* and *bare natural*. For bands 11 and 12 (SWIR), the reflection of *grape nets* is lower than the *bare field* and *bare natural* classes but higher than the *crops* and *natural vegetation* classes. The standard deviation of the *grape nets*, *crops* and *natural vegetation* signatures are larger in the RE and NIR (bands 6, 7, 8 and 8A) regions than in the visible (bands 2,3 and 5) and SWIR (bands 11 and 12) regions.

### 4.4.2 Feature selection

The rank allocated to each feature by the RF-RFE algorithm is listed in Table 4.6.

Table 4.6 Rank (#) achieved by each classification feature as produced by RF-RFE

| # | Feature | # | Feature | # | Feature | # | Feature | # | Feature |
|---|---|---|---|---|---|---|---|---|---|
| 1 | B12 mean | 21 | B4 mean | 41 | NDVI | 61 | B2 homogeneity | 81 | B8 contrast |
| 2 | B12 variance | 22 | B1 mean | 42 | PMLI | 62 | B2 contrast | 82 | B6 ASM |
| 3 | B11 mean | 23 | B3 mean | 43 | B12 dissimilarity | 63 | B11 contrast | 83 | B5 dissimilarity |
| 4 | B11 variance | 24 | B1 variance | 44 | B7 mean | 64 | OSAVI | 84 | B5 homogeneity |
| 5 | B9 mean | 25 | B12 contrast | 45 | B2 entropy | 65 | B8 entropy | 85 | B6 dissimilarity |
| 6 | B9 variance | 26 | B6 Variance | 46 | B8 mean | 66 | B4 contrast | 86 | B9 homogeneity |
| 7 | B11 | 27 | B2 ASM | 47 | B5 contrast | 67 | B2 dissimilarity | 87 | B11 homogeneity |
| 8 | B5 mean | 28 | B12 entropy | 48 | B4 entropy | 68 | B1 entropy | 88 | B8A |
| 9 | B12 | 29 | B3 | 49 | B3 contrast | 69 | B7 | 89 | B8A ASM |
| 10 | B5 variance | 30 | B4 ASM | 50 | EVI | 70 | B1 ASM | 90 | B7 ASM |
| 11 | B2 mean | 31 | B9 | 51 | B11 ASM | 71 | PGI | 91 | B8A contrast |
| 12 | B1 | 32 | B8 ASM | 52 | B7 variance | 72 | B9 ASM | 92 | B11 dissimilarity |
| 13 | B8A variance | 33 | B4 variance | 53 | B9 dissimilarity | 73 | B9 entropy | 93 | B8 dissimilarity |
| 14 | B2 variance | 34 | B3 ASM | 54 | B6 contrast | 74 | B5 ASM | 94 | B7 entropy |
| 15 | B8A mean | 35 | B2 ASM | 55 | B2 | 75 | B4 dissimilarity | 95 | B8A entropy |
| 16 | B6 | 36 | B3 variance | 56 | B3 homogeneity | 76 | B1 homogeneity | 96 | B6 homogeneity |
| 17 | B1 contrast | 37 | B1 dissimilarity | 57 | B11 entropy | 77 | B8 homogeneity | 97 | B7 dissimilarity |
| 18 | B5 | 38 | B12 homogeneity | 58 | B4 homogeneity | 78 | B6 entropy | 98 | B8 |
| 19 | B6 mean | 39 | B3 entropy | 59 | B4 | 79 | B5 entropy | 99 | B7 homogeneity |
| 20 | B9 Contrast | 40 | B8 variance | 60 | B3 dissimilarity | 80 | B7 contrast | 100 | B8A homogeneity |
| | | | | | | | | 101 | B8A dissimilarity |

Bands 11 and 12 (SWIR bands), along with their respective mean and variance texture features, are ranked in the top ten feature positions. Bands 8, 8A and 7 (NIR bands), with several of their corresponding texture features, are ranked the lowest and comprise 13 out of the 20 lowest ranked features. The visible bands (bands 2, 3 and 4) and the texture features derived from the visible bands generally rank higher than the RE and NIR features, but lower than the SWIR features. The mean and the variance texture features have high ranks, representing 17 out of the first 25 ranked

features. Furthermore, the spectral indices are ranked lower than the spectral bands and texture features, that is they are ranked lower than the top 40 features. The correlation matrix shows that the visible bands (bands 2, 3 and 4) are highly correlated with one another (Appendix C). Similarly, the NIR and RE bands (bands 6, 7, 8 and 8A) are highly correlated and the SWIR bands (bands 11 and 12) are highly correlated with one another. There is also a high correlation between each group of spectral bands (VIS, NIR + RE, and SWIR) and their corresponding mean, variance and homogeneity texture features. The remaining texture features, namely contrast, dissimilarity, entropy and ASM, show low correlation with the spectral bands and other texture features.

### 4.4.3 Image classification

Sixteen different feature combinations (scenarios) of features were used to classify the nets. The mean overall accuracy (OA), the kappa statistic (KS) and the BA of the test sites are summarized for each classification in Table 4.7. Each classification scenario is numbered (#) and the number of features (n) used in each scenario for RF, SVM and NN are shown.

The best individual classification scores (OA = 97%, KS = 0.87, BA = 87%) were achieved using the NN classifier for Scenario 10 for which the spectral bands and texture features were used as input. The McNemar test confirmed that the differences between this result and the other classification results are statistically significant. The column averages given in Table 4.7 represent the overall performance of each classifier. Both RF and NN achieved an averaged OA (AOA) of 95% and an averaged BA (ABA) of 84%, although the averaged KS (AKS) of NN (0.76) is slightly higher than that of RF (0.75). The SVM (AOA = 89%, AKS = 0.63, ABA = 78%) classifier achieved significantly lower accuracies than those of NN and RF.

The row averages in Table 4.7 indicate the overall performance of each feature set. Scenario 10 (BANDS + TEXTURE) has the highest AOA (96%), AKS (0.78) and ABA (86%). This performance is followed closely by Scenarios 14 (RF-RFE 60) and 9, which also achieved AOAs of 96%, but lower AKS (0.77) and ABA (85%) scores. Scenario 14 is based on the first 60 features recommended by RF-RFE for classification, while Scenario 9 used the spectral bands and spectral indices for classification. The accuracies of these two scenarios were only marginally higher than that of Scenario 1, where only the Sentinel-2 bands were used for classification. When RF and SVM are used as classifiers, the inclusion of texture features (Scenario 10) and spectral indices (Scenario 9) result in an increase in accuracy that is not statistically significant. By contrast, the inclusion of texture features does result in a statistically significant increase in accuracy when NN is used as the classifier. Moreover, the average accuracies of Scenarios 7 and 8, where the indices and texture features are used without the spectral bands respectively, are lower than when only the bands are used as in Scenario 1.

Table 4.7 Mean overall accuracy (OA), kappa statistic (KS) and balanced accuracy (BA) of the four test sites for each classification scenario

| # | Scenario | n | RF | | | SVM | | | NN | | | Ave | | |
|---|---|---|---|---|---|---|---|---|---|---|---|---|---|---|
| | | | OA | KS | BA | OA | KS | BA | OA | KS | BA | OA | KS | BA |
| 1 | BANDS | 12 | 0.96 | 0.79 | 0.85 | 0.95 | 0.71 | 0.83 | 0.94 | 0.72 | 0.83 | 0.95 | 0.74 | 0.84 |
| 2 | BANDS + NDVI | 13 | 0.95 | 0.79 | 0.85 | 0.94 | 0.70 | 0.83 | 0.95 | 0.77 | 0.84 | 0.95 | 0.75 | 0.84 |
| 3 | BANDS + OSAVI | 13 | 0.95 | 0.79 | 0.85 | 0.93 | 0.66 | 0.82 | 0.94 | 0.72 | 0.83 | 0.94 | 0.72 | 0.83 |
| 4 | BANDS + EVI | 13 | 0.95 | 0.79 | 0.85 | 0.93 | 0.66 | 0.82 | 0.95 | 0.77 | 0.84 | 0.95 | 0.74 | 0.84 |
| 5 | BANDS + PMLI | 13 | 0.95 | 0.79 | 0.85 | 0.93 | 0.66 | 0.82 | 0.96 | 0.78 | 0.85 | 0.95 | 0.74 | 0.84 |
| 6 | BANDS+ PGI | 13 | 0.95 | 0.79 | 0.85 | 0.94 | 0.68 | 0.83 | 0.94 | 0.76 | 0.84 | 0.95 | 0.74 | 0.84 |
| 7 | INDICES | 5 | 0.93 | 0.66 | 0.82 | 0.83 | 0.45 | 0.73 | 0.92 | 0.64 | 0.81 | 0.89 | 0.58 | 0.78 |
| 8 | TEXTURE | 84 | 0.93 | 0.66 | 0.82 | 0.94 | 0.70 | 0.83 | 0.95 | 0.74 | 0.84 | 0.94 | 0.71 | 0.83 |
| 9 | BANDS + INDICES | 17 | 0.96 | 0.80 | 0.85 | 0.94 | 0.71 | 0.83 | 0.96 | 0.78 | 0.85 | 0.96 | 0.77 | 0.84 |
| 10 | BANDS + TEXTURE | 96 | 0.95 | 0.80 | 0.85 | 0.95 | 0.73 | 0.84 | 0.97 | 0.82 | 0.87 | 0.96 | 0.78 | 0.86 |
| 11 | RF-RFE 10 | 10 | 0.92 | 0.66 | 0.81 | 0.49 | 0.11 | 0.39 | 0.93 | 0.67 | 0.82 | 0.78 | 0.48 | 0.67 |
| 12 | RF-RFE 20 | 20 | 0.95 | 0.76 | 0.84 | 0.90 | 0.64 | 0.79 | 0.95 | 0.79 | 0.84 | 0.94 | 0.73 | 0.83 |
| 13 | RF-RFE 40 | 40 | 0.96 | 0.79 | 0.85 | 0.94 | 0.73 | 0.83 | 0.95 | 0.76 | 0.84 | 0.95 | 0.76 | 0.84 |
| 14 | RF-RFE 60 | 60 | 0.96 | 0.80 | 0.85 | 0.95 | 0.74 | 0.84 | 0.96 | 0.79 | 0.85 | 0.96 | 0.77 | 0.84 |
| 15 | RF-RFE 80 | 80 | 0.96 | 0.80 | 0.85 | 0.94 | 0.72 | 0.83 | 0.96 | 0.78 | 0.84 | 0.95 | 0.77 | 0.84 |
| 16 | RF-RFE All | 101 | 0.96 | 0.80 | 0.85 | 0.95 | 0.73 | 0.83 | 0.96 | 0.76 | 0.85 | 0.95 | 0.76 | 0.84 |
| | | Ave | 0.95 | 0.75 | 0.84 | 0.89 | 0.63 | 0.78 | 0.95 | 0.76 | 0.84 | 0.93 | 0.71 | 0.82 |

The accuracies of Scenarios 11 to 16, where the RF-RFE feature subsets were tested, increased as subset size increased. However, no significant improvements were achieved when using more than 40 features for any of the classifiers. Figure 4.3 illustrates the effect that feature subset size has on classification accuracy. The RF-RFE algorithm was used to rank the features and these features were then added in the order of their ranking to create the subsets. Accuracy increased as the number of variables in the feature subset increased, although, the rate of increase varied significantly with the number of features.

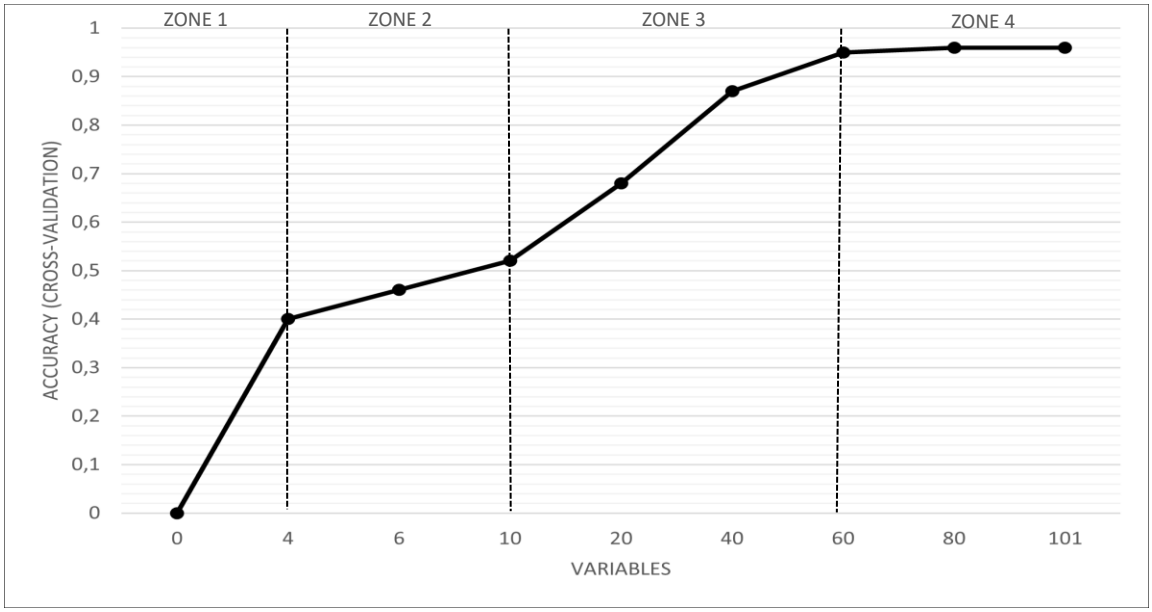


Figure 4.3 Accuracy achieved for different feature subset sizes by RF-RFE feature selection

Figure 4.3 is divided into four zones each based on the rate of change in accuracy. From zero to four features (Zone 1) accuracy increases rapidly (by 41%) and in zone 2 (four to 10 features) accuracy increases moderately (12%). Between 10 and 60 features (Zone 3) accuracy increases rapidly (43%) and in Zone 4 (60 to 101 features) the accuracy increases with less than 1%.

The agricultural nets classified by RF, SVM and NN for Scenario 14 (RF-RFE60) were compared to the Sentinel-2 reference imagery in Figure 4.4. The red polygons represent the perimeter of the reference nets and the blue polygons show the pixels classified as nets. Blue polygons that fall within the red outline represent correctly classified nets, whereas red outlines with no blue polygons represent nets that have been grouped into another class (i.e. they represent omission errors). Blue polygons that fall outside the red polygons represent other land cover that has been incorrectly classified as nets (i.e. they represent commission errors).

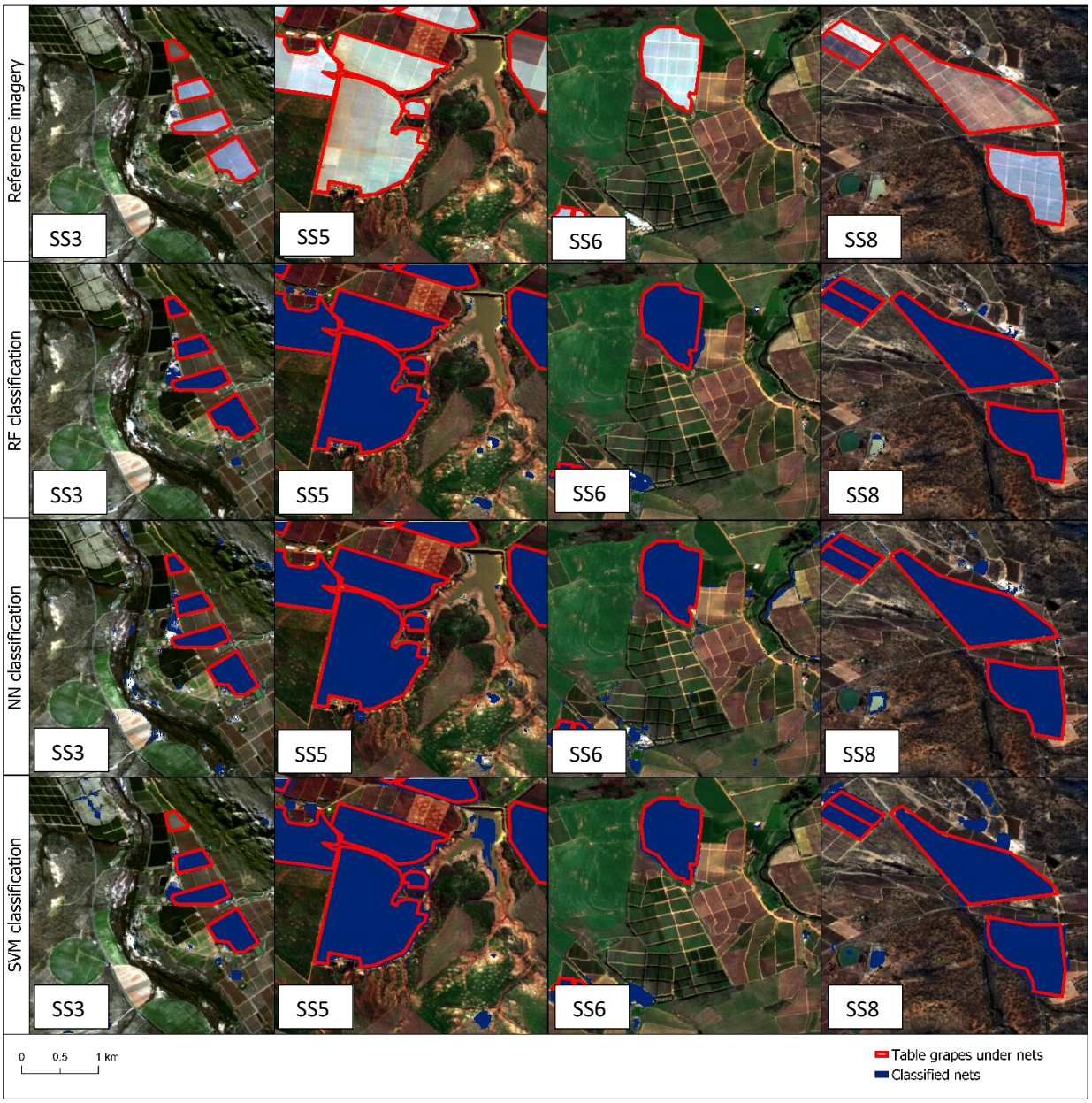


Figure 4.4 Classified agricultural nets produced by the RF, SVM and NN classifiers for Scenario 14 (RF-RFE60) compared to Sentinel-2 reference imagery

Figure 4.4 shows that the RF and the NN classifiers have made no errors of omission, while SVM failed to classify a vineyard net in the northern region of SS3. All three classifiers produce a considerable number of commission errors. These errors primarily originate from the misclassification of waterbodies, buildings and bare fields.

## 4.5 DISCUSSION

Overall, the classifications for RF and NN achieve comparable accuracies to those of other studies that mapped plasticulture. For example, Carvajal et al. (2006) achieved a general accuracy of 83% using QuickBird imagery to detect plastic greenhouses; Tarantino & Figorito (2012) achieved an

average OA of 90.3% for all study sites when mapping plastic-covered vineyards with aerial imagery; Aguilar et al. (2014) achieved an OA of 97.5% while mapping agricultural nets with WorldView-3 and GeoEye-1 imagery; and Aguilar et al. (2016) achieved an average OA of 98% using WorldView-3 imagery to map plastic greenhouses. When using medium- and high-resolution imagery, Aguilar et al. (2015) achieved a maximum OA of 79.1% for mapping greenhouse crops using Landsat-8; Novelli et al. (2016) achieved an OA of 91% using Sentinel-2 imagery to map plastic greenhouses; Yang et al. (2017) achieved an accuracy of 91.8% using Landsat-8 data to map plastic greenhouses; and González-Yebra et al. (2018) classified plastic greenhouses using Landsat 5 TM and Landsat 7 ETM + imagery and achieved a best OA of 93.4%. The OA scores achieved by RF and NN in this study (Table 4.7) exceed 90% for all the scenarios and thus fall within a range comparable to those of other studies. More specifically, the accuracies achieved by NN and RF are similar to those gained by methods that use very-high-resolution imagery, such as Worldview-3 imagery (Aguilar et al. 2015) or QuickBird imagery (Carvajal et al. 2006), and they exceed the Oas of studies that use Landsat imagery (Aguilar et al. 2015; González-Yebra et al. 2018). Figure 4.4 confirms that there are no errors of omission for the RF and NN classifiers. Levin et al. (2010) compared Landsat-8 imagery and hyperspectral AISA-ES imagery to map agricultural nets and concluded that the coarse spectral and spatial resolutions of the Landsat-8 data caused significant errors of omission for the nets class. The results illustrated in Figure 4.4 validate Sentinel-2 imagery as having a better detection rate for agricultural nets than that of Landsat-8 imagery. It is safe to conclude that Sentinel-2 imagery has the necessary spatial and spectral resolutions to map agricultural nets at regional scale.

Both RF and NN consistently achieved higher accuracies than SVM (Table 4.7). Several studies (Hasituya et al. 2017; Hasituya & Chen 2017; Lu, Tao & Di 2018; Novelli et al. 2016; Sun et al. 2021) have already demonstrated RF to be an effective classifier for mapping plasticulture. Hasituya & Chen (2017) even found that RF significantly outperformed SVM in all the scenarios for mapping PML using Landsat-8 imagery. The superior performance of the RF algorithm achieved in the present study is therefore consistent with the evidence in the existing literature. However, limited studies have investigated NN for mapping plasticulture, particularly agricultural nets. Ma et al. (2019) discuss the benefits and applications of NN in remote sensing and pointed out that this algorithm is especially effective for urban classifications using imagery with resolutions of 10 m or smaller. The mapping of plasticulture has often been compared to urban mapping as the spectral signatures of both types of land cover represent a mixture of artificial surfaces and vegetation (Levin et al. 2010). Therefore, NN's ability to map complex urban settings using high-resolution imagery may explain why the classifier performs well for mapping agricultural nets in the present study. The NN classifier also achieves the best overall classification

result using spectral bands and texture features for classification. These results corroborate Carvajal et al.'s (2006) findings that the addition of GLCM texture features improvs the overall accuracy of plastic greenhouse mapping using NN with QuickBird imagery. Furthermore, Sun et al.'s (2021) comparison of NN, RF and SVM for mapping plastic greenhouses determined that NN consistently outperformed the other classifiers.

Recall that Table 4.6 shows that the SWIR (bands 11 and 12) and visible bands (bands 2, 3 and 4) rank higher than the NIR and RE bands (bands 6, 7, 8 and 8A), and that the texture features rank higher than the spectral indices. Recall also that Figure 4.2 shows that the standard deviation of the visible and SWIR bands is smaller than that of the NIR bands. High intra-class variation decreases the separability of classes and thus decreases classification accuracy (Debba, Cho & Mathieu 2009). This probably explains why the visible and SWIR bands, which have lower degrees of spectral variation, are ranked above the RE and NIR bands. Spectral indices, such as NDVI, have been proven to significantly improve plasticulture classification accuracies toward the end of the growing season (Hasituya & Chen 2017). However, these indices become less effective when crops are dormant under nets as these nets have similar NDVI values to other types of land cover such as urban and bare soil. By contrast, texture features have been shown to aid the classification of plasticulture, regardless of crops' phenological stages (Hasituya & Chen 2017). This quite likely explains why the texture features rank higher than the spectral indices and also why Scenario 10 (BANDS + TEXTURE) achieves the highest average accuracies. Table 4.6 also shows that the mean and variance are the highest rated texture features. This agrees with Hasituya & Chen (2017), Agüera, Aguilar & Aguilar (2008) and Aguilar et al. (2016) who all noted that the mean texture feature is the most important texture feature for mapping plasticulture. However, the present study's correlation matrix (Appendix C) shows that the mean and variance texture features of the different bands are highly correlated with the unaltered Sentinel-2 bands suggesting that a number of these features have been duplicated.

The row averages in Table 4.7 show how well each feature set preforms. Scenario 10 (BANDS + TEXTURE) performs best, followed by Scenario 9 (BANDS + INDICES) and Scenario 14 (RF-RFE 60). However, the accuracies for these three scenarios are only marginally higher than that of Scenario 1 (BANDS). This marginal increase is likely attributable to the inclusion of texture features and spectral indices that cause no significant increase in the accuracies for RF and SVM. Perilla & Mas (2019) tested a range of different features, including GLCM texture features, NDVI, PMLI and PGI, to map mixed plasticulture using Sentinel-2 imagery with the maximum entropy classifier. They found a high correlation and redundancy among these ancillary features and the Sentinel-2 bands. Consequently, the ancillary features made no significant improvement to the

classification accuracy when used in combination with the Sentinel-2 bands (Perilla & Mas 2019). In the present study the correlation matrix (Appendix C) shows high correlation between the spectral bands and the texture features, and between the spectral bands and the spectral indices. This explains why the spectral indices and texture features make no significant difference to the classification accuracy for the RF and SVM classifiers (Table 4.7). All the classifiers show decreases in accuracy when the spectral indices only (Scenario 7) and the texture features only (Scenario 8) are used, in comparison to when the spectral bands are used (Scenario 1). These results suggest that the untransformed Sentinel-2 bands contain the most valuable information for mapping vineyards under nets.

Scenarios 11 to 16 (Table 4.7) that use the RF-RFE feature subsets show no significant improvement in accuracy when using more than 40 features. This plateau in accuracy can be further explained by the high correlations among the bands, indices and texture features. Hasituya & Chen (2017) had used RF-RFE to select features to classify PML using Landsat-8 imagery. The features included the Landsat-8 bands, vegetation indices, derivatives of reflectance, GLCM texture features and thermal features. The results showed that for three of the four acquisition dates, no significant improvement in accuracy was achieved when using more than 44 features (Hasituya & Chen 2017).

The results of the present study show that Sentinel-2 imagery has the necessary spectral and spatial resolutions to effectively map agricultural nets and moreover, RF and NN turn out to be effective classifiers for such an application. Clearly, more research is required to investigate object-based versus per-pixel classification approaches using Sentinel-2 imagery; the use of different feature selection methods; and the use of different classification schemes (class nomenclature and configurations). Three other further avenues of research are to evaluate the ability of Sentinel-2 imagery to map different crop types under agricultural nets, to investigate the fusion of synthetic aperture radar data and to examine multitemporal imagery for classification purposes.

## 4.6 CONCLUSION

The complex spectral properties of agricultural nets have long challenged the ability of existing remote sensing strategies to map and monitor agricultural regions (Levin et al. 2010). This has engendered the need to develop a regional crop mapping solution that includes crops under nets. Within this context, the current study aimed primarily to evaluate the potential of Sentinel-2 imagery to map agricultural nets covering table grapes and secondly to gain insight into which machine learning (ML) classifiers and image features can most effectively classify agricultural nets.

These goals were pursued by first acquiring Sentinel-2 imagery for eight study sites in the Western Cape. Four of these sites were earmarked for the collection of training data, to be used to classify the remaining four sites using the RF, the SVM and the NN classifiers. Sixteen different feature sets that include different combinations of the Sentinel-2 bands, spectral indices and GLCM texture features were evaluated for each test site. The results provide novel insights into the performance of Sentinel-2 imagery for mapping nets, as well as which features and classifiers aid this classification. Overall, both RF and NN proved to be reliable classifiers to map agricultural nets, whereas SVM proved less effective. The highest OA of 97%, kappa statistic (KS) of 0.87 and BA of 87% were achieved by the NN classifier with spectral bands used in combination with texture features. However, the results show that the untransformed Sentinel-2 bands contain the most important spectral information for the classification. Notably, the results of the classification show that the use of Sentinel-2 imagery achieve higher accuracies and higher detection rates for agricultural nets compared to studies that used lower resolution Landsat imagery. Furthermore, the accuracies achieved in this study are comparable with those achieved using very-high-resolution imagery. This supports the conclusion that Sentinel-2 imagery has the necessary spectral and spatial resolutions for mapping agricultural nets. Given these new insights, the frequent revisit time of Sentinel-2 and the fact that Sentinel-2 imagery is freely available, Sentinel-2 imagery is evidently a practical and viable source of imagery for mapping agricultural nets at regional scale. The various methods evaluated and demonstrated in this study provide a logical foundation for developing and operationalizing a solution to the problem of mapping agricultural nets in the Western Cape, which is essential for gauging the environmental and hydrological impacts of modern agricultural practices.

# CHAPTER 5: SYNTHESIS AND CONCLUSIONS

In this concluding chapter the findings of the study are evaluated in the context of finding an operational solution for mapping agricultural nets and the crops that are grown under the nets. The findings of the study are summarized, the aims and objectives are revised, the value of the study is evaluated, the limitations are pointed out, recommendations are made and final conclusions are drawn.

## 5.1 REVISITING THE AIMS AND OBJECTIVES

The uses and nature of agricultural nets was introduced in Chapter 1. The rapidly growing use of such nets has complicated existing remote sensing methods for mapping and monitoring agriculture. It is therefore imperative that these methods be modified to include areas under nets. A key aspect of addressing this problem is to investigate the use of Sentinel-2 imagery for mapping agricultural nets at a regional scale. This study set out to achieve this goal. The primary aim was to develop a spectral profile of agricultural nets using Sentinel-2 imagery and the secondary aim was to demonstrate how the spectral profile can be used to map agricultural nets and specific crops grown under nets. This study set out to accomplish the aims by setting six objectives, the pursuance of which is reported in Chapters 2 to 4.

In Chapter 2 Objective 1 was addressed by examining the literature relating to the spectral properties of agricultural nets, the classification strategies suitable for mapping these nets, as well as a range of relevant remote sensing techniques and approaches to accuracy assessment. Chapter 3 and 4 both report on the acquisition of Sentinel-2 imagery and therefore fulfil the requirements of Objective 2. Spectral signatures were constructed for vineyards, citrus and berries grown under nets (Objective 3). These signatures were compared to the signatures of surrounding land cover to investigate the effects that seasonal variations of the underlying crops have on the net signatures (Objective 4). These were used to develop and demonstrate a methodology for mapping nets covering table grapes using Sentinel-2 imagery (Objective 5). In the current chapter, the findings are summarized in the context of finding operational solutions to the problem of mapping crops under agricultural nets (Objective 6).

## 5.2 SYNTHESIS OF KEY FINDINGS

The literature review (Chapter 2) explored the concepts of remote sensing, image classification and accuracy assessment as they relate to the mapping of plasticulture. The review provided several insights that formed the basis of the methods employed in Chapters 3 and 4. Several studies

found that very-high-resolution imagery achieved high accuracies for mapping plasticulture (Aguilar et al. 2015; Aguilar et al. 2016; Novelli et al. 2016; Shen & Sarris 2008), while the use of lower-resolution Landsat imagery resulted in significant misclassification errors (Aguilar et al. 2016; Rodriguez-Galiano et al. 2012). Sentinel-2 imagery was recommended by Sun et al. (2021) for mapping plasticulture as this imagery has a higher spatial resolution than Landsat and produced high accuracies for the classification of plastic greenhouses. Additionally it was determined that very-high-resolution imagery, such as WorldView-3, is prohibitively expensive for regional mapping tasks, whereas Sentinel-2 imagery is freely available and has global coverage. Based on the literature review it was concluded that Sentinel-2 imagery would be a more practical source of data for mapping plasticulture. Prior to the present study, no study has investigated the use of Sentinel-2 imagery for mapping agricultural nets.

Borgogno-Mondino, Palma & Novello (2020) compared the spectral signatures of agricultural nets and uncovered crops over the course of year and found that the signatures of the agricultural nets showed significant temporal changes. However, their study did not determine whether the signatures of the agricultural nets were spectrally separable from the uncovered crops or other land cover. To determine whether Sentinel-2 imagery is a viable source of data for mapping agricultural nets, the spectral properties of these nets, as captured by Sentinel-2, and different classification techniques needed to be investigated for this purpose. The primary intention of Chapter 3 was therefore to identify and interpret the spectral signatures, as captured by Sentinel-2 imagery, of different agricultural nets, the crops that they cover and the surrounding land cover. The purpose was to evaluate whether Sentinel-2 imagery has the necessary spatial and spectral resolutions to distinguish agricultural nets from their surrounding land cover. The secondary purpose of Chapter 3 was to investigate the effect of temporal variation on the separability of the net signatures. The spectral signatures of the nets were compared to the corresponding signatures of their uncovered crop types for each season (i.e. summer, autumn, winter, spring). The results show that a reliable signature of the crops under agricultural nets can be extracted from Sentinel-2 imagery, as the signature of the covered crops mimic the shape and seasonal changes of the signatures of the corresponding uncovered crops. The separability between each crop type under nets was compared to the surrounding land cover classes per season. The separability scores showed that the signatures of the nets were distinguishable from the signatures of surrounding land cover. The separability analysis also showed that summer, particularly toward the end of December, was the best time to separate nets covering different crop types from surrounding land cover. The insights obtained form the foundation of developing a strategy for mapping nets at regional scale using Sentinel-2 imagery.

The review of classification methods (Chapter 2) revealed that the RF, SVM and NN classifiers proved to be effective in combination with spectral indices and texture features to map plasticulture (Chaofan et al. 2016; Hasituya et al. 2016; Lu, Tao & Di 2018; Perilla & Mas 2019; Sun et al. 2021). However, these techniques have not been investigated for mapping agricultural nets using Sentinel-2 imagery. The intentions of Chapter 4 were therefore to evaluate the potential of Sentinel-2 imagery to identify and map nets covering table grapes and to determine which spectral features and classification algorithms are most effective for mapping nets. Classifications were conducted using the random forest (RF), support vector machine (SVM) and neural network (NN) algorithms to classify Sentinel-2 imagery collected for four study sites. Different feature subsets consisting of spectral indices, texture features and spectral bands were evaluated. Several studies, reviewed in Chapter 2, validated the use of the overall accuracy, kappa statistic and balanced accuracy metrics to access classification accuracy (Aguilar et al. 2015; Aguilar et al. 2016; Chaofan et al. 2016; González-Yebra et al. 2018; Hasituya et al. 2017; Lu, Di & Ye 2014). These metrics were therefore used in Chapter 4. RF and NN both achieved relatively high accuracies, whereas SVM proved to be less reliable for this application. Regarding classification features, the untransformed spectral bands proved to be the most effective for classification. The accuracies attained by specifically using RF and NN were better than those of other studies that used lower resolution (Landsat) imagery, and similar to studies that have used very-high-resolution imagery. Therefore, the results validate Sentinel-2 as a viable sensor for the regional mapping of agricultural nets. The insights obtained through this research add to the body of knowledge pertaining to agricultural net mapping.

## 5.3 LIMITATIONS AND RECCOMMENDATIONS FOR FUTURE RESEARCH

The study was limited by two factors. First, there was very little reference data available for covered crops. The use of agricultural nets is rapidly growing in South Africa, but the total area covered by nets is still small compared to countries such as Spain, China and the USA. As such, the use of nets in South Africa is sporadic and dispersed. This limitation had two major implications in this study. First, the different citrus and berry varieties were grouped into larger classes, namely *berry* and *citrus* to ensure sufficient reference data for spectral analysis. By grouping these crops certain spectral characteristics caused by the unique seasonal changes of each fruit variety were lost. Second, the mapping of nets was limited to those covering table grapes because test sites containing sufficient reference data for multiple crop types is rare.

Despite these limitations the study provides a sound foundation for future research. The development of a robust classification scheme for crops under nets would benefit from the spectral analysis of the individual citrus and berry varieties. The effect of spectral indices and texture

features on the separability of net signatures can be investigated to find out if these results align with classification results. The spectral analysis and the classification should both be expanded to investigate the spectral characteristics of other crops covered by nets, such as pome fruit, stone fruit, flowers and nuts. The study concentrated on four sites for training and four sites for testing to demonstrate the transferability of the method. Further research is required to test the method at regional scale.

## 5.4 CONCLUSIONS

Climate change has forced the agricultural sector to adapt to extreme weather conditions, variable rainfall and increased temperatures. Agricultural nets are a popular adopted strategy to cope with these extremes. However, the introduction of nets has created a need to develop new methods for mapping and monitoring our agricultural resources. This study aimed to access the capacity and usefulness of Sentinel-2 imagery for mapping agricultural nets. Although Sentinel-2 imagery is freely available and has a temporal resolution of five days – which makes it a practical and cost-effective source of data for mapping and monitoring large areas – it was initially unclear whether Sentinel-2 imagery had the necessary spatial and spectral resolutions to map nets. This investigation demonstrated that Sentinel-2 imagery has the requisite spectral resolution to capture distinct signatures of agricultural nets. The study also gives direction to the selection of image dates and the classification scheme design for mapping nets. The classifications achieved comparable accuracies to those gained by using very-high-resolution satellite imagery, like Worldview-3 and QuickBird. Furthermore, the unaltered Sentinel-2 bands were shown to contain the most valuable information for classification. The research confirms that Sentinel-2 imagery has adequate spatial and spectral resolutions for mapping nets, and the results of this study verify the effectiveness of machine learning classifiers and classification features for mapping nets.

The research has provided valuable insights into the spectral characteristics of nets, thereby laying the foundation for the development of a practical solution for mapping nets at regional scale. Such a solution will help to gauge the environmental impact of nets regarding plastic waste and it can be used for examining their hydrological impacts. Accurate agricultural maps enable the effective management and policy implementation of agricultural resources, which will contribute to improved food security.

[35 114]

# REFERENCES

Adams R, Hurd B, Lenhart S & Leary N 1998. Effects of global climate change on world agriculture: an interpretive review. *Climate Research* 11, 1: 19–30. [online]. Available from: http://www.int-res.com/abstracts/cr/v11/n1/p19-30/ [Accessed 28 February 2019].

Agüera F, Aguilar FJ & Aguilar MA 2008. Using texture analysis to improve per-pixel classification of very high resolution images for mapping plastic greenhouses. *ISPRS Journal of Photogrammetry and Remote Sensing* 63, 6: 635–646. [online]. Available from: https://www.sciencedirect.com/science/article/pii/S0924271608000270 [Accessed 11 February 2019].

Aguilar MA, Novelli A, Nemamoui A, Aguilar FJ, García Lorca A & González-Yebra Ó 2018. Optimizing Multiresolution Segmentation for Extracting Plastic Greenhouses from WorldView-3 Imagery. In 31–40. Springer, Cham. [online]. Available from: http://link.springer.com/10.1007/978-3-319-59480-4_4 [Accessed 14 May 2019].

Aguilar M, Bianconi F, Aguilar F, Fernández I, Aguilar MA, Bianconi F, Aguilar FJ & Fernández I 2014. Object-Based Greenhouse Classification from GeoEye-1 and WorldView-2 Stereo Imagery. *Remote Sensing* 6, 5: 3554–3582. [online]. Available from: http://www.mdpi.com/2072-4292/6/5/3554 [Accessed 14 February 2019].

Aguilar M, Nemmaoui A, Novelli A, Aguilar F, García Lorca A, Aguilar MA, Nemmaoui A, Novelli A, Aguilar FJ & García Lorca A 2016. Object-Based Greenhouse Mapping Using Very High Resolution Satellite Data and Landsat 8 Time Series. *Remote Sensing* 8, 6: 513. [online]. Available from: http://www.mdpi.com/2072-4292/8/6/513 [Accessed 15 February 2019].

Aguilar M, Vallario A, Aguilar F, Lorca A, Parente C, Aguilar MA, Vallario A, Aguilar FJ, Lorca AG & Parente C 2015. Object-Based Greenhouse Horticultural Crop Identification from Multi-Temporal Satellite Imagery: A Case Study in Almeria, Spain. *Remote Sensing* 7, 6: 7378–7401. [online]. Available from: http://www.mdpi.com/2072-4292/7/6/7378 [Accessed 21 May 2019].

Ahmad F 2012. Spectral vegetation indices performance evaluated for Cholistan Desert. *Journal of Geography and Regional Planning* 5, 6: 165–172. [online]. Available from: http://www.academicjournals.org/JGRP [Accessed 25 May 2019].

Al-Helal IM & Abdel-Ghany AM 2011. Measuring and evaluating solar radiative properties of plastic shading nets. *Solar Energy Materials and Solar Cells* 95, 2: 677–683. [online].

Available from: https://www.sciencedirect.com/science/article/pii/S0927024810005799 [Accessed 11 March 2019].

Amani M, Ghorbanian A, Ahmadi SA, Kakooei M, Moghimi A, Mirmazloumi SM, Moghaddam SHA, Mahdavi S, Ghahremanloo M, Parsian S, Wu Q & Brisco B 2020. Google Earth Engine Cloud Computing Platform for Remote Sensing Big Data Applications: A Comprehensive Review. *IEEE Journal of Selected Topics in Applied Earth Observations and Remote Sensing* 13: 5326–5350.

Amani M, Salehi B, Mahdavi S & Brisco B 2018. Spectral analysis of wetlands using multi-source optical satellite imagery. *ISPRS Journal of Photogrammetry and Remote Sensing* 144: 119–136.

Aplin P 2004. Remote sensing: land cover. *Progress in Physical Geography: Earth and Environment* 28, 2: 283–293. [online]. Available from: http://journals.sagepub.com/doi/10.1191/0309133304pp413pr [Accessed 17 January 2020].

Araujo JA, Abiodun BJ & Crespo O 2014. Impacts of drought on grape yields in Western Cape, South Africa. *Theoretical and Applied Climatology*: 1–14.

Arcidiacono C & Porto SMC 2012. Pixel-based classification of high-resolution satellite images for crop-shelter coverage recognition. *Acta Horticulturae* , 937: 1003–1010. [online]. Available from: https://www.actahort.org/books/937/937_124.htm [Accessed 19 March 2019].

Artigas FJ & Yang J 2006. Spectral discrimination of marsh vegetation types in the New Jersey Meadowlands, USA. *Wetlands* 26, 1: 271. [online]. Available from: https://link.springer.com/article/10.1672/0277-5212(2006)26[271:SDOMVT]2.0.CO;2 [Accessed 22 August 2019].

Arvor D, Jonathan M, Meirelles MSP, Dubreuil V & Durieux L 2011. Classification of MODIS EVI time series for crop mapping in the state of Mato Grosso, Brazil. *International Journal of Remote Sensing* 32, 22: 7847–7871. [online]. Available from: https://www.tandfonline.com/doi/full/10.1080/01431161.2010.531783 [Accessed 25 May 2019].

Atkinson PM & Tatnall ARL 1997. Introduction Neural networks in remote sensing. *International Journal of Remote Sensing* 18, 4: 699–709.

Atzberger C 2013. Advances in Remote Sensing of Agriculture: Context Description, Existing Operational Monitoring Systems and Major Information Needs. *Remote Sensing* 5, 2: 949–

981. [online]. Available from: http://www.mdpi.com/2072-4292/5/2/949 [Accessed 30 January 2019].

Bannari A, Morin D, Bonn F & Huete AR 1995. A review of vegetation indices. *Remote Sensing Reviews* 13, 1–2: 95–120. [online]. Available from: http://www.tandfonline.com/doi/abs/10.1080/02757259509532298 [Accessed 23 May 2019].

Belgiu M & Csillik O 2018. Sentinel-2 cropland mapping using pixel-based and object-based time-weighted dynamic time warping analysis. *Remote Sensing of Environment* 204: 509–523. [online]. Available from: https://www.sciencedirect.com/science/article/pii/S0034425717304686 [Accessed 20 March 2019].

Belgiu M & Drăguţ L 2016. Random forest in remote sensing: A review of applications and future directions. *ISPRS Journal of Photogrammetry and Remote Sensing* 114: 24–31. [online]. Available from: https://www.sciencedirect.com/science/article/pii/S0924271616000265 [Accessed 21 May 2019].

Beucher S 1992. *The Watershed Transformation Applied To Image Segmentation*. [online]. Available from: https://www.researchgate.net/publication/2407235 [Accessed 14 May 2019].

Blanco I, Loisi RV, Sica C, Schettini E & Vox G 2018. Agricultural plastic waste mapping using GIS. A case study in Italy. *Resources, Conservation and Recycling* 137: 229–242. [online]. Available from: https://www.sciencedirect.com/science/article/pii/S0921344918302143 [Accessed 21 March 2019].

Blaschke T 2010. Object based image analysis for remote sensing. *ISPRS Journal of Photogrammetry and Remote Sensing* 65, 1: 2–16. [online]. Available from: https://www.sciencedirect.com/science/article/pii/S0924271609000884 [Accessed 26 March 2019].

Borgogno-Mondino E, Palma L de & Novello V 2020. Investigating Sentinel 2 Multispectral Imagery Efficiency in Describing Spectral Response of Vineyards Covered with Plastic Sheets. *Agronomy 2020, Vol. 10, Page 1909* 10, 12: 1909. [online]. Available from: https://www.mdpi.com/2073-4395/10/12/1909/htm [Accessed 17 August 2021].

Bostanci B & Bostanci E 2013. An Evaluation of Classification Algorithms Using Mc Nemar's Test. *Advances in Intelligent Systems and Computing* 201 AISC, VOL. 1: 15–26. [online].

Available from: https://link.springer.com/chapter/10.1007/978-81-322-1038-2_2 [Accessed 2 August 2021].

Boyle SA, Kennedy CM, Torres J, Colman K, Pérez-Estigarribia PE & De La Sancha NU 2014. High-resolution satellite imagery is an important yet underutilized resource in conservation biology. *PLoS ONE* 9, 1: 86908. [online]. Available from: /pmc/articles/PMC3900690/ [Accessed 31 May 2021].

Briassoulis D, Mistriotis A & Eleftherakis D 2007. Mechanical behaviour and properties of agricultural nets-Part I: Testing methods for agricultural nets. *Elsevier* 26, 6: 822–832. [online]. Available from: www.elsevier.com/locate/polytest [Accessed 29 January 2019].

Bryan E, Deressa TT, Gbetibouo GA & Ringler C 2009. Adaptation to climate change in Ethiopia and South Africa: options and constraints. *Elsevier* 12, 4: 413–426. [online]. Available from: www.elsevier.com/locate/envsci [Accessed 29 January 2019].

Campbell JB & Wynne RH 2011. *Introduction to remote sensing*. Guilford Press. [online]. Available from: https://www.guilford.com/books/Introduction-to-Remote-Sensing/Campbell-Wynne/9781609181765/reviews [Accessed 11 February 2019].

Campos-Taberner, García-Haro, Martínez, Sánchez-Ruiz & Gilabert 2019. A Copernicus Sentinel-1 and Sentinel-2 Classification Framework for the 2020+ European Common Agricultural Policy: A Case Study in València (Spain). *Agronomy* 9, 9: 556. [online]. Available from: https://www.mdpi.com/2073-4395/9/9/556 [Accessed 18 March 2021].

Carfagna E & Gallego FJ 2006. Using Remote Sensing for Agricultural Statistics. *International Statistical Review* 73, 3: 389–404. [online]. Available from: http://doi.wiley.com/10.1111/j.1751-5823.2005.tb00155.x [Accessed 31 May 2019].

Carleer AP, Debeir O & Wolff E 2005. Assessment of Very High Spatial Resolution Satellite Image Segmentations. *Photogrammetric Engineering & Remote Sensing* 71, 11: 1285–1294. [online]. Available from: http://openurl.ingenta.com/content/xref?genre=article&issn=0099-1112&volume=71&issue=11&spage=1285 [Accessed 28 March 2019].

Carrao H, Sarmento P, Araujo A & Caetano M 2007. *Separability analysis of land cover classes at regional scale: A comparitive study of MERIS and MODIS data*. Envisat Symposium 2007.

Carvajal F, Agüera F, Aguilar FJ & Aguilar MA 2010. Relationship between atmospheric corrections and training-site strategy with respect to accuracy of greenhouse detection

process from very high resolution imagery. *International Journal of Remote Sensing* 31, 11: 2977–2994. [online]. Available from: https://www.tandfonline.com/doi/full/10.1080/01431160902946580 [Accessed 19 March 2019].

Carvajal F, Crisanto E, Aguilar FJ, Aguera F & Aguilar MA 2006. *Greenhouse detection using an artificial neural network with a very high resolution satellite image*. [online]. Available from: http://www.isprs.org/proceedings/XXXVI/part2/pdf/carvajal.pdf [Accessed 13 February 2019].

Castellano S, Candura A & Scarascia Mugnozza G 2008. Relationship Between Solidity Ratio, Colour and Shading Effect of Agricultural Nets. *Acta Horticulturae* , 801: 253–258. [online]. Available from: https://www.actahort.org/books/801/801_24.htm [Accessed 9 March 2019].

Castellano S, Russo G & Mugnozza GS 2006. The influence of construction paramaters on radiometric performance of agricultural nets. *Acta Horticulturae* , 718: 283–290. [online]. Available from: https://www.actahort.org/books/718/718_32.htm [Accessed 19 February 2019].

Castellano S, Scarascia-Mugnozza G, Russo G, Briassoulis D, Mistriotis A, Hemming S & Waaijenberg D 2008. Plastic Nets in Agriculture: A General Review of Types and Applications. *Applied Engineering in Agriculture* 24, 6: 799–808. [online]. Available from: https://www.researchgate.net/publication/40800639 [Accessed 11 February 2019].

Chaofan W, Jinsong D, Ke W, Ligang M & Tahmassebi ARS 2016. Object-based classification approach for greenhouse mapping using Landsat-8 imagery. *International Journal of Agricultural and Biological Engineering* 9, 1: 79–88. [online]. Available from: http://www.ijabe.org/index.php/ijabe/article/view/1414 [Accessed 14 May 2019].

Clevers J & Gitelson A 2012. Using the red-edge bands on Sentinel-2 for retrieving canopy chlorophyll and nitrogen content. *Journal of Geosience Remote Sensing*.

Cohen J 1960. A coefficient of agreement for nominal scales. *Educational and psycological journal* 20, 1. [online]. Available from: https://journals.sagepub.com/doi/pdf/10.1177/001316446002000104 [Accessed 31 May 2019].

Congalton RG 1991. A review of assessing the accuracy of classifications of remotely sensed data. *Remote Sensing of Environment* 37, 1: 35–46. [online]. Available from: https://www.sciencedirect.com/science/article/pii/003442579190048B [Accessed 15 May

2019].

Congalton RG & Green K 2009. *Assessing the accuracy of remotely sensed data : principles and practices*.

Cowling RM, Rundel PW, Lamont BB, Kalin Arroyo M & Arianoutsou M 1996. Plant diversity in mediterranean-climate regions. *Trends in Ecology & Evolution* 11, 9: 362–366. [online]. Available from: https://www.sciencedirect.com/science/article/pii/0169534796100446 [Accessed 31 March 2019].

Cremers D, Sochen N & Schnörr C 2006. A Multiphase Dynamic Labeling Model for Variational Recognition-driven Image Segmentation. *International Journal of Computer Vision* 66, 1: 67–81. [online]. Available from: http://link.springer.com/10.1007/s11263-005-3676-z [Accessed 14 May 2019].

Curran PJ & Williamson HD 1985. The accuracy of ground data used in remote-sensing investigations. *International Journal of Remote Sensing* 6, 10: 1637–1651. [online]. Available from: https://www.tandfonline.com/doi/full/10.1080/01431168508948311 [Accessed 30 May 2019].

Curran PJ & Williamson HD 1986. Sample size for ground and remotely sensed data. *Remote Sensing of Environment* 20, 1: 31–41. [online]. Available from: http://www.sciencedirect.com/science/article/pii/003442578690012X

Dabboor M, Howell S, Shokr M & Yackel J 2014. The Jeffries–Matusita distance for the case of complex Wishart distribution as a separability criterion for fully polarimetric SAR data. *International Journal of Remote Sensing* 35, 19: 6859–6873.

Darnell RL, Stutte GW, Martin GC, Lang GA & Early ]. D. 1992. Developmental Physiology of Rabbiteye Blueberry. In *Horticultural Reviews*, 339–405. John Wiley & Sons, Inc. [online]. Available from: https://onlinelibrary.wiley.com/doi/full/10.1002/9780470650509.ch9 [Accessed 16 June 2021].

Darst BF, Malecki KC & Engelman CD 2018. Using recursive feature elimination in random forest to account for correlated variables in high dimensional data. *BMC Genetics* 19, 1: 1–6. [online]. Available from: https://link.springer.com/articles/10.1186/s12863-018-0633-8 [Accessed 1 June 2021].

Darwish A, Leukert K & Reinhardt W 2003. *Image segmentation for the purpose of object-based classification*. IGARSS 2003. 2003 IEEE International Geoscience and Remote Sensing Symposium. Proceedings (IEEE Cat. No.03CH37477). IEEE.: 2039–2041. [online].

Available from: http://ieeexplore.ieee.org/document/1294332/ [Accessed 14 May 2019].

DEADP 2011. *Western Cape integrated water resources management plan*.

Debba P, Cho MA & Mathieu R 2009. *Within- and between-class variability of spectrally similar tree species*. International Geoscience and Remote Sensing Symposium (IGARSS).

Dey V, Zhang Y & Zhong M 2010. *A review on image segmentation techniques with remote sensing perspective*. ISPRS Symposium. Vienna, Austria. [online]. Available from: https://pdfs.semanticscholar.org/72ea/0209ea48769cbda2863c4295cafdaeac41d1.pdf [Accessed 14 May 2019].

Drăguţ L, Tiede D & Levick SR 2010. ESP: a tool to estimate scale parameter for multiresolution image segmentation of remotely sensed data. *International Journal of Geographical Information Science* 24, 6: 859–871. [online]. Available from: http://www.tandfonline.com/doi/abs/10.1080/13658810903174803 [Accessed 15 May 2019].

Drusch M, Del Bello U, Carlier S, Colin O, Fernandez V, Gascon F, Hoersch B, Isola C, Laberinti P, Martimort P, Meygret A, Spoto F, Sy O, Marchese F & Bargellini P 2012. Sentinel-2: ESA's Optical High-Resolution Mission for GMES Operational Services. *Remote Sensing of Environment* 120: 25–36. [online]. Available from: https://www.sciencedirect.com/science/article/pii/S0034425712000636 [Accessed 9 May 2019].

Du CJ & Sun DW 2008. Object Classification Methods. *Computer Vision Technology for Food Quality Evaluation*: 81–107.

Dudley KL, Dennison PE, Roth KL, Roberts DA & Coates AR 2015. A multi-temporal spectral library approach for mapping vegetation species across spatial and temporal phenological gradients. *Remote Sensing of Environment* 167: 121–134.

ESA 2018. Open Access Hub [online]. Available from: https://scihub.copernicus.eu/ [Accessed 22 August 2018].

Espí E, Salmerón A, Fontecha A, García Y & Real AI 2006. Plastic Films for Agricultural Applications. *Journal of Plastic Film & Sheeting* 22, 2: 85–102. [online]. Available from: http://journals.sagepub.com/doi/10.1177/8756087906064220 [Accessed 10 March 2019].

Espindola GM, Camara G, Reis IA, Bins LS & Monteiro AM 2006. Parameter selection for region-growing image segmentation algorithms using spatial autocorrelation. *International Journal of Remote Sensing* 27, 14: 3035–3040. [online]. Available from:

https://www.tandfonline.com/doi/full/10.1080/01431160600617194 [Accessed 14 May 2019].

Fitzgerald RW & Lees BG 1994. Assessing the classification accuracy of multisource remote sensing data. *Remote Sensing of Environment* 47, 3: 362–368. [online]. Available from: https://linkinghub.elsevier.com/retrieve/pii/0034425794901031 [Accessed 31 May 2019].

Fitzpatrick-Lins K 1981. Comparison of sampling procedures and data analysis for land-use and land-cover map. *Photogrammetric Engineering & Remote Sensing* 47: 343–351.

Foody GM 2002. Status of land cover classification accuracy assessment. *Remote Sensing of Environment* 80, 1: 185–201. [online]. Available from: http://www.sciencedirect.com/science/article/pii/S0034425701002954

Georganos S, Grippa T, Vanhuysse S, Lennert M, Shimoni M, Kalogirou S & Wolff E 2018. Less is more: optimizing classification performance through feature selection in a very-high-resolution remote sensing object-based urban application. *GIScience and Remote Sensing* 55, 2: 221–242. [online]. Available from: https://www.tandfonline.com/doi/abs/10.1080/15481603.2017.1408892 [Accessed 1 June 2021].

Gibson PJ (Paul J & Power CH 2000. *Introductory remote sensing : principles and concepts*.

González-Yebra Ó, Aguilar MA, Nemmaoui A & Aguilar FJ 2018. Methodological proposal to assess plastic greenhouses land cover change from the combination of archival aerial orthoimages and Landsat data. *Biosystems Engineering* 175: 36–51. [online]. Available from: https://www.sciencedirect.com/science/article/pii/S1537511018305129 [Accessed 15 February 2019].

GreenAgri 2016. *A Status Quo Review of Climate Change and the Agricultural Sector of the Western Cape Province*.

Guerschman JP, Paruelo JM, Di Bella C, Giallorenzi MC & Pacin F 2003. Land cover classification in the Argentine Pampas using multi-temporal Landsat TM data. *International Journal of Remote Sensing* 24, 17: 3381–3402.

Gunal S & Edizkan R 2008. Subspace based feature selection for pattern recognition. *Information Sciences* 178, 19: 3716–3726. [online]. Available from: https://www.sciencedirect.com/science/article/pii/S0020025508001850 [Accessed 20 August 2019].

Guyon I & Elisseeff A 2003. An Introduction to Variable and Feature Selection. *Journal of*

*Machine Learning Research* 3: 1157–1182.

Haralick RM, Shanmugam K & Dinstein I 1973. Textural Features for Image Classification. *IEEE Transactions on Systems, Man, and Cybernetics* SMC-3, 6: 610–621. [online]. Available from: http://ieeexplore.ieee.org/document/4309314/ [Accessed 26 May 2019].

Hasituya & Chen Z 2017. Mapping Plastic-Mulched Farmland with Multi-Temporal Landsat-8 Data. *Remote Sensing* 9, 6.

Hasituya, Chen Z, Li F, Hongmei, Hasituya, Chen Z, Li F & Hongmei 2017. Mapping Plastic-Mulched Farmland with C-Band Full Polarization SAR Remote Sensing Data. *Remote Sensing* 9, 12: 1264. [online]. Available from: http://www.mdpi.com/2072-4292/9/12/1264 [Accessed 25 October 2018].

Hasituya, Chen Z, Wang L, Wu W, Jiang Z & Li H 2016. Monitoring Plastic-Mulched Farmland by Landsat-8 OLI Imagery Using Spectral and Textural Features. *Remote Sensing* 8, 4.

Hemming Silke, Castellano S, Russo Giovanni, Hemming S, Swinkels GLAM, Russo G & Scarascia-Mugnozza G 2008. *Numerical Model to estimate the Radiometric Performance of Net Covered Structures Physical Characteristics of Nets for Agricultural Use View project Numerical Model to estimate the Radiometric Performance of Net Covered Structures*. [online]. Available from: https://www.researchgate.net/publication/242177967 [Accessed 10 March 2019].

Herold M, Gardner ME & Roberts DA 2003. Spectral resolution requirements for mapping urban areas. *IEEE Transactions on Geoscience and Remote Sensing* 41, 9 PART I: 1907–1919.

Hörig B, Kühn F, Oschütz F & Lehmann F 2001. HyMap hyperspectral remote sensing to detect hydrocarbons. *International Journal of Remote Sensing* 22, 8: 1413–1422. [online]. Available from: https://www.tandfonline.com/doi/full/10.1080/01431160120909 [Accessed 12 February 2019].

Horing N 2010. *Random Forests : An algorithm for image classification and generation of continuous fields data sets*. International Conference on Geoinformatics for Spatial Infrastructure Development in Earth and Allied Sciences.

Horler DNH, Dockray M & Barber J 1983. The red edge of plant leaf reflectance. *International Journal of Remote Sensing* 4, 2: 273–288. [online]. Available from: https://www.tandfonline.com/doi/full/10.1080/01431168308948546 [Accessed 25 March 2019].

Howden SM, Soussana J-F, Tubiello FN, Chhetri N, Dunlop M & Meinke H 2007. Adapting

agriculture to climate change. *Proceedings of the National Academy of Sciences of the United States of America* 104, 50: 19691–6. [online]. Available from: http://www.ncbi.nlm.nih.gov/pubmed/18077402 [Accessed 28 February 2019].

Hu Q, Wu W, Song Q, Lu M, Chen D, Yu Q-Y & Tang H 2017. How do temporal and spectral features matter in crop classification in Heilongjiang Province, China? *Journal of Integrative Agriculture* 16, 2: 324–336.

Huang C, Davis LS & Townshend JRG 2002. An assessment of support vector machines for land cover classification. *International Journal of Remote Sensing* 23, 4: 725–749. [online]. Available from: https://www.tandfonline.com/doi/full/10.1080/01431160110040323 [Accessed 31 May 2019].

Huete A. 1988. A soil-adjusted vegetation index (SAVI). *Remote Sensing of Environment* 25, 3: 295–309. [online]. Available from: https://www.sciencedirect.com/science/article/abs/pii/003442578890106X [Accessed 24 May 2019].

Hughes G 1968. On the mean accuracy of statistical pattern recognizers. *IEEE Transactions on Information Theory* 14, 1: 55–63. [online]. Available from: http://ieeexplore.ieee.org/document/1054102/ [Accessed 24 May 2019].

Ihuoma SO & Madramootoo CA 2019. Crop reflectance indices for mapping water stress in greenhouse grown bell pepper. *Agricultural Water Management* 219: 49–58.

Immitzer M, Vuolo F, Atzberger C, Immitzer M, Vuolo F & Atzberger C 2016. First Experience with Sentinel-2 Data for Crop and Tree Species Classifications in Central Europe. *Remote Sensing* 8, 3: 166. [online]. Available from: http://www.mdpi.com/2072-4292/8/3/166 [Accessed 20 March 2019].

Janssen F & Van der Wel FJ 1994. Accuracy Assessment of Satellite Derived Land-Gover Data: A Review. *Photogrammetric Engineering & Remote Sensing* 60, 4: 479–426. [online]. Available from: https://www.asprs.org/wp-content/uploads/pers/1994journal/apr/1994_apr_419-426.pdf [Accessed 31 May 2019].

Jensen JR 1996. *Introductory Digital Image Processing: A Remote Sensing Perspective*.

Jensen JR 2016. *Introductory Digital Image Processing: A Remote Sensing Perspective, 4th Edition | Pearson*. 4th ed. Pearson (ed). Brigham Young University. [online]. Available from: https://www.pearson.com/us/higher-education/program/Jensen-Introductory-Digital-Image-Processing-A-Remote-Sensing-Perspective-4th-Edition/PGM30020.html [Accessed

6 May 2019].

Jensen JR 2005. *Introductory digital image processing : a remote sensing perspective*. Prentice Hall.

Jensen M & Malter A 1995. *Protected Agriculture: A Global Review*. Washington: The World Bank. [online]. Available from: https://www.researchgate.net/publication/5078125_Protected_Agriculture_A_Global_Review [Accessed 11 February 2019].

Jia K, Liang S, Wei X, Yao Y, Su Y, Jiang B, Wang X, Jia K, Liang S, Wei X, Yao Y, Su Y, Jiang B & Wang X 2014. Land Cover Classification of Landsat Data with Phenological Features Extracted from Time Series MODIS NDVI Data. *Remote Sensing* 6, 11: 11518–11532. [online]. Available from: http://www.mdpi.com/2072-4292/6/11/11518 [Accessed 24 May 2019].

Jones MR, Singels A & Ruane AC 2015. Simulated impacts of climate change on water use and yield of irrigated sugarcane in South Africa. *AGSY* 139: 260–270. [online]. Available from: http://dx.doi.org/10.1016/j.agsy.2015.07.007 [Accessed 29 January 2019].

Julesz B 1962. Visual Pattern Discrimination. *IRE Transactions on Information Theory* 8, 2: 84–92.

Kaufman YJ, Tanré D, Gordon HR, Nakajima T, Lenoble J, Frouin R, Grassl H, Herman BM, King MD & Teillet PM 1997. Passive remote sensing of tropospheric aerosol and atmospheric correction for the aerosol effect. *Journal of Geophysical Research: Atmospheres* 102, D14: 16815–16830. [online]. Available from: http://doi.wiley.com/10.1029/97JD01496 [Accessed 3 May 2019].

Kaufman YJ & Tanre D 1992. Atmospherically resistant vegetation index (ARVI) for EOS-MODIS. *IEEE Transactions on Geoscience and Remote Sensing* 30, 2: 261–270. [online]. Available from: http://ieeexplore.ieee.org/document/134076/ [Accessed 24 May 2019].

Kavzoglu T & Colkesen I 2009. A kernel functions analysis for support vector machines for land cover classification. *International Journal of Applied Earth Observation and Geoinformation* 11, 5: 352–359. [online]. Available from: https://www.sciencedirect.com/science/article/pii/S0303243409000464 [Accessed 21 May 2019].

Ketsdever A 2014. *Introduction to Remote Sensing*. [online]. Available from: https://www.slideserve.com/bruis/lesson-7-remote-sensing [Accessed 3 May 2019].

Khalid S, Khalil T & Nasreen S 2014. *A survey of feature selection and feature extraction techniques in machine learning*. Proceedings of 2014 Science and Information Conference, SAI 2014. Institute of Electrical and Electronics Engineers Inc.: 372–378.

Knitex 2020. Climate control shade net [online]. Available from: https://www.knittex.co.za/knittex-spectranet.html

Kramer HJ 2002. *Observation of the Earth and Its Environment: Survey of Missions and Sensors*. 4th ed. Springer Verlag. [online]. Available from: https://www.satimagingcorp.com/satellite-sensors/other-satellite-sensors/sentinel-2a/ [Accessed 8 May 2019].

Kühn F, Oppermann K & Hörig B 2004. Hydrocarbon Index – an algorithm for hyperspectral detection of hydrocarbons. *International Journal of Remote Sensing* 25, 12: 2467–2473. [online]. Available from: https://www.tandfonline.com/doi/full/10.1080/01431160310001642287 [Accessed 12 February 2019].

Kuhn M 2015. caret: Classification and Regression Training. *ascl*: ascl:1505.003. [online]. Available from: https://ui.adsabs.harvard.edu/abs/2015ascl.soft05003K/abstract [Accessed 5 June 2021].

Kuplich TM 2001. Temporal, spatial, spectral and polarisation characteristics of the SAR backscatter from regenerating tropical forests.

Lanorte A, De Santis F, Nolè G, Blanco I, Loisi RV, Schettini E & Vox G 2017. Agricultural plastic waste spatial estimation by Landsat 8 satellite images. *Computers and Electronics in Agriculture* 141: 35–45. [online]. Available from: https://www.sciencedirect.com/science/article/pii/S0168169917302259 [Accessed 19 March 2019].

Lary DJ, Alavi AH, Gandomi AH & Walker AL 2016. Machine learning in geosciences and remote sensing. *Geoscience Frontiers* 7, 1: 3–10.

Lautenbacher CC 2006. The Global Earth Observation System of Systems: Science Serving Society. *Space Policy* 22, 1: 8–11. [online]. Available from: https://www.sciencedirect.com/science/article/pii/S0265964605001220 [Accessed 15 March 2019].

Lefebvre A, Sannier C, Corpetti T, Lefebvre A, Sannier C & Corpetti T 2016. Monitoring Urban Areas with Sentinel-2A Data: Application to the Update of the Copernicus High Resolution

Layer Imperviousness Degree. *Remote Sensing* 8, 7: 606. [online]. Available from: http://www.mdpi.com/2072-4292/8/7/606 [Accessed 20 March 2019].

Levin N, Lugassi R, Ramon U, Braun O & Ben-Dor E 2007. Remote sensing as a tool for monitoring plasticulture in agricultural landscapes. *International Journal of Remote Sensing* 28, 1: 183–202.

Levin N, Lugassi R, Ramon U, Braun O, Ben-Dor E, Lugassi{ R, Ramon{ U & Ben-Dor{ E 2010. Remote sensing as a tool for monitoring plasticulture in agricultural landscapes Remote sensing as a tool for monitoring plasticulture in agricultural landscapes. *Remote Sensing* 28, 1: 183–202. [online]. Available from: https://www.tandfonline.com/action/journalInformation?journalCode=tres20 [Accessed 12 February 2019].

Li C, Wang J, Wang L, Hu L & Gong P 2014. Comparison of Classification Algorithms and Training Sample Sizes in Urban Land Classification with Landsat Thematic Mapper Imagery. *Remote Sensing* 6, 2: 964–983. [online]. Available from: https://www.mdpi.com/2072-4292/6/2/964

Li G, Lu D, Moran E & Sant'Anna SJS 2012. Comparative analysis of classification algorithms and multiple sensor data for land use/land cover classification in the Brazilian Amazon. *Journal of Applied Remote Sensing* 6, 1: 061706. [online]. Available from: http://remotesensing.spiedigitallibrary.org/article.aspx?doi=10.1117/1.JRS.6.061706 [Accessed 26 May 2019].

Li M, Zang S, Zhang B, Li S & Wu C 2014. A Review of Remote Sensing Image Classification Techniques: the Role of Spatio-contextual Information. *European Journal of Remote Sensing* 47, 1: 389–411. [online]. Available from: https://www.tandfonline.com/doi/full/10.5721/EuJRS20144723 [Accessed 21 May 2019].

Liang L 2019. *Reference Module in Earth Systems and Environmental Sciences*.

Liang S, Li X & Wang J 2012. *Advanced Remote Sensing*. Elsevier. [online]. Available from: https://linkinghub.elsevier.com/retrieve/pii/C20100673044 [Accessed 4 May 2019].

Lillesand TM, Kiefer RW & Chipman JW 1994. *Remote sensing and image interpretation*. New York: John Wiley and Sons Inc. [online]. Available from: https://www.wiley.com/en-us/Remote+Sensing+and+Image+Interpretation%2C+7th+Edition-p-9781118343289 [Accessed 7 May 2019].

Lim S 2002. *Indicators for agricultural landscapes and policy implications: A Korean*

*perspective*. NIJOS/OECD Expert Meeting on Agricultural Landscape Indicators: 228–241.

Liu BYH & Jordan RC 1960. The interrelationship and characteristic distribution of direct, diffuse and total solar radiation. *Solar Energy* 4, 3: 1–19. [online]. Available from: https://www.sciencedirect.com/science/article/pii/0038092X60900621 [Accessed 11 March 2019].

Liu H & Huete A 1995. A feedback based modification of the NDVI to minimize canopy background and atmospheric noise. *IEEE Transactions on Geoscience and Remote Sensing* 33, 2: 457–465. [online]. Available from: http://ieeexplore.ieee.org/document/377946/ [Accessed 25 May 2019].

Lu D & Weng Q 2007. A survey of image classification methods and techniques for improving classification performance. *International Journal of Remote Sensing* 28, 5: 823–870. [online]. Available from: https://doi.org/10.1080/01431160600746456

Lu L, Di L & Ye Y 2014. A Decision-Tree Classifier for Extracting Transparent Plastic-Mulched Landcover from Landsat-5 TM Images. *IEEE Journal of Selected Topics in Applied Earth Observations and Remote Sensing* 7, 11: 4548–4558. [online]. Available from: http://ieeexplore.ieee.org/document/6837479/ [Accessed 21 May 2019].

Lu L, Tao Y & Di L 2018. Object-Based Plastic-Mulched Landcover Extraction Using Integrated Sentinel-1 and Sentinel-2 Data. *Remote Sensing* 10, 11.

Luque A, Carrasco A, Martín A & de las Heras A 2019. The impact of class imbalance in classification performance metrics based on the binary confusion matrix. *Pattern Recognition* 91: 216–231.

Ma L, Fu T, Blaschke T, Li M, Tiede D, Zhou Z, Ma X & Chen D 2017. Evaluation of feature selection methods for object-based land cover mapping of unmanned aerial vehicle imagery using random forest and support vector machine classifiers. *ISPRS International Journal of Geo-Information* 6, 2: 51. [online]. Available from: www.mdpi.com/journal/ijgi [Accessed 31 May 2021].

Ma L, Liu Y, Zhang X, Ye Y, Yin G & Johnson BA 2019. Deep learning in remote sensing applications: A meta-analysis and review. *ISPRS Journal of Photogrammetry and Remote Sensing* 152: 166–177.

Main-Knorn M, Pflug B, Louis J, Debaecker V, Müller-Wilm U & Gascon F 2017. Sen2Cor for Sentinel-2. 10427: 1042704. [online]. Available from: https://www.spiedigitallibrary.org/conference-proceedings-of-

spie/10427/1042704/Sen2Cor-for-Sentinel-2/10.1117/12.2278218.full [Accessed 27 July 2021].

Manandhar R, Odeh I, Ancev T, Manandhar R, Odeh IOA & Ancev T 2009. Improving the Accuracy of Land Use and Land Cover Classification of Landsat Data Using Post-Classification Enhancement. *Remote Sensing* 1, 3: 330–344. [online]. Available from: http://www.mdpi.com/2072-4292/1/3/330 [Accessed 31 May 2019].

Maponya MG, Van Niekerk A & Mashimbye ZE 2020. Pre-harvest classification of crop types using a Sentinel-2 time-series and machine learning. *Computers and Electronics in Agriculture* 169: 105164.

Mas JF & Flores JJ 2008. The application of artificial neural networks to the analysis of remotely sensed data. *International Journal of Remote Sensing* 29, 3: 617–663.

Matongera TN, Mutanga O, Dube T & Sibanda M 2017. Detection and mapping the spatial distribution of bracken fern weeds using the Landsat 8 OLI new generation sensor. *International Journal of Applied Earth Observation and Geoinformation* 57: 93–103.

Matsei E 2016. *Economic Review of SA Agriculture*. ISBN: 978-0-621-45887-9. [online]. Available from: https://www.daff.gov.za/Daffweb3/Portals/0/Statistics and Economic Analysis/Economic Analysis/Economic Review 2016_17.pdf [Accessed 29 January 2019].

Maxwell AE, Warner TA & Fang F 2018. Implementation of machine-learning classification in remote sensing: An applied review. *International Journal of Remote Sensing* 39, 9: 2784–2817. [online]. Available from: https://www.tandfonline.com/action/journalInformation?journalCode=tres20 [Accessed 5 June 2021].

McKeown DM, Cochran SD, Ford SJ, McGlone JC, Shufelt JA & Yocum DA 1999. Fusion of HYDICE hyperspectral data with panchromatic imagery for cartographic feature extraction. *IEEE Transactions on Geoscience and Remote Sensing* 37, 3: 1261–1277. [online]. Available from: http://ieeexplore.ieee.org/document/763286/ [Accessed 13 August 2019].

McNemar Q 1974. Correction to a correction. *Journal of Consulting and Clinical Psychology* 42, 1: 145–146. [online]. Available from: https://psycnet.apa.org/journals/ccp/42/1/145 [Accessed 2 August 2021].

Millard K & Richardson M 2015. On the Importance of Training Data Sample Selection in Random Forest Image Classification: A Case Study in Peatland Ecosystem Mapping. *Remote Sensing* 7, 7: 8489–8515. [online]. Available from: https://www.mdpi.com/2072-

4292/7/7/8489

Mishra VN, Rai P, Kumar P & Prasad R 2012. A Review of Optical Imagery and Airborne LiDAR Data Registration Methods. *The Open Remote Sensing Journal* 5, 1: 54–63. [online]. Available from: http://benthamopen.com/ABSTRACT/TORMSJ-5-54 [Accessed 7 May 2019].

Morisette JT, Privette JL & Justice CO 2002. A framework for the validation of MODIS Land products. *Remote Sensing of Environment* 83, 1–2: 77–96. [online]. Available from: https://linkinghub.elsevier.com/retrieve/pii/S0034425702000883 [Accessed 6 May 2019].

Mountrakis G, Im J & Ogole C 2011. Support vector machines in remote sensing: A review. *ISPRS Journal of Photogrammetry and Remote Sensing* 66, 3: 247–259. [online]. Available from: https://www.sciencedirect.com/science/article/pii/S0924271610001140 [Accessed 21 May 2019].

Mtshiselwa Z 2020. Trends and determinants of competitiveness in the South African table grape industry.

Mulla DJ 2013. Twenty five years of remote sensing in precision agriculture: Key advances and remaining knowledge gaps. *Biosystems Engineering* 114, 4: 358–371. [online]. Available from: https://www.sciencedirect.com/science/article/pii/S1537511012001419 [Accessed 4 March 2019].

Mutanga O, Adam E & Cho MA 2012. High density biomass estimation for wetland vegetation using WorldView-2 imagery and random forest regression algorithm. *International Journal of Applied Earth Observation and Geoinformation* 18: 399–406. [online]. Available from: https://www.sciencedirect.com/science/article/pii/S0303243412000566 [Accessed 8 May 2019].

Mutanga O & Kumar L 2019. Google Earth Engine Applications. *Remote Sensing* 11, 5: 591. [online]. Available from: https://www.mdpi.com/2072-4292/11/5/591 [Accessed 20 January 2020].

Nair M & Bindhu J 2016. *Supervised Techniques and Approaches for Satellite Image Classification*. 16.*International Journal of Computer Applications* 134 [online]. Available from: http://citeseerx.ist.psu.edu/viewdoc/download?doi=10.1.1.735.6733&rep=rep1&type=pdf [Accessed 27 May 2019].

Ngubane NP 2018. Blueberries, Distribution of pests of Re-description, in South Africa and Bud,

and behaviour of the blueberry (Eriophyidae), mite Acalitus vaccinii.

Van Niekerk A, Jarmien C, Goudriaan R, Muller S, Ferreira F, Munch Z, Pauw T, Stephenson G & Gibso L 2018. *An earth observation approach towards mapping irrigated areas and quantifying water use by irrigated crops in South Africa*.

Van Niekerk A & Joubert SJ 2011. Input variable selection for interpolating high-resolution climate surfaces for the western cape. *Water SA* 37, 3: 271–280. [online]. Available from: http://www.wrc.org.za [Accessed 16 June 2021].

Novelli A, Aguilar MA, Nemmaoui A, Aguilar FJ & Tarantino E 2016. Performance evaluation of object based greenhouse detection from Sentinel-2 MSI and Landsat 8 OLI data: A case study from Almería (Spain). *International Journal of Applied Earth Observations and Geoinformation* 52: 403–411. [online]. Available from: http://dx.doi.org/10.1016/j.jag.2016.07.011 [Accessed 11 February 2019].

Novelli A & Tarantino E 2015. Combining ad hoc spectral indices based on LANDSAT-8 OLI/TIRS sensor data for the detection of plastic cover vineyard. *Remote Sensing Letters* 6, 12: 933–941. [online]. Available from: http://www.tandfonline.com/doi/full/10.1080/2150704X.2015.1093186 [Accessed 19 March 2019].

Olaode A, Naghdy GA, Todd C & Naghdy G 2014. Unsupervised Classification of Images: A Review Biometric gait, motion and fall risk analysis in older people View project Image Retrieval View project Unsupervised Classification of Images: A Review. *International Journal of Image Processing (IJIP)* , 8: 325. [online]. Available from: https://www.researchgate.net/publication/265729668 [Accessed 28 October 2021].

Pahlefi MR, Danoedoro P & Kamal M 2021. The utilisation of sentinel-2A images and google earth engine for monitoring tropical Savannah grassland. *https://doi.org/10.1080/10106049.2021.1914749*. [online]. Available from: https://www.tandfonline.com/doi/abs/10.1080/10106049.2021.1914749 [Accessed 27 July 2021].

Pal M & Mather PM 2003. An assessment of the effectiveness of decision tree methods for land cover classification. *Remote Sensing of Environment* 86, 4: 554–565. [online]. Available from: https://www.sciencedirect.com/science/article/pii/S0034425703001329 [Accessed 27 May 2019].

Panda SS, Ames DP, Panigrahi S, Panda SS, Ames DP & Panigrahi S 2010. Application of Vegetation Indices for Agricultural Crop Yield Prediction Using Neural Network

Techniques. *Remote Sensing* 2, 3: 673–696. [online]. Available from: http://www.mdpi.com/2072-4292/2/3/673 [Accessed 24 May 2019].

Pandit S, Tsuyuki S & Dube T 2020. Exploring the inclusion of Sentinel-2 MSI texture metrics in above-ground biomass estimation in the community forest of Nepal. *Geocarto International* 35, 16: 1832–1849.

Pembury Smith MQR & Ruxton GD 2020. Effective use of the McNemar test. *Behavioral Ecology and Sociobiology* 74.

Perilla G. & Mas J 2019. High-resolution mapping of protected agriculture in Mexico, through remote sensing data cloud geoprocessing. *European Journal of Remote Sensing* 52, 1: 532–54.

Pesaresi M, Corbane C, Julea A, Florczyk A, Syrris V, Soille P, Pesaresi M, Corbane C, Julea A, Florczyk AJ, Syrris V & Soille P 2016. Assessment of the Added-Value of Sentinel-2 for Detecting Built-up Areas. *Remote Sensing* 8, 4: 299. [online]. Available from: http://www.mdpi.com/2072-4292/8/4/299 [Accessed 20 March 2019].

Phiri D, Simwanda M, Salekin S, Nyirenda VR, Murayama Y & Ranagalage M 2020. Sentinel-2 data for land cover/use mapping: A review. *Remote Sensing* 12, 14: 2291. [online]. Available from: www.mdpi.com/journal/remotesensing [Accessed 5 June 2021].

Pienaar L 2018. The flyover project: Tracking agricultural land-use changes in the Western Cape from 2013 to 2017. *Elsenburg Journal* 15, 4.

PlasticsSA 2018. *Annual Review*.

Du Plessis A 2017. Water Scarcity and Other Significant Challenges for South Africa. In 119–125. Springer, Cham. [online]. Available from: http://link.springer.com/10.1007/978-3-319-49502-6_7 [Accessed 8 August 2018].

Plourde L & Congalton RG 2003. Sampling Method and Sample Placement. *Photogrammetric Engineering & Remote Sensing* 69, 3: 289–297. [online]. Available from: http://openurl.ingenta.com/content/xref?genre=article&issn=0099-1112&volume=69&issue=3&spage=289 [Accessed 31 May 2019].

Prins AJ & Niekerk A Van 2020. Crop type mapping using LiDAR, Sentinel-2 and aerial imagery with machine learning algorithms. *http://www.tandfonline.com/action/journalInformation?show=aimsScope&journalCode=tgsi20#.VsXpLiCLRhE*: 1–13. [online]. Available from: https://www.tandfonline.com/doi/abs/10.1080/10095020.2020.1782776 [Accessed 1

November 2021].

Qiu B, Fan Z, Zhong M, Tang Z & Chen C 2014. A new approach for crop identification with wavelet variance and JM distance. *Environmental Monitoring and Assessment* 186, 11: 7929–7940.

Richards JA 1993. *Remote Sensing Digital Image Analysis*. Berlin, Heidelberg: Springer Berlin Heidelberg. [online]. Available from: http://link.springer.com/10.1007/978-3-642-30062-2 [Accessed 20 August 2019].

Richards J & Jia X 2006. *Remote Sensing Digital Image Analysis*.

Rodriguez-Galiano VF, Ghimire B, Rogan J, Chica-Olmo M & Rigol-Sanchez JP 2012. An assessment of the effectiveness of a random forest classifier for land-cover classification. *ISPRS Journal of Photogrammetry and Remote Sensing* 67: 93–104. [online]. Available from: https://www.sciencedirect.com/science/article/pii/S0924271611001304 [Accessed 31 May 2019].

Russ JC 1995. *The image processing handbook*. CRC Press. [online]. Available from: https://dl.acm.org/citation.cfm?id=201104 [Accessed 9 May 2019].

Safavian SR & Landgrebe D 1991. A survey of decision tree classifier methodology. *IEEE Transactions on Systems, Man, and Cybernetics* 21, 3: 660–674. [online]. Available from: http://ieeexplore.ieee.org/document/97458/ [Accessed 21 May 2019].

SANBI 2013. *Climate trends and scenarios in South Africa*. [online]. Available from: https://www.sanbi.org/wp-content/uploads/2018/03/ltas-factsheetclimate-trends-and-scenarios2013.pdf [Accessed 21 March 2019].

SATI 2020. *Statistics of Table Grapes in South Africa*.

Scarascia-Mugnozzo G, Sica C & Russo G 2011. Plastic Materials in European agriculture. *Journal of Agricultural Engineering* 3: 15–28. [online]. Available from: https://agroengineering.org/index.php/jae/article/view/jae.2011.3.15/26 [Accessed 9 March 2019].

Schmidt KS & Skidmore AK 2003. Spectral discrimination of vegetation types in a coastal wetland. *Remote Sensing of Environment* 85, 1: 92–108. [online]. Available from: https://www.sciencedirect.com/science/article/pii/S0034425702001967 [Accessed 20 August 2019].

Schober P & Schwarte LA 2018. Correlation coefficients: Appropriate use and interpretation. *Anesthesia and Analgesia* 126, 5: 1763–1768. [online]. Available from:

https://journals.lww.com/anesthesia-analgesia/Fulltext/2018/05000/Correlation_Coefficients__Appropriate_Use_and.50.aspx [Accessed 17 February 2022].

Shahak Y, Gussakovsky EE, Gal E & Ganelevin R 2004. ColorNets: Crop Protection and Light-Quality Manipulation in One Technology. *Acta Horticulturae* , 659: 143–151. [online]. Available from: https://www.actahort.org/books/659/659_17.htm [Accessed 11 March 2019].

Shao Y & Lunetta RS 2012. Comparison of support vector machine, neural network, and CART algorithms for the land-cover classification using limited training data points. *ISPRS Journal of Photogrammetry and Remote Sensing* 70: 78–87.

Shen G & Sarris A 2008. Application of texture analysis in land cover classification of high resolution image. *Proceedings - 5th International Conference on Fuzzy Systems and Knowledge Discovery, FSKD 2008* 3: 513–517.

Sica C & Picuno P 2008a. Spectro-radiometrical characterization of protected nets for protected cultivation. *Acta Horticulturae* , 801: 245–252. [online]. Available from: https://www.actahort.org/books/801/801_23.htm [Accessed 4 March 2019].

Sica C & Picuno P 2008b. Spectro-Radiometrical Characterization of Plastic Nets for Protected Cultivation. *Acta Horticulturae* , 801: 245–252. [online]. Available from: https://www.actahort.org/books/801/801_23.htm [Accessed 10 March 2019].

Smith A 2010. Image segmentation scale parameter optimization and land cover classification using the Random Forest algorithm. *Journal of Spatial Science* 55, 1: 69–79. [online]. Available from: http://www.tandfonline.com/doi/abs/10.1080/14498596.2010.487851 [Accessed 15 May 2019].

Sothe C, de Almeida CM, Liesenberg V & Schimalski MB 2017. Evaluating Sentinel-2 and Landsat-8 data to map sucessional forest stages in a subtropical forest in Southern Brazil. *Remote Sensing* 9, 8: 838. [online]. Available from: www.mdpi.com/journal/remotesensing [Accessed 28 June 2021].

SSA 2017. *Population estimates*. [online]. Available from: www.statssa.gov.zainfo@statssa.gov.za [Accessed 20 March 2019].

Stander J 2015. *The Reproductive Phenology of Citrus III: Morphogenesis from Flower to Fruit*. [online]. Available from: http://www.1stfruits.co.za/wp/wp-content/uploads/2016/02/3-OKT-NOV-citrus-phenology_JS.pdf [Accessed 12 June 2021].

Stromann O, Nascetti A, Yousif O & Ban Y 2019. Dimensionality Reduction and Feature Selection for Object-Based Land Cover Classification based on Sentinel-1 and Sentinel-2 Time Series Using Google Earth Engine. *Remote Sensing 2020, Vol. 12, Page 76* 12, 1: 76. [online]. Available from: https://www.mdpi.com/2072-4292/12/1/76/htm [Accessed 2 August 2021].

Sun H, Wang L, Lin R, Zhang Z & Zhang B 2021. Mapping Plastic Greenhouses with Two-Temporal Sentinel-2 Images and 1D-CNN Deep Learning. *Remote Sensing* 13, 14: 2820. [online]. Available from: https://www.mdpi.com/2072-4292/13/14/2820 [Accessed 1 August 2021].

Syarif I, Prugel-Bennett A & Wills G 2016. SVM Parameter Optimization Using Grid Search and Genetic Algorithm to Improve Classification Performance. *TELKOMNIKA* 14, 4: 1504–1509.

Takakura T & Fang W 2002. *Climate Under Cover*. Springer Netherlands.

Talukdar S, Singha P, Mahato S, Shahfahad, Pal S, Liou Y-A & Rahman A 2020. Land-Use Land-Cover Classification by Machine Learning Classifiers for Satellite Observations—A Review. *Remote Sensing 2020, Vol. 12, Page 1135* 12, 7: 1135. [online]. Available from: https://www.mdpi.com/2072-4292/12/7/1135/htm [Accessed 28 October 2021].

Tarantino E, Figorito B, Tarantino E & Figorito B 2012. Mapping Rural Areas with Widespread Plastic Covered Vineyards Using True Color Aerial Data. *Remote Sensing* 4, 7: 1913–1928. [online]. Available from: http://www.mdpi.com/2072-4292/4/7/1913 [Accessed 12 February 2019].

Tempfli K, Huurneman GC, Bakker WH, Janssen LLF, Feringa WF, Gieske ASM, Grabmaier KA, Hecker CA, Horn JA van der., Kerle N, Meer FD van der, Parodi GN, Pohl C, Reeves CV, Ruitenbeek FJA van, Schetselaar EM, Weir MJC, Westinga E & Woldai T 2009. *Principles of remote sensing : an introductory textbook.* ITC. [online]. Available from: https://research.utwente.nl/en/publications/principles-of-remote-sensing-an-introductory-textbook-4 [Accessed 3 May 2019].

Thanh Noi P, Kappas M, Thanh Noi P & Kappas M 2017. Comparison of Random Forest, k-Nearest Neighbor, and Support Vector Machine Classifiers for Land Cover Classification Using Sentinel-2 Imagery. *Sensors* 18, 2: 18. [online]. Available from: http://www.mdpi.com/1424-8220/18/1/18 [Accessed 27 May 2019].

Tharwat A 2018. Classification assessment methods. *Applied Computing and Informatics*.

Van Til M, Bijlmer A & De Lange R 2004. *Seasonal variability in spectral reflectance of coastal dune vegetation*. EARSeL eProceedings. [online]. Available from: https://www.researchgate.net/profile/Mark_Til/publication/241220900_SEASONAL_VARIABILITY_IN_SPECTRAL_REFLECTANCE_OF_COASTAL_DUNE_VEGETATION/links/5631e0a208ae0530378d379e.pdf [Accessed 22 August 2019].

Tippmann S 2015. Programming tools: Adventures with R. *Nature* 517, 7532: 109–110. [online]. Available from: www.r-bloggers.com [Accessed 27 June 2021].

Tong H, Maxwell T, Zhang Y & Dey V 2012. A Supervised and Fuzzy-based Approach to Determine Optimal Multi-resolution Image Segmentation Parameters. *Photogrammetric Engineering & Remote Sensing* 78, 10: 1029–1044. [online]. Available from: http://openurl.ingenta.com/content/xref?genre=article&issn=0099-1112&volume=78&issue=10&spage=1029 [Accessed 14 May 2019].

Turner W, Spector S, Gardiner N, Fladeland M, Sterling E & Steininger M 2003. Remote sensing for biodiversity science and conservation. *Trends in Ecology & Evolution* 18, 6: 306–314. [online]. Available from: https://www.sciencedirect.com/science/article/pii/S0169534703000703 [Accessed 2 May 2019].

Vani V & Mandla VR 2017. Comparative study of NDVI and SAVI vegetation indices in Anantapur district semi-arid areas. *International Journal of Civil Engineering and Technology* 8: 559–566.

Varga OG, Nagy IG, Burai P, Tomor T, Lénárt C & Szabó S 2018. Land cover analysis based on Sentinel-2 time series data. *Landscape & Environment* 20, 1. [online]. Available from: http://landscape.geo.klte.hu/pdf/agd/2018/2018v12is2_1.pdf [Accessed 25 March 2019].

Vink N & Tregurtha N 2003. *Western Cape Agricultural Sector*. [online]. Available from: https://www.westerncape.gov.za/other/2005/10/final_first_paper_overview_agriculture.pdf [Accessed 31 March 2019].

VinPro 2021. *Planting of Grapes in South Africa*.

Wang Q, Shi W, Li Z & Atkinson PM 2016. Fusion of Sentinel-2 images. *Remote Sensing of Environment* 187: 241–252. [online]. Available from: https://www.sciencedirect.com/science/article/abs/pii/S0034425716304023 [Accessed 26 March 2019].

Waske B & Braun M 2009. Classifier ensembles for land cover mapping using multitemporal

SAR imagery. *ISPRS Journal of Photogrammetry and Remote Sensing* 64, 5: 450–457.

Water D of 2010. *Strawberry production guideline*.

WCDoA 2018. *The Western Cape mapping of agricultural commodities and infrastructure 2013 and 2017.Elsenburg: GIS Services Western Cape Department of Agriculture.*

Wicaksono P & Aryaguna PA 2020. Analyses of inter-class spectral separability and classification accuracy of benthic habitat mapping using multispectral image. *Remote Sensing Applications: Society and Environment* 19: 100335.

Wójtowicz M, Wójtowicz A & Piekarczyk J 2016. *Application of remote sensing methods in agriculture.Communications in Biometry and Crop Science* 11 [online]. Available from: http://agrobiol.sggw.pl/~cbcs/articles/CBCS_11_1_3.pdf [Accessed 9 February 2019].

Xue J & Su B 2017. Significant Remote Sensing Vegetation Indices: A Review of Developments and Applications. *Journal of Sensors* 2017: 1–17. [online]. Available from: https://www.hindawi.com/journals/js/2017/1353691/ [Accessed 24 May 2019].

Yang D, Chen J, Zhou Y, Chen Xiang, Chen Xuehong & Cao X 2017. Mapping plastic greenhouse with medium spatial resolution satellite data: Development of a new spectral index. *ISPRS Journal of Photogrammetry and Remote Sensing* 128: 47–60. [online]. Available from: https://www.sciencedirect.com/science/article/pii/S0924271616302982 [Accessed 15 February 2019].

Yildiz O. T & Alpaydin E 2012. *Univariate and Multivariate Decision Trees*. TAINN. [online]. Available from: https://www.researchgate.net/publication/267799938_Univariate_and_Multivariate_Decision_Trees [Accessed 27 May 2019].

Zheng H, Du P, Chen J, Xia J, Li E, Xu Z, Li X & Yokoya N 2017. Performance evaluation of downscaling sentinel-2 imagery for Land Use and Land Cover classification by spectral-spatial features. *Remote Sensing* 9, 12.

Zhou Q 1996. *Ground Truthing*. Proceedings of Geoinformatics'96 Conference,. West Palm Beach: 69–77. [online]. Available from: http://citeseerx.ist.psu.edu/viewdoc/download?doi=10.1.1.613.245&rep=rep1&type=pdf [Accessed 30 May 2019].

Zvoleff A 2020. GLCM.

# APPENDIX A

Link to tables containing the JM distance between each net class and the other land cover classes for each acquisition period

https://drive.google.com/drive/folders/1RXFb2eZV_MX78Wx1dSJMYoVBJuLmhCAz?usp=sharing

# APPENDIX B

Link to tables containing the confusion matrices for each classification scenario

https://drive.google.com/drive/folders/14ut4U5bg4bUU0dqLOXkhCYXvoBpuHVaf?usp=sharing

# APPENDIX C

Link to tables containing the correlation matrix for the classification features

https://drive.google.com/drive/folders/1Rd9lkjfjOLKcrF8d3Cf3K09pq41hyvQw?usp=sharing